Titanium-Doped Sapphire Laser Research and Design Study

Peter F. Moulton

N/\S/\

NASA Contractor Report 4093

Titanium-Doped Sapphire Laser Research and Design Study

Peter F. Moulton

Schwartz Electro-Optics, Inc.
Boston Division
Concord, Massachusetts

NASA

National Aeronautics
and Space Administration

Scientific and Technical
Information Office

1987

Table of Contents

Table of Tables

Table of Figures

1 Introduction

The discovery and development of broadly tunable lasers has been of great benefit to the field of remote sensing. One can detect spatially resolved molecular concentrations by combining aerosol scattering and differential-absorption techniques with laser radar (LIDAR), if the laser transmitter can be tuned through the appropriate molecular absorption bands. To date, the most commonly used tunable lasers have used, as the active medium, organic dyes in a liquid solvent. It is generally conceded that dyes are not practical for spacecraft applications, where a laser system must run without attention for a substantial period of time and the environment is not friendly to flowing-liquid systems. With the relatively recent development of tunable lasers based on solid state crystals, an opportunity exists for construction of energetic tunable systems which can meet the rigorous requirements of a space-based application. The $Ti:Al_2O_3$ (or Ti:sapphire) laser is a particularly attractive candidate for remote sensing since the demonstrated tuning range includes wavelength regions around 726 and 939 nm, for H_2O sensing and 760 nm for O_2 detection. If the optical pump for the $Ti:Al_2O_3$ laser is a frequency-doubled neodymium (Nd)-doped solid state laser, which is in turn pumped by an array of semiconductor diode lasers, one can consider construction of an all-solid-state, space-qualified LIDAR transmitter with an operational lifetime measured in years.

The $Ti:Al_2O_3$ system is a relatively new laser, having been first demonstrated in 1982 at MIT Lincoln Laboratory, and as such is still in the development stage. For the study reported here there were several tasks defined for investigation. The first was an evaluation of the fundamental laser parameters of $Ti:Al_2O_3$, important to the design of any $Ti:Al_2O_3$ system. The second was characterization of commercially grown $Ti:Al_2O_3$ crystals, necessary given the limited experience in the crystal-growth industry with production of laser-quality material. The last topic involved the design of a narrow-linewidth $Ti:Al_2O_3$ oscillator suitable for NASA remote-sensing applications. The report is divided into three major sections covering each of the tasks described above.

2 Fundamental Laser Parameters Of $Ti:Al_2O_3$

Included as an Appendix in this report is a copy of an article by the Principal Investigator for the study. The experimental work in the paper was done while the author was at Lincoln Laboratory, but some of the theoretical analysis on derivation of the gain cross section, including the calculation of gain in anisotropic media, was performed as part of this study. There are two items, discussed in the study Statement of Work, which are covered in the article: a calculation of gain cross section based on laser data and a measurement of the effect on crystal temperature on fluorescence lifetime. In the following we summarize the results described in more detail in the Appendix and provide additional information gathered during the study. The last subsection covers study measurements made on the surface optical damage threshold of $Ti:Al_2O_3$.

2.1 Gain cross section

In the Appendix the value of the gain cross section is estimated by four different techniques, from a direct gain-probe measurement, from the laser threshold of a well-character-ized quasi-cw laser, from the measured fluorescence lifetime and emission spectra and from the value of the absorption cross section. The estimated values agreed reasonably well, and our best estimate for the gain cross section is 3.5 x 10^{-19} cm^2. The data from this study on $Ti:Al_2O_3$ oscillators, discussed in more detail in Sections 4.2 and 4.3 below, is in reasonable agreement with that value.

2.2 Fluorescence lifetime vs temperature

As shown in Fig. 3 in the Appendix, the reduction in fluorescence lifetime with increasing temperature is negligible up to 200 K, and is fairly rapid above 300 K. The behavior is characteristic of the onset of significant nonradiative decay of the excited state due to

multiphonon emission. Byvik and Buoncristiani[1] at NASA/Langely and Albers et al[2] have also measured the lifetime vs temperature relationship, with essentially similar results. The experimental data can be fit well to a standard activation-energy relation, such that the decay rate R (inverse of lifetime) is given by the formula,

$$R = R_0 + S exp(-E_A/kT)$$

where R_0 is the low-temperature rate, S is the 'hopping' rate, E_A is the activation energy, k is Boltzman's constant and T is the temperature. We found a good fit for an S and E_A of 2.5 x 10^9 sec^{-1} and 2350 cm^{-1}, respectively. The basis for the activation-energy relation is the existence of a nonradiative state at a level E_A above the upper level of the fluorescence transition. The physical process of nonradiative decay for the Ti^{3+} ion is not as simple as thermally excited transitions to a single higher-lying level, however, and the value for E_A may have little physical significance. In addition, hopping rates are typically assumed to be on the order of lattice vibrational rates, 10^{12} to 10^{13} Hz, and the value we found for S is somewhat surprising. More sophisticated treatments[3] of the temperature quenching of fluorescence have been developed. Albers et al have applied the Struck and Fonger model to the Ti:Al$_2$O$_3$ lifetime data and find a good fit, but only by using an unphysical value for the adjustable parameter equivalent to the hopping rate in the activation-energy model. The Struck and Fonger model assumes that a simple single configuration coordinate treatment can describe the energy levels of the fluorescing ion. Since both the upper (^2E) and lower ($^2T_2$) levels of the Ti^{3+} ion are subject to Jahn-Teller distortions one cannot assume that the simple configuration-coordinate model is appropriate for the system. A theoretically correct treatment of the temperature quenching process is thus difficult and well beyond the scope of this study.

We can estimate the level of heating in a optically pumped crystal to determine if the lifetime reduction could be a problem. The greatest temperature rise occurs under pulsed conditions in the time period immediately after the pump pulse ends. If the pulse is short compared to the time required for heat to diffuse away from the pumped region, then for a longitudinally pumped crystal, the temperature rise T_r right at the crystal entrance surface is given by the relation

$$T_r = F_p \alpha /C ,$$

where F_p is the dissipated pump fluence (Joules/cm^2) inside the crystal surface, α is the pump absorption coefficient in cm^{-1} and C is the heat capacity of the crystal, which for Al$_2$O$_3$ is 1.8 degrees C/cm^3. Assuming the extreme conditions of F_p equal to 10 J/cm^2 and an α of 2 cm^{-1}, we calculate a temperature rise of only 11 degrees, which would have an insignificant effect on the lifetime for a laser crystal at 25 degrees C nominal temperature.

2.3 Surface optical damage data

The surface optical damage threshold for the pump radiation is one of the key parameters in the design of Ti:Al$_2$O$_3$ systems pumped by conventional q-switched and frequency-doubled Nd lasers. We initially attempted measurements of surface damage threshold by using an unstable resonator Nd:YAG oscillator, described in Section 4. The second harmonic of the oscillator was spatially filtered at the focus of a long-focal-length lens to remove the diffraction rings surrounding the far-field central beam, and refocused at a test region. The beam profile at the test region was characterized by measuring the fractional amount of energy passed through a number of calibrated apertures with differing diameters, and was found to sharply peaked at the center, much more so than the Gaussian distribution found for stable, TEM$_{00}$ oscillators. We were not satisfied with the reliability of the damage thresholds measured, especially since the threshold fluence (Joules/cm^2) appeared to change drastically as we changed the focal length of the lens used to focus energy on the sample.

The measurements we report here were accomplished by employing a frequency-doubled, TEM$_{00}$, Nd:YAG oscillator-amplifier system, also described in Section 4. The use of a TEM$_{00}$-mode laser assured that the intensity in the beam varied smoothly from the center to the

2

edge, without the high spatial frequencies or 'hot spots' present in the output of either unstable or multi-transverse-mode stable-resonator oscillators. The beam radius at the focus of the test beam was estimated, as discussed above, by measuring the fractional transmission through apertures. Figure 1 shows data points for two focusing lenses, of 1- and 2-meter focal lengths. Also shown in the figure are two theoretical curves for focal spot radii of 0.15 and 0.55 mm, based on the relation for a Gaussian beam

$$F = 1 - exp(-2a^2/w^2) ,$$

where F is the fractional transmission, a is the aperture radius and w is the focal spot radius. Enough data points were available for the spot created by the 2-m lens to convincingly show that the beam profile was close to Gaussian, with some indication of more energy in the periphery of the beam than expected for a purely Gaussian distribution.
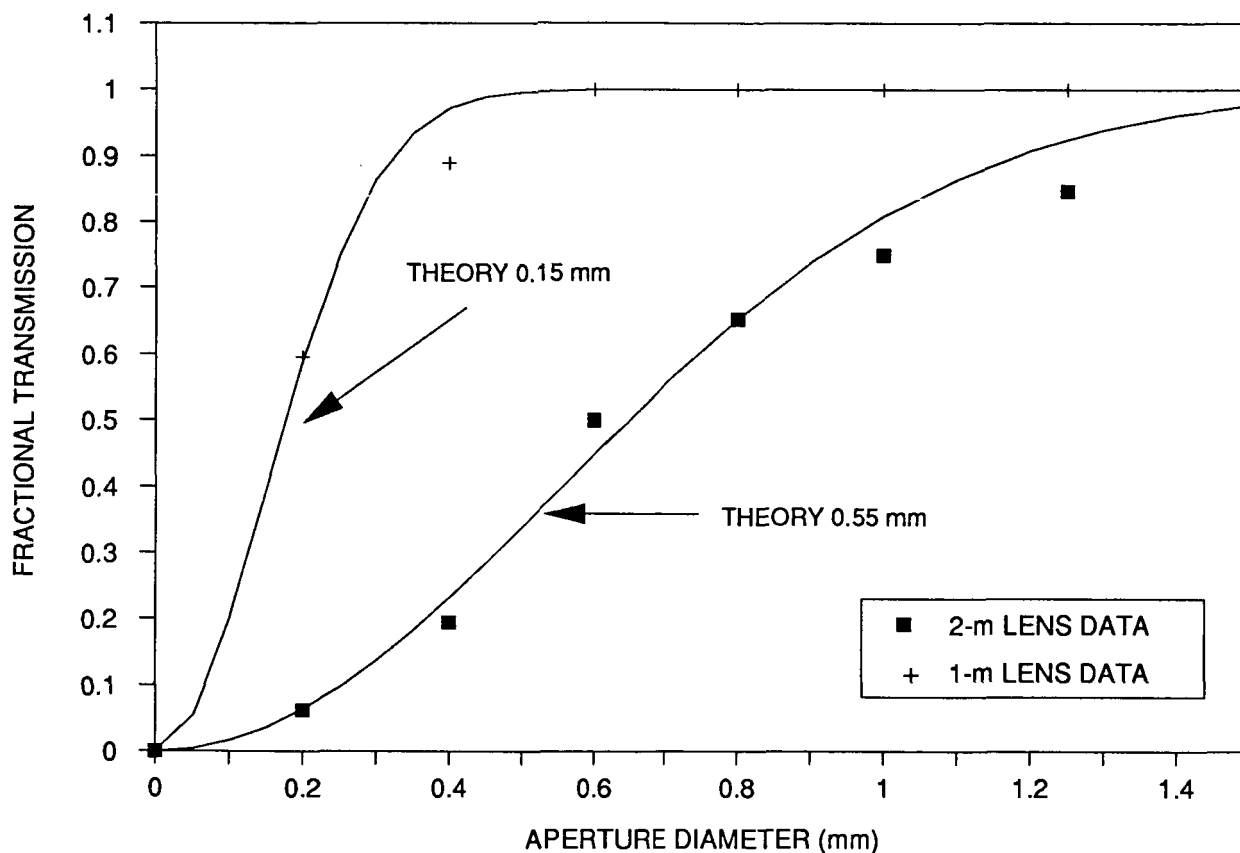
Figure 1. Fractional transmission of focused beam as a function of aperture size.

Three Ti:Al$_2$O$_3$ crystals with differing Ti^{3+} concentrations were tested for surface-damage threshold. Crystal #1, in the form of a cube with 2-cm-long edges, was cut from the first boule grown by Union Carbide under the NASA contract, and was very lightly doped. The polarized peak absorption coefficient at 500 nm was 0.27 cm^{-1}, corresponding (based on data developed in the Appendix) to a Ti^{3+} concentration of 0.014 wt.%. Crystal #2 was also from Union Carbide, and supplied to us by NASA. It had a higher doping level of 0.047%, and was in the form of a half cylinder, 2.2 cm long and 3.8 cm in diameter. Crystal #3 was from Crystal Systems, had a doping level of 0.053% and was a cylinder 1.7-cm in length and 1.7-cm in diameter. All samples were uncoated; the two Union Carbide samples had inspection-polished faces, while the Crystal

Systems sample had a laser-grade polish.

The determination of damage threshold was done as follows: The test laser was run at a constant 5-Hz repetition rate and one spot on the sample was illuminated. The incident energy was increased in steps, and at each step the laser output was maintained on the sample for at least 2 minutes, or for greater than 600 pulses. We took as an indication of damage during the illumination period an increase in scattering of the incident beam. Several spots on each sample were examined to reduce the effect of a gross variation in sample finish over the surface.

For a Gaussian-profile beam we can define an average fluence F_{ave} by the relation

$$F_{ave} = E / \pi w^2 \, ,$$

where E is the beam energy. The peak fluence at the beam center is twice the average value. We were not able to damage any of the samples with a focal spot size of 0.55 mm up to the maximum energy available from the system, 100 mJ, which implies that the average damage fluence was greater than 10.5 J/cm². It was possible to create damage with the smaller spot size associated with the 1-meter lens, and damage threshold data appears in Table 1 for the three crystals. For Crystal #1 damage appeared on the exit face of the sample, while damage was on the entrance face for the other crystals. Typically, in the absence of any absorption in the bulk of a crystal, damage appears on the exit face because the electric fields from the transmitted and reflected beams add at the exit face. The absorption of the incident beam was sufficiently low for Crystal #1 to permit exit-face damage, but high enough in the other two crystals to result in entrance-face damage.

Table 1. Surface-damage threshold for three crystals.

Crystal #	Sample ID	Absolute Damage Energy (mJ)	Peak Energy Fluence (J/cm²)
1	UCNAS5	12-15	19-24
2	UCNAS2	5-6	8-10
3	CS10	7.5	12

It is apparent that the damage threshold is reduced at increased doping levels. (The difference in threshold between Crystals #2 and #3, which had about the same doping level, may be related to the poorer surface finish of Crystal #2.) The increased absorption of the incident energy in the bulk of the more heavily doped material could produce additional stresses on the surface which reduce the damage threshold, or there may be more fundamental changes in the crystal properties induced by the presence of Ti^{3+} ions. Further studies of damage, over a wider range of doping levels, are recommended.

3 Characterization Of Commercially Grown Material

Over the course of the study a number of samples of Ti:Al$_2$O$_3$ were made available to us for examination. Some material was furnished by NASA as a result of a contract with Union Carbide and some material was provided directly to us by Milan Kokta at Union Carbide. In addition we received several crystals from Chandra Khattak at Crystal Systems and one (not commercial) sample grown by Robert Fahey at MIT Lincoln Laboratory.

Our primary method of characterization was to measure the polarized absorption in the material over the wavelength range 400-2000 nm. The measurement device was a Perkin-Elmer Lambda 9 spectrophotometer, fitted with Polaroid sheet polarizers in both sample and reference beams. Both Polaroid HN-32 (1.8-mm thick), effective from 400-700 nm, and HR sheet, effective from 700-2000 nm, were used. In some cases the spectrophotometer data was transferred in real time to a computer for further analysis.

One major issue in any absorption measurement is the establishment of an accurate baseline or zero-absorption level, made difficult by the presence of Fresnel reflection losses from the sample surfaces. Reflection losses are particularly large for the high-index material sapphire, and for the Ti:Al$_2$O$_3$ crystals the additional weak absorption band in the infrared from as-yet-unidentified impurities or defects is another complication. As shown in the Appendix, absorption from this band extends out to 2000 nm. In most of our measurements we set the baseline level to the transmission observed at 2000 nm. We were fortunate to have available for measurement a set of samples prepared by Milan Kokta at Union Carbide which permitted us to effectively eliminate the problem of baseline ambiguity. The set consisted of pairs of crystals cut from the same section of a boule, with one crystal of the pair approximately 1-cm in length and the other 2-cm in length. By placing the short sample in the spectrophotometer reference beam and the long sample in the sample beam we could cancel out the effects of Fresnel losses. In Fig. 2 we show the absorption spectra in the range 400-800 nm resulting from the matched pairs of samples, clearly showing that absorption in the infrared increased for samples with greater visible-wavelength $^2T_2 \rightarrow {}^2E$ absorption. Figure 3 plots the infrared absorption band for one sample set.
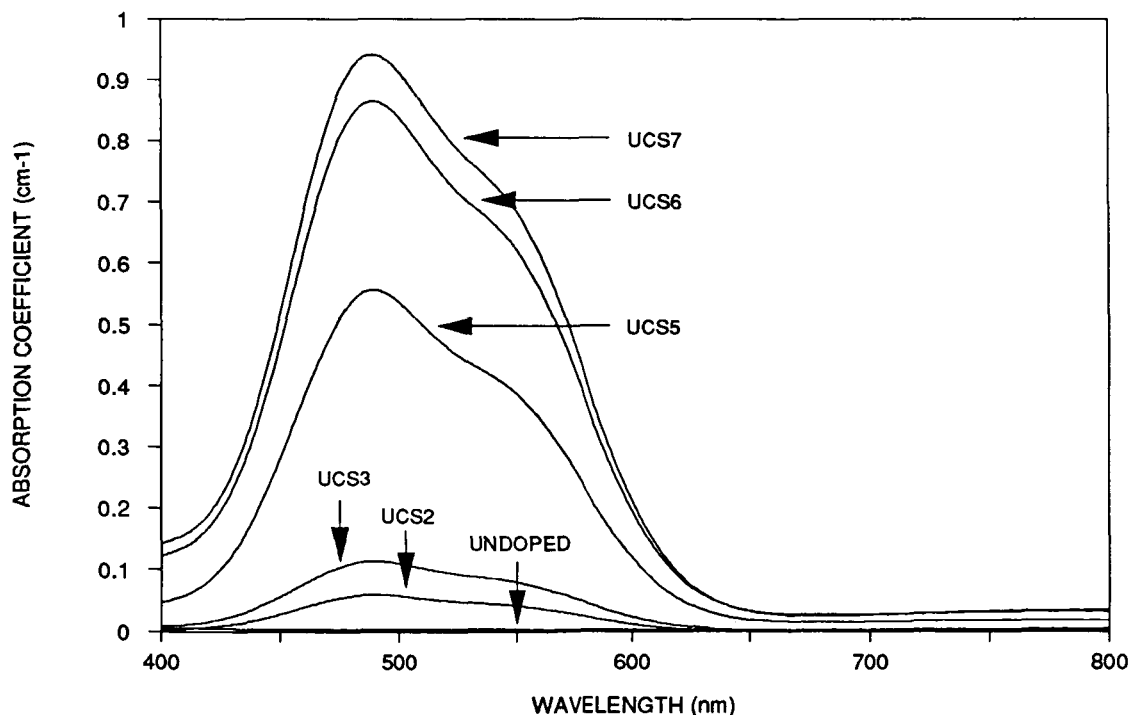
Figure 2. Absorption spectra for matched pairs of samples.
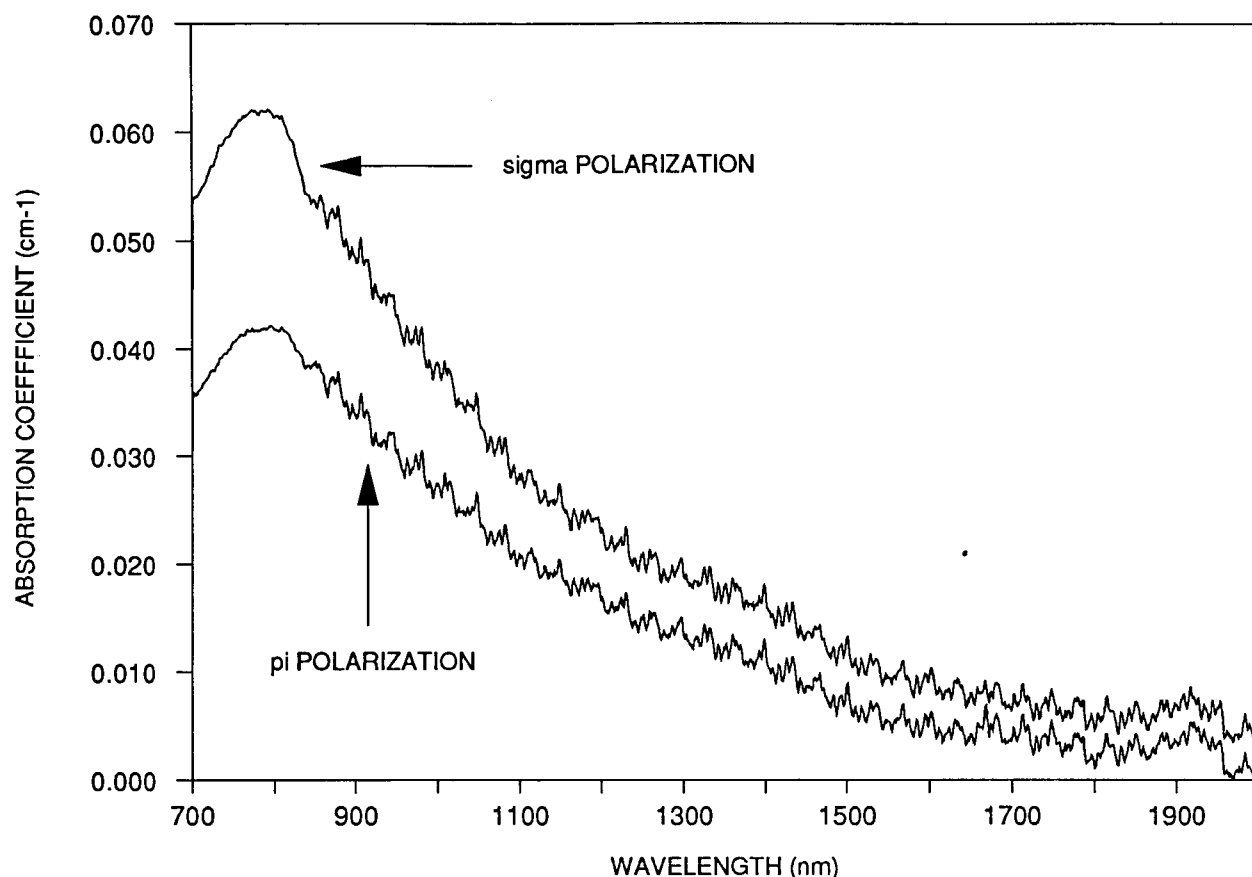
Figure 3. Infrared absorption band for one sample pair.

Table 2 lists absorption data for the samples examined in terms of two quantities, the π-polarized absorption coefficient at 490 nm, at the peak of the $^2T_2 \rightarrow {}^2E$ absorption band of the Ti^{3+} ion, and the π-polarized absorption coefficient at 800 nm, at the peak of the infrared absorption band. Also shown in Table 2 is the Ti^{3+} concentration in weight percent based on the measured absorption, the weight percent used in the initial melt (when known) and the ratio of 500- to 800-nm absorption, often referred to as the 'goodness coefficient' or 'figure of merit' (FOM) for the material. Data on samples UCS2, UCS3, UCS5, UCS6 and UCS7 resulted from the use of matched sets of samples, and the path length indicated is the difference between the lengths of the sample-beam and reference-beam crystals. Sample UCS5A is the same as UCS5, except that the crystal had been annealed at Union Carbide and the data was taken without a short sample in the reference beam.

6

Table 2. Absorption data for 18 samples.

SAMPLE ID	SOURCE	DESCRIPTION	PATH LENGTH (cm)	490-nm ABS. COEFF. (cm-1)	800-nm ABS. COEFF. (cm-1)	FOM	CONC. (wt. %)	START MELT (%)
UCNAS2	UC/NASA	1/2 CYLINDER 3.72 cm dia.	2.21	0.990	0.045	21.8	0.047	0.38
UCNAS3	UC/NASA	RECTANGLE 0.79x0.94 cm	2.32	0.140	0.022	6.5	0.007	0.25
UCNAS4	UC/NASA	RECTANGLE 0.82x0.94 cm	2.32	0.333	0.017	19.7	0.016	NA
UCNAS5	UC/NASA	CUBE 2 cm edges	2.01	0.300	0.028	10.8	0.014	NA
UCNAS6	UC/NASA	ROD 1D66 0.6 cm dia.	7.62	0.236	0.010	23.6	0.011	NA
UCNAS7	UC/NASA	ROD 2E08 0.5 cm dia.	7.62	1.010	0.028	36.5	0.048	NA
UC10	UC	RECTANGLE 0.91x1.21 cm	1.78	1.180	0.045	26.4	0.056	NA
UCS2	UC	RECTANGLE 0.7x0.7 cm	1.00	0.138	0.020	6.9	0.007	0.25
UCS3	UC	RECTANGLE 0.7x0.7 cm	1.01	0.262	0.015	17.5	0.012	0.25
UCS4	UC	RECTANGLE 0.7x0.7 cm	2.03	0.917	0.043	21	0.043	0.50
UCS5	UC	RECTANGLE 0.7x0.7 cm	1.11	1.157	0.042	27.5	0.055	0.50
UCS5A	UC	RECTANGLE 0.7x0.7 cm	2.04	1.360	0.017	80.0	0.064	0.50
UCS6	UC	RECTANGLE 0.7x0.7 cm	1.03	1.927	0.074	26.0	0.091	1.00
UCS7	UC	RECTANGLE 0.7x0.7 cm	0.96	2.072	0.094	22.0	0.098	1.00
CS10	CS	ROD 1.74 cm dia.	1.74	1.120	<0.01	>100	0.053	NA
CS13	CS	ROD 1.06 cm dia.	1.40	1.440	0.017	84.7	0.068	NA
CS28.1	CS	ROD 1.10 cm dia.	6.72	0.626	0.0065	96.3	0.030	NA
S-007	LL	CYLINDER 2.34 cm dia.	1.90	2.030	0.040	50.8	0.096	NA

One of the unknowns at the beginning of the study was whether the FOM depended greatly on the density of Ti^{3+} in the sample. Figure 4 plots the FOM for all the samples as a function of the absorption coefficient at 490 nm, which is proportional to the Ti^{3+} concentration. All of the samples with a FOM below 40 were from Union Carbide, and there does not appear to be any clear trend in their variation of FOM with absorption coefficient. Samples provided by Crystal Systems and Lincoln Laboratory had significantly higher FOMs than all but one of the Union Carbide crystals, consistent with earlier findings discussed in the Appendix. One of the samples from Crystal Systems is shown with an FOM of 100, but the actual value was likely higher than that, as the amount of absorption at 800 nm was below the measurement limit of our spectrophotometer.
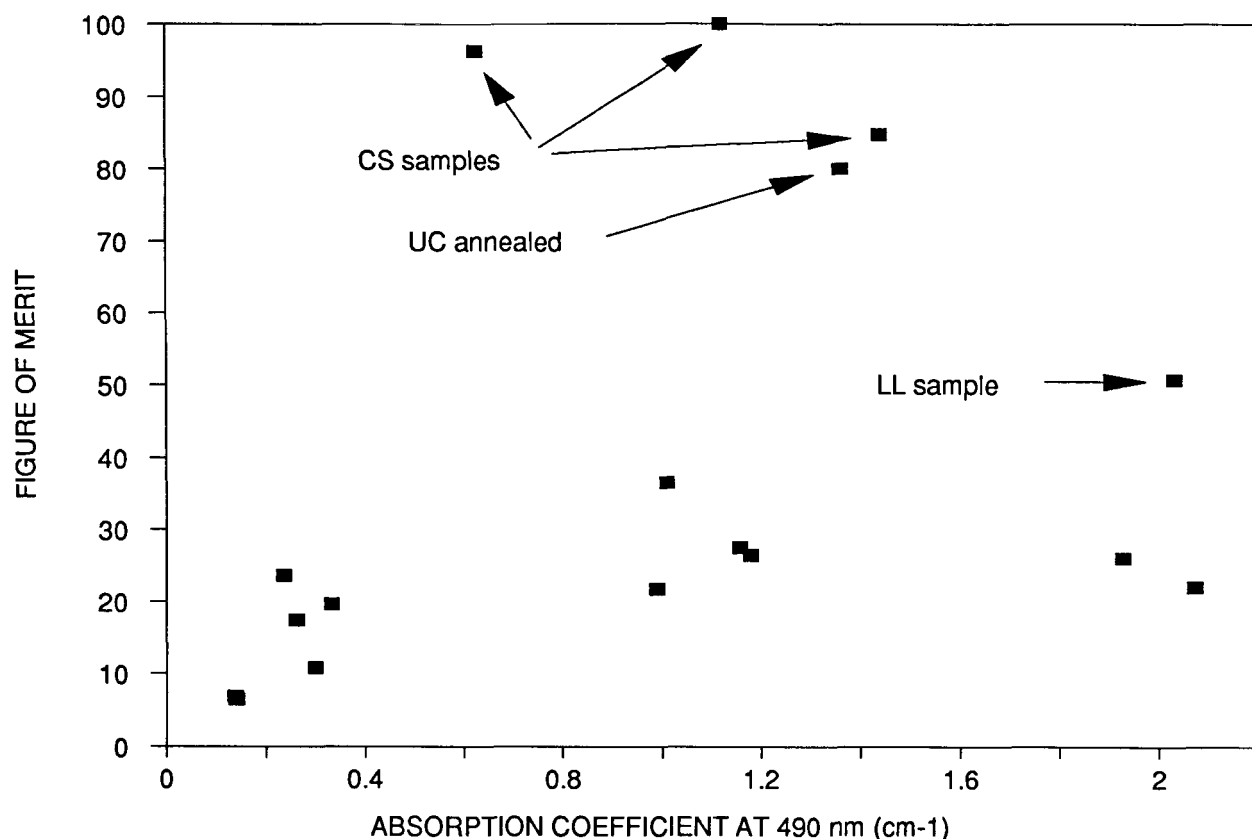
Figure 4. Plot of FOM vs 490-nm, π-polarized absorption coefficient.

There were several sets of crystals from Union Carbide provided to test the effects of post-growth annealing. The exact details of the annealing process were not furnished to us by Union Carbide, but in general annealing attempts to increase the ratio of Ti^{3+}/Ti^{4+} and possibly reduce the level of crystal defects by heating the sample up to high temperatures in a chemically inert or slightly reducing environment. Table 3 lists data comparing pairs of annealed and as-grown samples, with each pair originating from the same growth run. Union Carbide employed two types of annealing processes, an initial technique used on all but one of the crystals, and a newer process (starred in the column indicating annealed status) on one sample, UCS5, which had earlier been annealed by the initial technique. Thus, data for UCS5 appears twice. The early technique had, in most cases, the greatest effect on the apparent Ti^{3+} concentration, but did little to reduce the 800-nm absorption. The newer technique not only increased the apparent Ti^{3+} concentration but significantly reduced the 800-nm absorption, and produced a sample with the highest FOM for all of the Union Carbide material.

8

Table 3. Annealing data.

Sample ID	Anneal	490-nm Abs. Coeff. (cm^{-1})	800-nm Abs. Coeff. (cm^{-1})	FOM
UCNAS3	N	0.140	0.022	6.5
UCNAS4	Y	0.333	0.017	19.7
UCS2	N	0.138	0.020	6.9
UCS3	Y	0.262	0.015	17.5
UCS4	N	0.917	0.043	21
UCS5	Y	1.157	0.042	27.5
UCS5A	Y*	1.360	0.017	80
UCS6	N	1.927	0.074	26
UCS7	Y	2.072	0.094	22

*New annealing process

9

A number of samples from the three sources of Ti:Al$_2$O$_3$, Union Carbide, Crystal Systems and Lincoln Laboratory, were examined for optical scattering by propagation of an unfocused, 1 mW HeNe laser beam through the material and observation by eye of the scattering in a darkened room. All the samples exhibited scattering, which varied from being light and uniform throughout the crystal (Samples UCNASA5,6,7 and CS28.1) to light but non-uniform (Samples UC10, UCNASA2 and CS13) to moderate with evidence of occasional large centers (Samples CS10 and S-007). There did not appear to be a strong correlation between low scattering and high FOM and, in fact, the sample with the highest FOM (CS10) exhibited nearly the worst scattering. It is presumed that the scattering is associated with complexes of Ti^{4+} ions in the crystal, but we had no way of confirming this.

There is a strong ultraviolet absorption band present in Ti:Al$_2$O$_3$ crystals, whose peak intensity cannot be readily measured unless one uses thin (<1 mm) samples. As discussed in the Appendix, this band has previously been associated with a Ti^{3+} charge-transfer transition, but is now thought to result from Ti^{4+} ions. We measured the uv absorption in several of the 1-cm-long samples provided by Union Carbide, and the results for 5 samples are shown in Fig. 5. The data was taken with an unpolarized measurement beam and with no sample in the reference beam. However, all of the samples were oriented with the c-axis horizontal in the sample compartment, as we determined that the spectrophotometer beam tended to be strongly polarized in the horizontal plane. One of the samples, UCS1, was undoped, and the expected transparency of Al$_2$O$_3$ in the measurement range can be seen. No attempt was made to correct for Fresnel losses at the sample surface and thus the plot for the undoped sample provides a baseline reference. On comparison of the data for Samples UCS2 and UCS3 we note that the effect of annealing on the uv absorption is the opposite of that on the visible (Ti^{3+}-related) absorption. This result is consistent with the association of Ti^{4+} ions and the uv band and the assumption that annealing increases the Ti^{3+} concentration at the expense of the Ti^{4+}-ion concentration.
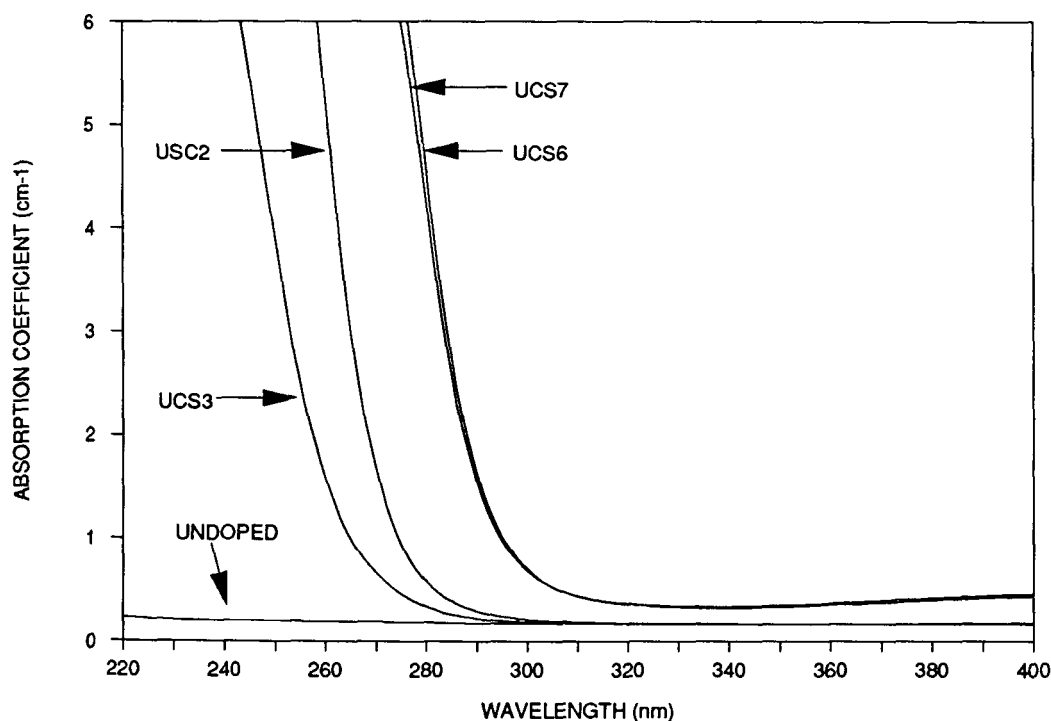
Figure 5. Uv absorption in 5 samples.

4 Design Of Tunable Narrow-Linewidth Oscillators

In this Section we describe both experimental and theoretical efforts towards the design of a narrow-linewidth Ti:Al$_2$O$_3$ oscillator. The experimental work involved development of a suitable pump laser, investigations of conventional two-mirror-cavity Ti:Al$_2$O$_3$ lasers and the construction and characterization of a Ti:Al$_2$O$_3$ ring-cavity oscillator. At the conclusion of the Section we present a theoretical design for a narrow-linewidth oscillator based, on part, on results of the experimental work.

4.1 Pump laser development

4.1.1 Unstable-resonator oscillator

The most widely used commercial q-switched and frequency-doubled Nd:YAG lasers (e.g. Quanta Ray and Quantel) employ an unstable-resonator configuration for the oscillator. The major advantage of the unstable resonator is that a large fraction of the stored energy in a typical Nd:YAG laser rod can be extracted in a single, low-divergence transverse mode, an important feature for obtaining efficient second-harmonic generation. We constructed an unstable resonator oscillator, the layout of which is shown schematically in Fig. 6, for evaluation as a pump source for Ti:Al$_2$O$_3$ lasers. The 6.3-mm dia. x 100-mm long laser rod was pumped by a xenon flashlamp (5-mm-dia. bore x 89-mm-long discharge) in a commercial (Kigre FC-35K) diffuse-reflector pump cavity. The lamp was driven by SEO-built electronics, which provided simmer operation for the lamp, used a SCR for discharge control and resonantly charged the capacitor bank. The unstable resonator design was similar to that described by Andreou[4] in the use of an output coupler with a highly reflecting dielectric-coated dot in the center of an anti-reflection-coated convex substrate. The dot diameter for our system was 2.0 mm and the nominal magnification of the positive-branch confocal resonator was 3.33.

Figure 6. Schematic of Nd:YAG unstable-resonator laser.

Figure 7 shows the long-pulse and q-switched output energies vs lamp input energy for the oscillator. Nearly 400 mJ of energy could be extracted at an input energy of 27 J, with an output pulse of approximately 15 nsec in duration. The ability of the oscillator to efficiently generate second-harmonic output is indicated in Fig. 8, where data is shown for two dif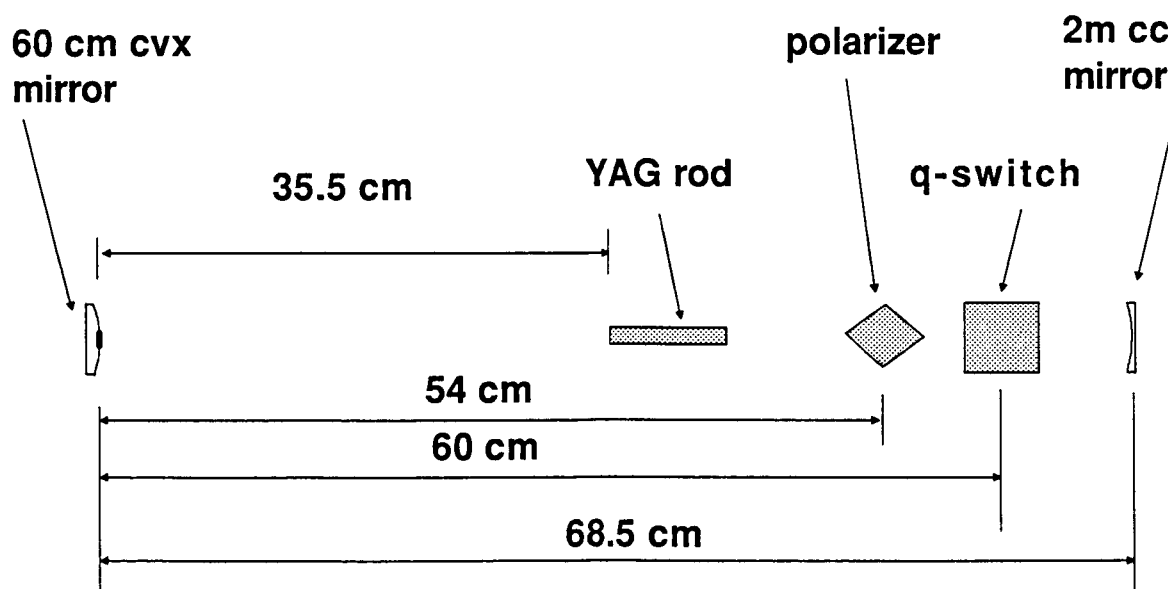ferent doubling crystals. The CD*A crystal, 2.5 cm in length, was cut for 84-degree phase-matching and placed in an oven for operation at a temperature of 90 centigrade, while the 2.5-cm-long KD*P crystal was angle-matched at room temperature. Both crystals were placed in the near-field output beam of the laser (no focusing lens was used) and, from the data in Fig. 8, we were able to obtain maximum conversion efficiencies of 43 and 33% for CD*A and KD*P, respectively. In terms of efficiency the CD*A crystal was superior, but we experienced damage problems with the inside surfaces of the cell windows used for the oven, possibly due to contamination from the contents of the cell, and thus tended to use the KD*P crystal in many of the experiments.

The efficient generation of second-harmonic output afforded by the use of the unstable-resonator oscillator was accompanied by some practical problems in employing such a system as a pump laser. We intended to use a longitudinal pumping configuration for the Ti:Al$_2$O$_3$ laser, which required that the pump output be focused, i.e be brought into the far field. The far-field energy distribution of the unstable-resonator laser consisted of a central spot with an intensity variation falling off more rapidly than a Gaussian distribution, surrounded by diffraction rings resulting from the presence of a hole in the center of the near-field output beam. The energy in the rings was between 30 and 40% of the total output energy. If one attempted to focus the pump beam into the crystal such that all the energy coupled into the desired mode of the Ti:Al$_2$O$_3$ laser, damage from the peak intensity in the central spot would limit operation of the Ti:Al$_2$O$_3$ system to low pump-energy levels. On the other hand, pump energy is effectively lost if the diffraction rings do not couple to the Ti:Al$_2$O$_3$-laser mode and thus the overall system efficiency is lowered. Also, we found that the transition region of the unstable-resonator beam, approximately 10 meters in length, in which the beam transforms from near to far field, exhibited a peak in the intensity profile (the spot of Arago) which would readily damage optical components unless care was taken in component placement. Although this problem can be dealt with in a given system, it can result in additional and unwanted constraints in the optical-system layout. Finally, we had some indication that the focused beam of the unstable-resonator laser, even after spatial filtering, tended to damage the surface of Ti:Al$_2$O$_3$ crystals at lower average-fluence levels than that of a TEM$_{00}$-mode laser. This may be the result of the more rapid variation in intensity with distance for the unstable-resonator mode, leading to a higher surface stress, or may be the result of errors in our estimate of beam intensity. It would be appropriate to examine this problem in more detail, but we felt it was beyond the scope of our study.

For the reasons just presented we concluded that development of stable-resonator lasers as pump sources was warranted, and this effort is described below.

4.1.2 TEM$_{00}$ and multimode oscillator-amplifier systems

The development of a TEM$_{00}$-mode pump source was initially motivated by the need to perform reliable and well-characterized surface-damage measurements on Ti:Al$_2$O$_3$ samples. The design of energetic TEM$_{00}$-mode oscillators requires that the optical cavity design maximizes the TEM$_{00}$-mode volume in the laser rod, while maintaining some practical level of cavity stability. We used a concave-convex-mirror design, with a 4-m and 6-m radii concave and convex mirrors, respectively, spaced 1.1-m apart, which led to the formation of a 2.2-mm spot diameter in the laser rod. Figure 9 shows the oscillator output energy as a function of lamp energy in both long-pulse and q-switched modes, and indicates that we could generate somewhat more than 50 mJ from the q-switched system. The components (except for cavity mirrors) in the TEM$_{00}$ oscillator were the same used in the unstable-resonator system, with the addition of a 2.5-mm-diameter intracavity aperture to limit operation to the TEM$_{00}$ mode. The output-energy limit was set by the inability of the q-switch to hold off higher stored-energy levels. Comparison of Figs. 7 and 9 point to the clear advantage of the unstable-resonator laser in efficiently generating single-transverse-mode output energies.

12
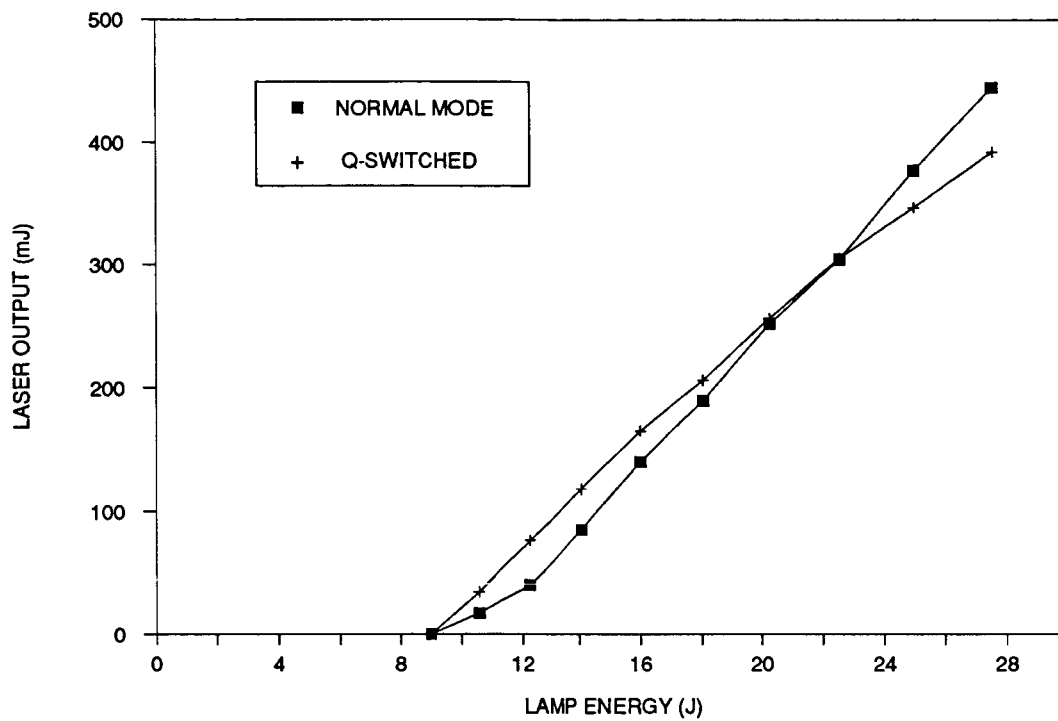
Figure 7. Output energy vs lamp energy for unstable-resonator laser.
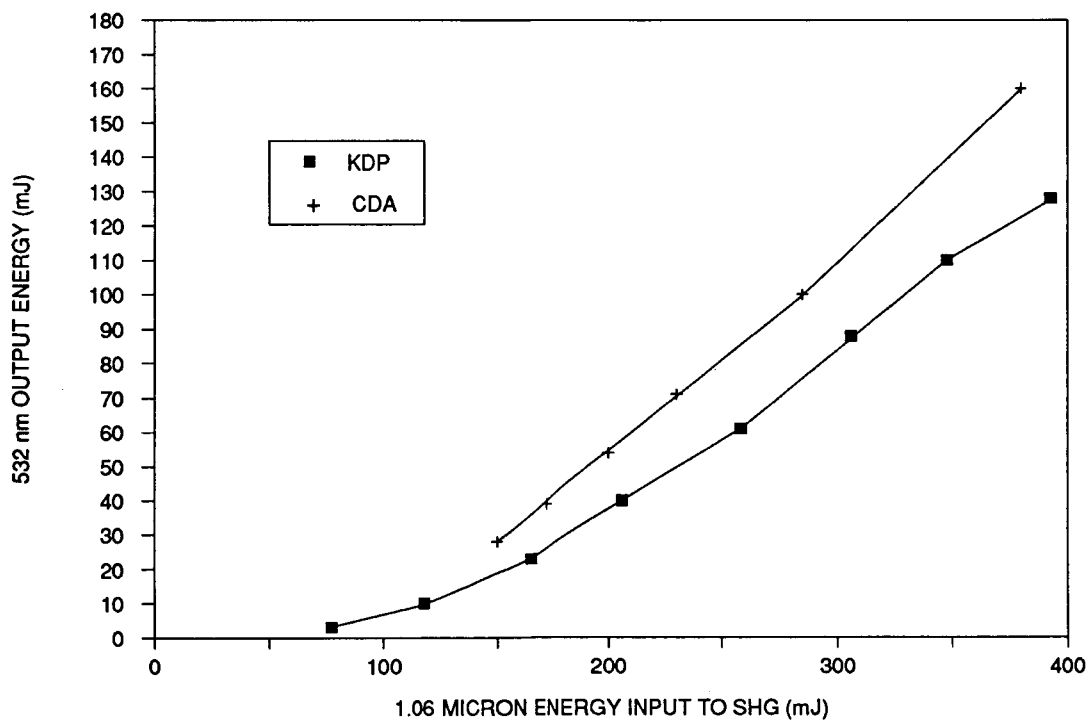
Figure 8. Second-harmonic output energy vs fundamental energy from unstable resonator laser, for two different doubling crystals.
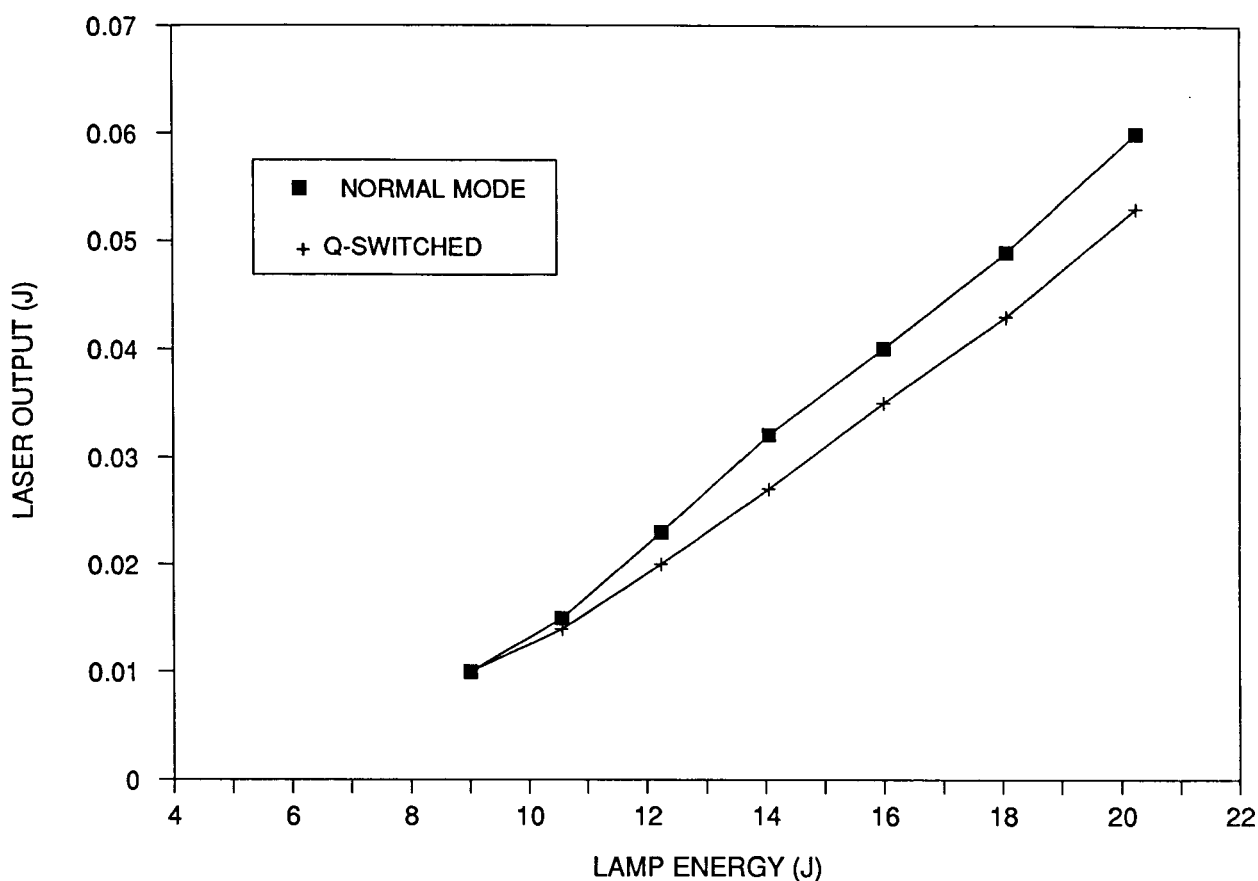
Figure 9. Output energy vs lamp energy for TEM_{00}-mode oscillator.

In order to obtain higher levels of output energy we amplified the output of the oscillator with a single-pass rod (6.3-mm dia. x 100-mm long) amplifier, pumped by a single lamp in an SEO-designed ceramic-reflector pump cavity. The output of the amplifier as a function of lamp input appears in Fig. 10, for two different input energies from the oscillator. The limit of output energy was set by parasitic-oscillation limits to stored energy in the amplifier rod. Second-harmonic generation from the amplifier output was accomplished by the KD*P crystal described in 4.4.1, and the energy input-output curve for an unfocused beam appear in Fig. 11. The harmonic-generation efficiencies for the unstable- and TEM_{00}-mode resonator systems were essentially the same for the same input energies.

The maximum amount of frequency-doubled energy, used in some experiments, was obtained by removing the aperture from the oscillator cavity, allowing the system to operate multi-transverse mode, approximately $3x$ diffraction limit. In that case we could generate 700 and 275 mJ of fundamental and second-harmonic energy, respectively, from the oscillator-amplifier combination at a 5-Hz rate.
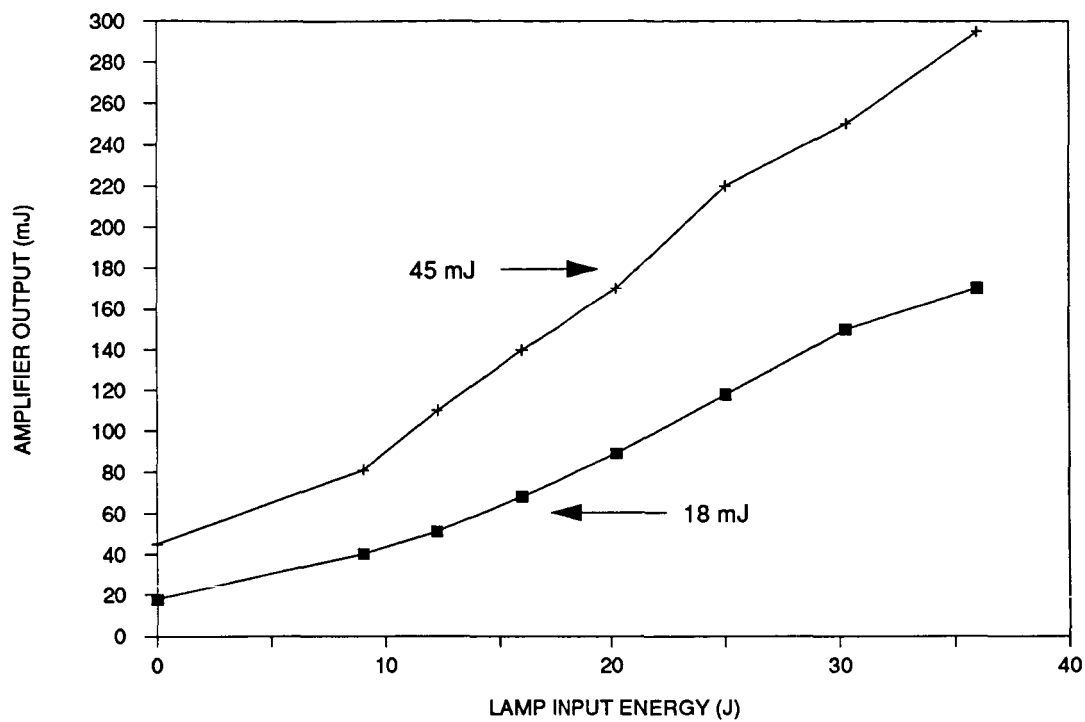
Figure 10. Output energy from amplifier vs lamp energy,
for two different input energies from TEM_{00}-mode oscillator.
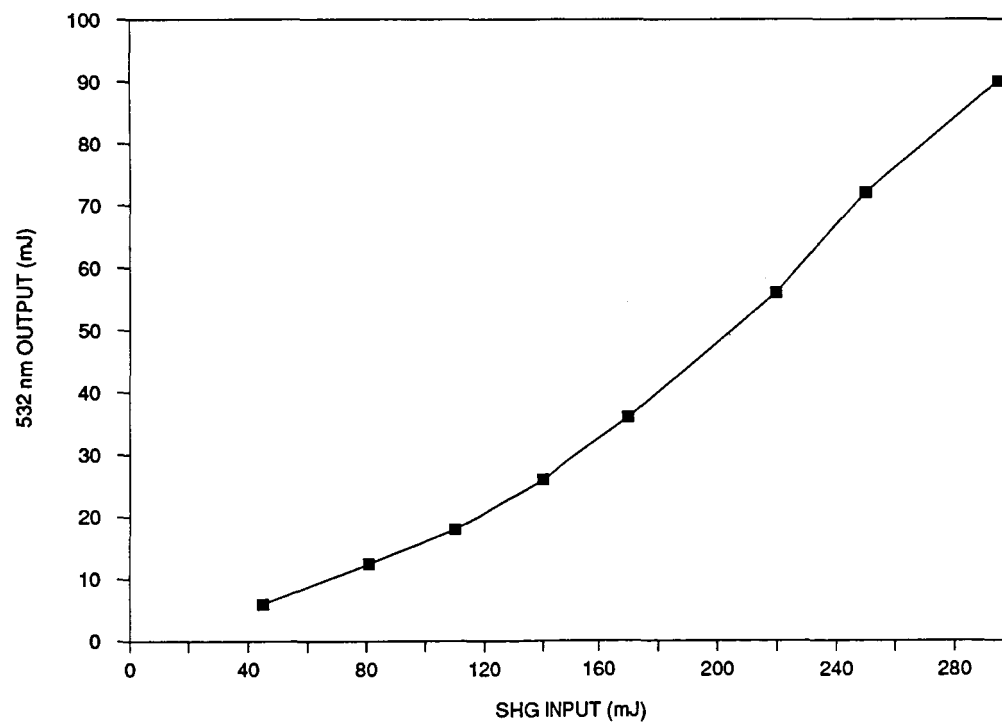
Figure 11. Second-harmonic output energy vs fundamental energy
from TEM_{00}-mode oscillator-amplifier system.

15

4.2 Conventional Ti:Al$_2$O$_3$ oscillators

In the performance of the study we constructed a number of longitudinally pumped Ti:Al$_2$O$_3$ oscillators. In early work we determined that one problem associated with longitudinal pumping was damage to the dichroic mirror through which the pump beam passed. We developed two techniques, shown schematically in Figs. 12 and 13, to avoid this problem. In the first, we used the dispersion inherent in Al$_2$O$_3$ in combination with a Brewster-angle laser crystal to separate the pump and laser beams outside of the laser medium. If one of the cavity mirrors was located sufficiently far from the crystal then the pump beam could pass to one side of the mirror. The angular separation between pump and laser beams is (for a 532-nm pump) 11 mrad at a 780-nm Ti:Al$_2$O$_3$ laser wavelength. The second technique is a variation on the first, by the addition of an intracavity prism (or prisms) to obtain additional angular separation between pump and laser beams, with the added benefit of adding the ability to tune the Ti:Al$_2$O$_3$ laser by rotation of one of the cavity mirrors. Our experiments with intracavity prisms showed that prisms made of high-index glass (SF-6) tended to undergo bulk damage from the pump beam, manifested by the creation of dark tracks in the material, while BK-7 glass or fused-silica prisms would operate free of damage.

Our initial oscillator experiments used crystal CS10, which was fabricated for normal-incidence operation with AR-coated surfaces, combined with a spatially filtered unstable-resonator pump. The oscillator could only operate at 2.4x the 7-mJ absorbed-energy threshold (for a 65-cm-long cavity consisting of a 5-m-radius high-reflector, an intracavity SF-6 glass prism and an 80%-reflectivity flat output coupler) before damage on the coated crystal surfaces appeared. The coating damage fluence was estimated to be 1.7 J/cm^2.

The remainder of the conventional-oscillator work employed a Brewster-angle crystal fabricated from material supplied by Crystal Systems. The crystal, 1.4-cm in length, absorbed 90% of the incident pump radiation, which implies that the average doping level was 0.1%. Energy input-output data for three different configurations is shown in Fig. 14. In all cases the pump laser was the oscillator-amplifier system described above, operated in the TEM$_{00}$ mode for the low- and medium-energy oscillator and multimode for the highest-energy oscillator. The resonator for the Ti:Al$_2$O$_3$ lasers consisted of a 2-m-radius, concave-surface high reflector, an intracavity fused-silica prism and a flat output mirror coated for 60% reflectivity at 780 nm. For the low and medium-energy lasers the cavity-mirror spacing was 1.2 m, decreased to 60 cm for the high-energy laser in order to accommodate the beam properties of the multimode pump laser. The operating wavelength was approximately 780 nm.

The low-energy laser operated in the TEM$_{00}$ mode, and was limited in output by optical damage to the pump-input face of the Brewster crystal. The pump-beam diameter at the crystal was measured to be 1.2 mm. In order to obtain the results shown for the medium-energy oscillator, we repositioned the pump focusing lens to produce a larger pump diameter at the crystal, approximately 2.2 mm. With the larger pump spot the Ti:Al$_2$O$_3$ laser no longer operated in a single transverse mode, as the gain region was large enough to support higher-order-mode oscillation. For the highest-energy system the multimode-pump diameter was approximately 3 mm, and the Ti:Al$_2$O$_3$ laser output was highly multimode. Thresholds for the low, medium and high-energy lasers were 8, 32 and 65 mJ, respectively. In the simplest approximation, we would expect that the thresholds would vary as the area of the pump beam, i.e be proportional to the pump fluence. The thresholds would be predicted to vary in the proportions 1: 3.4: 6.3, compared to the observed 1: 4: 8. The agreement between theory and data is not unreasonable, given that the transverse-mode properties of both the Ti:Al$_2$O$_3$ lasers and the pump beams changed from one oscillator to the next. A more detailed analysis of the threshold for longitudinally pumped lasers has been carried out[5], for the case of TEM$_{00}$-mode pump and laser beams. The analysis, applied to the lowest-energy oscillator (the only appropriate system), indicated that the threshold was consistent with a gain cross section of 2.3 x 10^{-19} cm^2, close to the value of 3-4 x 10^{-19} cm^2 determined by the work presented in Appendix A. The slope efficiencies of all the oscillators were high, 45, 58 and 52% for the low-, medium- and high-energy devices, corresponding to quantum efficiencies of 66, 85 and 76%.

16

HIGH REFLECTOR

RESIDUAL 532 nm

532 nm PUMP BEAM   LASER CRYSTAL

PARTIAL REFLECTOR
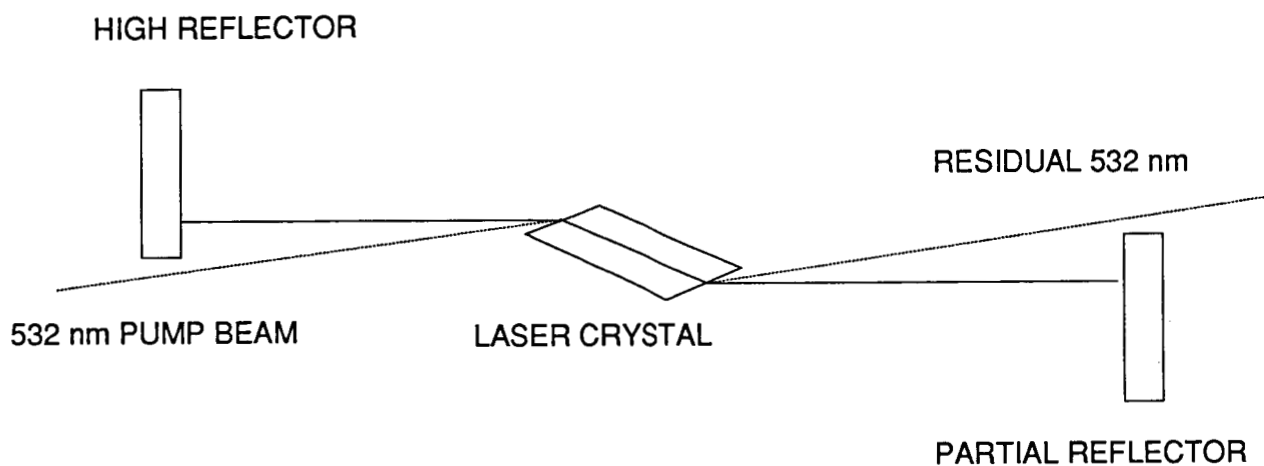
Figure 12. Scheme to avoid passing the pump beam through a cavity mirror
by dispersion coupling into a Brewster-angle crystal.

HIGH REFLECTOR

PRISM

532 nm PUMP BEAM

LASER CRYSTAL

PARTIAL REFLECTOR
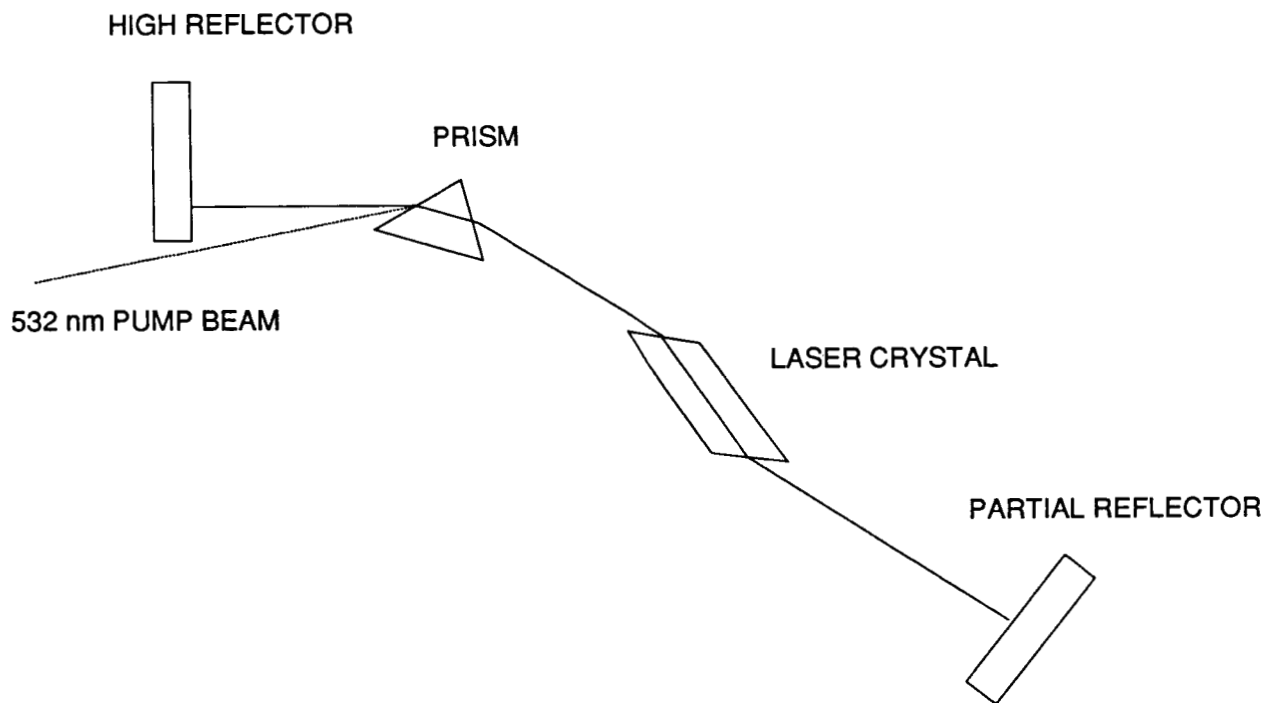
Figure 13. Scheme to avoid passing the pump beam through a cavity mirror
by use of an intracavity prism.
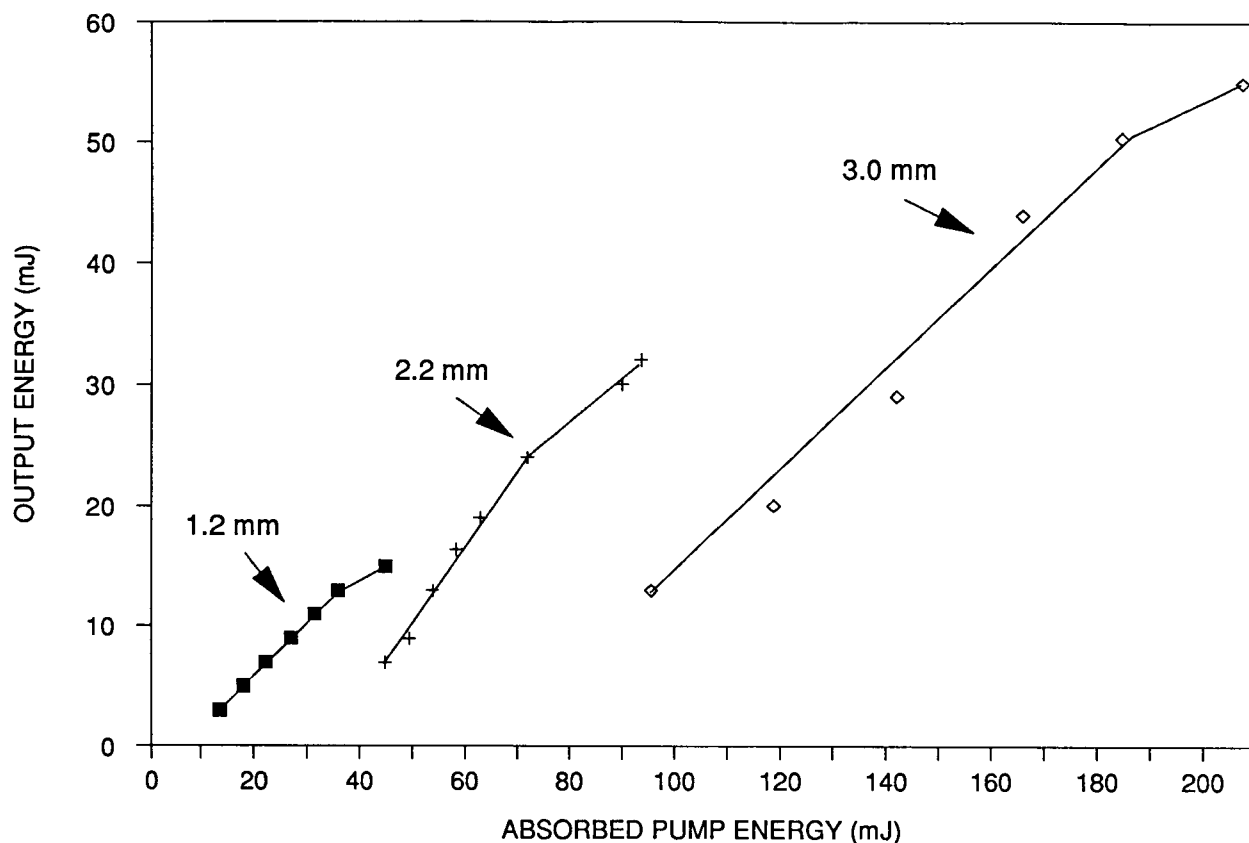
Figure 14. Input-output energy data for three different oscillator experiments.

The conventional oscillator experiments showed that scaling up the energy of Ti:Al$_2$O$_3$ lasers pumped longitudinally by q-switched, frequency-doubled Nd lasers is a straightforward matter. One increases the pump-beam diameter in the Ti:Al$_2$O$_3$ crystal in a manner which limits the fluence on the crystal surface to a level below the damage threshold. It is clear that the TEM$_{00}$ energy from such lasers is limited by the same issue limiting the TEM$_{00}$ energy produced by Nd-laser oscillators. That is, there is a practical upper limit to the TEM$_{00}$ beam size one can establish in the crystal, set by the properties of stable resonators. The output energy of the TEM$_{00}$-mode oscillator characterized in Fig. 14, limited to 15 mJ by damage, was generated in a resonator with a calculated beam diameter (at the crystal) of 1.1 mm. If we had employed the same convex-concave resonator used for the TEM$_{00}$-mode Nd:YAG laser described in Section 4.1.2, we should have, in theory, been able to generate around 60 mJ of TEM$_{00}$-mode output from the Ti:Al$_2$O$_3$ laser. Generation of higher-energy, diffraction-limited output would require use of an unstable resonator oscillator, or the addition of Ti:Al$_2$O$_3$ amplifier stages.

We determined during the course of the study that the use of injection techniques was the best approach to generation of narrow-linewidth output from Ti:Al$_2$O$_3$ lasers pumped by conventional q-switched lasers. With that in mind, we decided to construct and characterize a ring-cavity Ti:Al$_2$O$_3$ laser, described in 4.3, and forgo a detailed series of measurements on the temporal and spectral properties of the conventional oscillators.

18

4.3 Ring oscillator system

In the conceptual design of a narrow-linewidth Ti:Al$_2$O$_3$ oscillator, discussed in detail in 4.4, we identified the use of injection-locking as the most promising approach to obtaining narrow-linewidth (defined here as single-frequency) operation. A ring-cavity oscillator provides an ideal geometry for the use of injection-locking techniques. A beam injected in one direction into the cavity, through the output mirror, will not be reflected back on itself from any of the components in the ring cavity even when perfect mode-matching is attained. If the ring laser is unidirectional in oscillation, a property enhanced by the very use of injection, there will be no energy directly coupled back from the ring laser output to the injection source. We designed and operated a Ti:Al$_2$O$_3$ ring-cavity laser, and the results are described below.

Figure 15 presents a schematic diagram of the ring-cavity system. The same Brewster-angle crystal used for the conventional oscillators discussed in the previous Section was employed in the ring system, and a fused silica Brewster-angle intracavity prism provided both a means for pump-beam coupling and a dispersive element for tuning. In general the ring cavity oscillated in both directions, although under some (apparently random) alignment conditions nearly all of the energy could be observed in one direction. We were also able to get essentially unidirectional operation by placing a high-reflector mirror in one of the output beams, and aligning the mirror to feed back the beam to the opposite direction. In that case nearly all the output appeared in the opposite direction, but the output was very unstable. Energy input-output curves for the ring laser appear in Fig. 16, for 80%- and 60%-reflectivity output coupling mirrors, where the output energy was the sum of the energy in both directions. The pump system used just the Nd:YAG oscillator, operated multimode at a 5-Hz repetition rate, but the pump focusing was adjusted such that the Ti:Al$_2$O$_3$ laser operated in the TEM$_{00}$ mode. The thresholds observed were consistent with a gain cross section of 3 x 10^{-19} cm^2, and for the 60%-mirror system the observed slope efficiency of 62% implied a quantum efficiency of 92%. The lower slope efficiency found with the 80%-R output mirror was somewhat surprising given the efficiency level found with the 60%-R mirror. Cavity losses, exclusive of the output coupler, would have to be approximately 3.5% in order to allow a 92% slope quantum efficiency, and one would expect that the quantum efficiency obtained with the 80%-R mirror would be 85%, rather than the observed average slope of 62%. Also, the thresholds for the two mirrors differed by almost exactly a factor of two, which one would expect for a low-loss system. To date, we have no explanation for the low slope efficiency.

The ring laser was tunable, by adjusting the alignment of the cavity mirror nearest the crystal, over the range 740 - 820 nm. Both the short- and long-wavelength limits were determined to be set by rolloffs in the reflectivity of the cavity mirrors.

We examined the temporal behavior of the Ti:Al$_2$O$_3$ laser by detection of the output with a high-speed silicon photodiode and observation of the waveform on a Tektronix high-speed storage oscilloscope. Figure 17 shows a photograph of the oscilloscope trace for a single pump and Ti:Al$_2$O$_3$-laser pulse, at a 4.5-mJ output level from the system with a 60%-R output mirror. As expected, the Ti:Al$_2$O$_3$ operated in the so-called gain-switched mode, as a result of the short pump pulse, and produced a single output pulse.

FLAT HR

2 MCC HR

Ti:sapphire
CRYSTAL

60 mm

230 mm

90 mm

FUSED SILICA
BREWSTER PRISM

250 mm

200 mm

2 MCC HR

GREEN PUMP BEAM
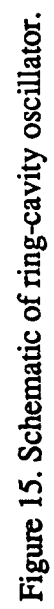
OUTPUTS

60 AND 80% R
FLATS @ 750 NM

Figure 15. Schematic of ring-cavity oscillator.

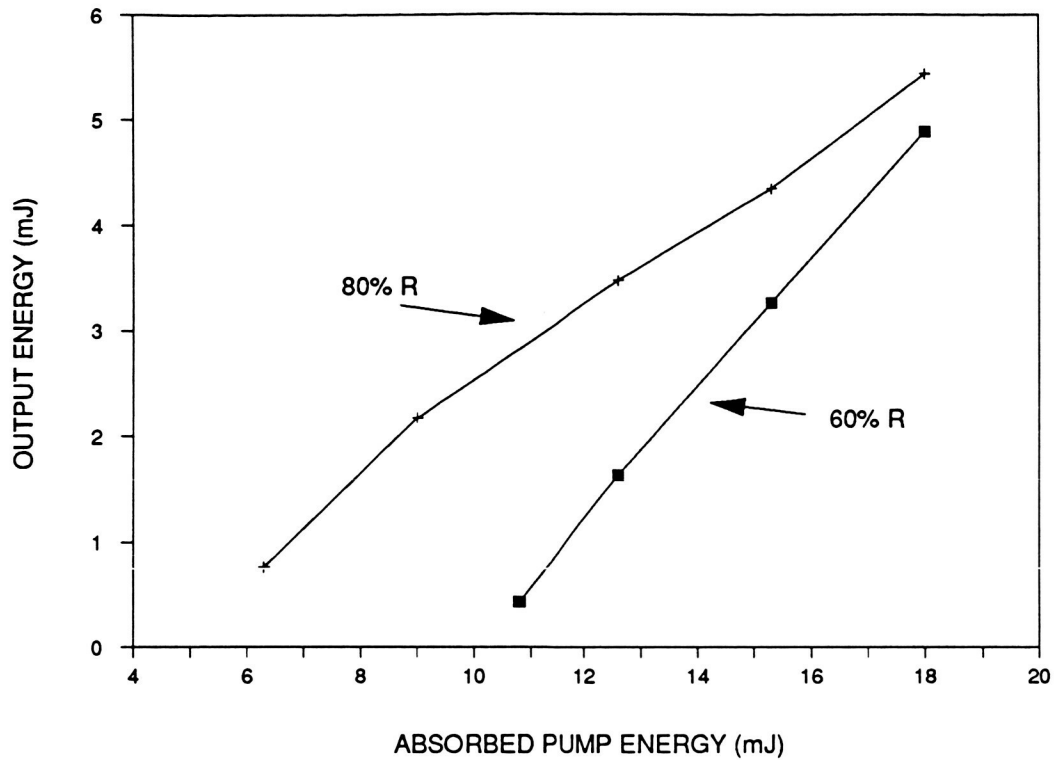Figure 16. Energy input-output curves for ring-laser system,
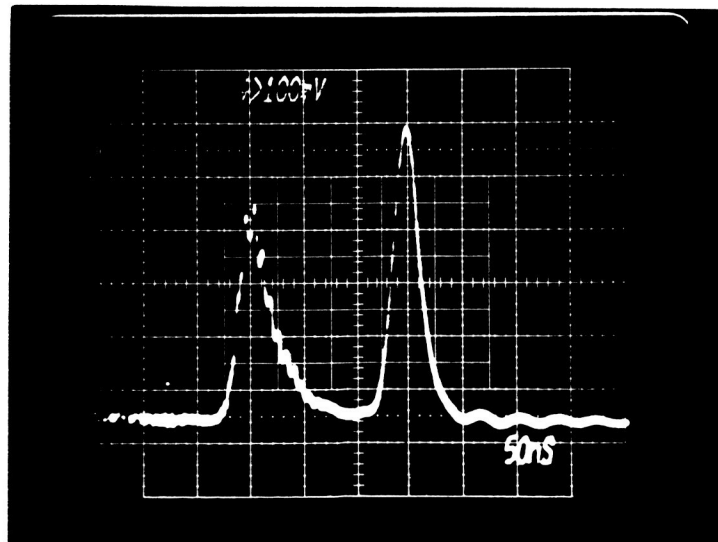from two different output-mirror reflectivities.

Figure 17. Output pulses of pump and Ti:Al_2O_3 lasers.
Structure on pump pulse is due to mode beating.

We were interested in two temporal characteristics of the ring laser, the width of the Ti:Al$_2$O$_3$ output pulse and the buildup time of the pulse, defined here as the delay from the start of the pump pulse to the peak of the ring-laser pulse. We observed these characteristics as a function of the ratio of actual pump energy to threshold pump energy (the pumping ratio), for the two different output mirrors used. The data were compared with the results of a computer model based on the conventional rate-equation approach to laser dynamics, discussed in more detail in Ref. 5. The FORTRAN code for the model, developed initially by Moulton at M.I.T. Lincoln Laboratory, was transferred over to an IBM PC, optimized for reduced computation time and enhanced with the addition of a menu-driven user interface and a graphical display of the results. Parameters used in the model included the upper-state lifetime of Ti:Al$_2$O$_3$, the relative number of photons present in the cavity at the beginning of the pump pulse (i.e. the noise level) and the cavity lifetime, with the latter determined by the cavity transit time and the loss per transit. Given the high slope quantum efficiencies observed experimentally, we can assume that the loss per transit is dominated by the output-coupling loss, especially for the 60%-R output mirror. In the calculations we set additional one-way cavity losses at 3.5%.

Figures 18 and 19 show the observed and calculated output pulsewidths of the ring laser as a function of pump ratio for the 60%-and 80%-R mirrors, respectively. The agreement between data and theory is good, considering that the effect on pulsewidth of the cavity noise level is minimal and thus there were essentially no adjustable parameters in the model. At low values of pumping ratio the agreement has more of an element of chance, since the sensitivity of the pulsewidth to the actual ratio is high, and the error in establishing the actual ratio is high as well. In general, the observed pulsewidths were longer than the model predicted. Some if not all of this result may be due to the simplifications of the model, which assumes that only one mode of the cavity oscillates or that all modes which build up from the noise have the same loss and therefore the same threshold pump energy. In fact, there is a distribution of losses, not all of the modes build up at the same rate and the output pulse would be expected to be broader than a pulse calculated under the equal-loss assumption.

Figures 20 and 21 present a comparison of the observed and calculated buildup times for the 60%-and 80%-R mirrors, respectively, again as a function of pump ratio. In Fig. 20 we show the calculated buildup time for two cavity noise levels, one in which there is only one photon in the cavity mode, and another in which there are approximately 10^4 photons. Clearly, better agreement is found at the higher initial photon level. The calculated buildup time shown in Fig. 21 is based on a noise level of 10^4 photons. If the laser buildup was truly from a thermal background then one would expect that the proper noise level would be a single photon. We believe that the experimental results reflect the fact that a fraction of the spontaneous emission induced by the pump couples into the laser cavity, effectively creating a much higher noise level than that from the thermal background. The relatively short lifetime of Ti:Al$_2$O$_3$ results in a much higher spontaneous emission rate for a given excited state population, compared to other solid state lasers such as Nd:YAG or alexandrite. The actual calculation of coupling between spontaneous emission and the optical cavity is complicated and was not carried out, but would be of interest in future research efforts to confirm our observations.

22
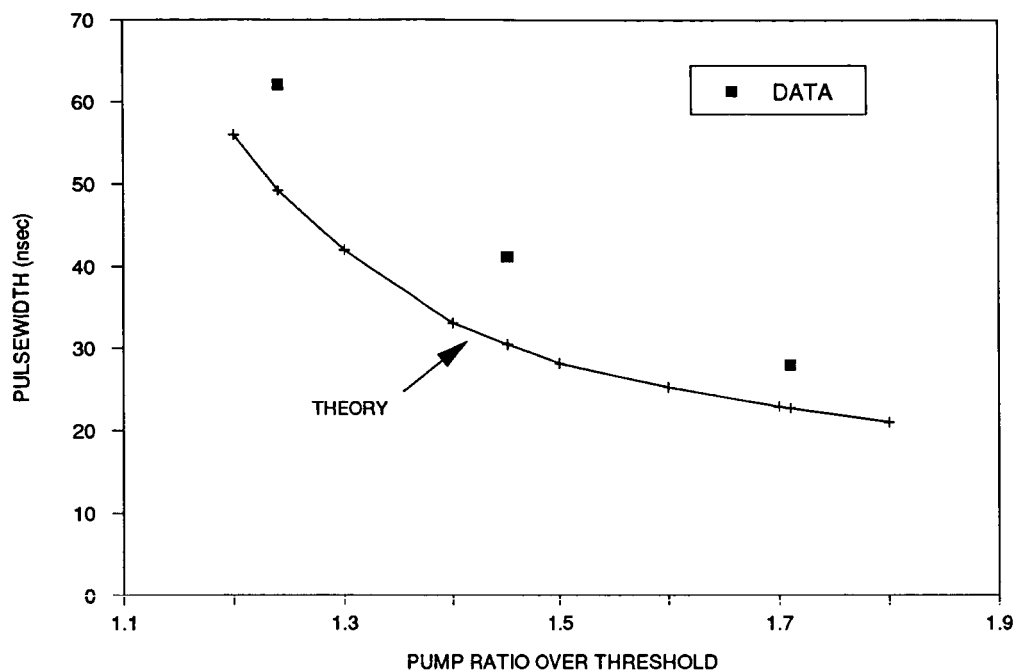
Figure 18. Observed and calculated ring-laser output pulsewidth
for the 60%-R output mirror.
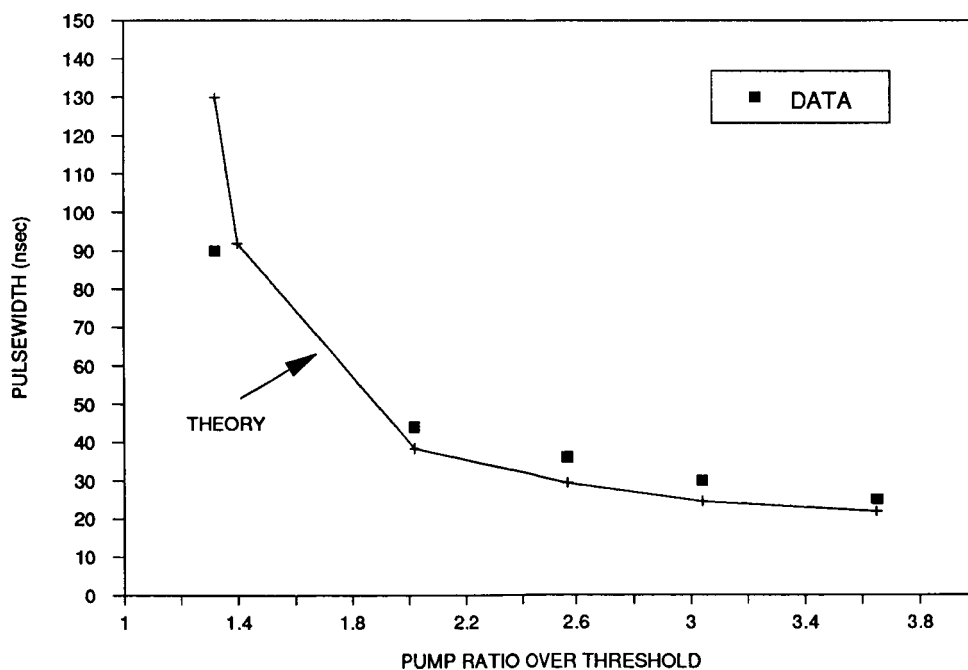
Figure 19. Observed and calculated ring-laser output pulsewidth
for the 80%-R output mirror.

23
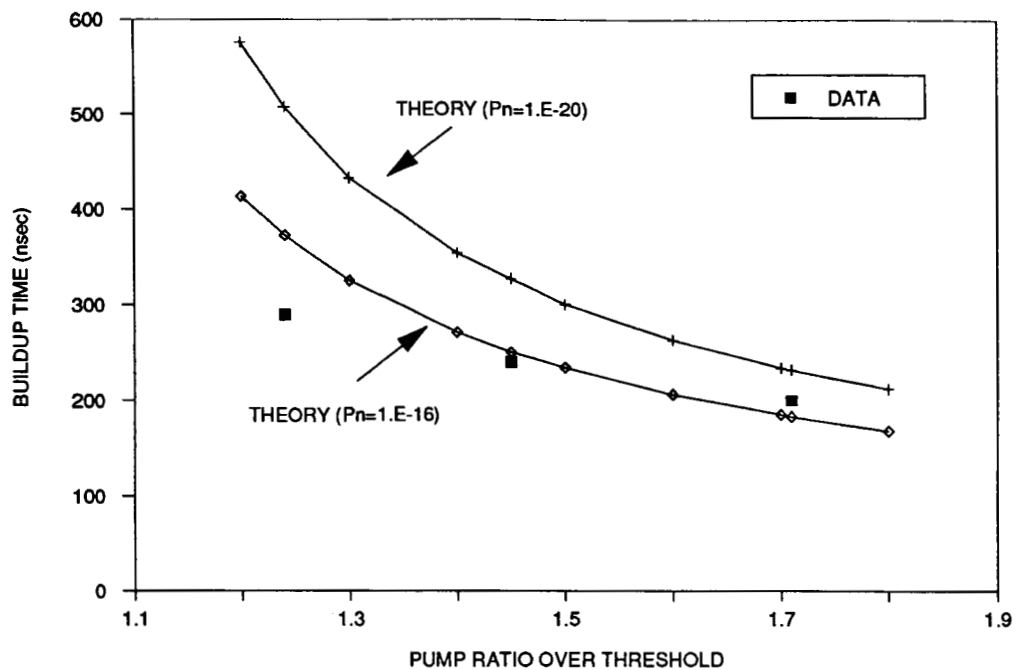
Figure 20. Observed and calculated ring-laser pulse buildup time for the 60%-R output mirror. Calculations based on two different levels of assumed cavity noise level are shown.
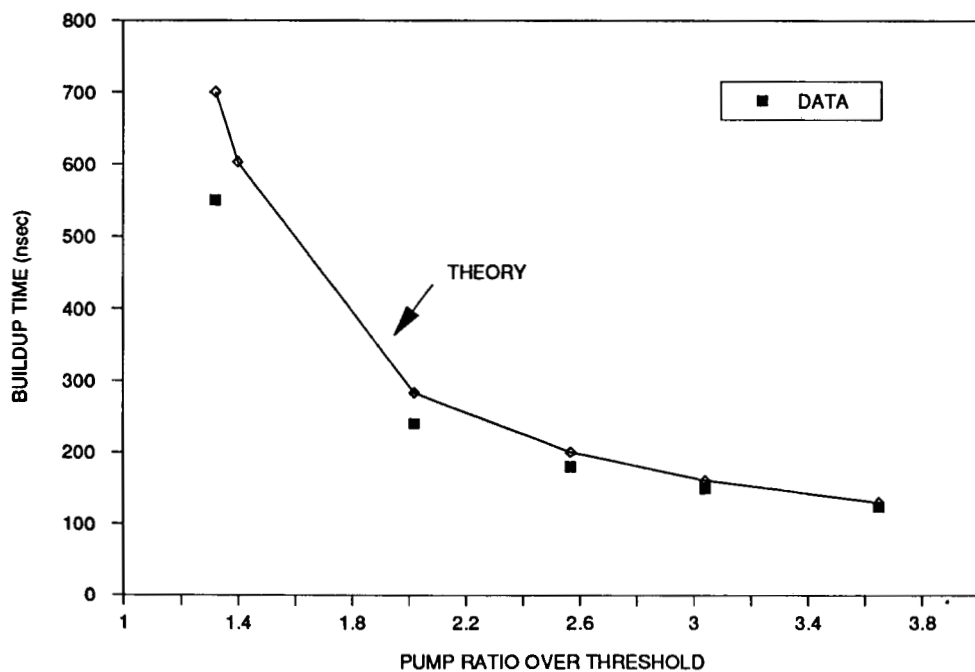
Figure 21. Observed and calculated ring-laser pulse buildup time for the 80%-R output mirror.

We studied the spectral behavior of the Ti:Al$_2$O$_3$ ring laser by use of a 1024-element, self-scanning silicon diode array placed at the exit plane of a 0.68-m grating spectrometer (ISA HR-640). The array allowed observation of the spectral nature of the Ti:Al$_2$O$_3$ laser on a per-pulse basis, with a resolution of approximately 30 pm. The output of the array was fed into a Data Precision 6000 waveform analyzer, where it was digitized and output in digital format to an IBM PC for examination and plotting.

Figure 22 shows the emission spectrum for the ring laser at a 3-mJ output level. For this and the spectral data presented below, the laser output mirror reflectivity was 80%. The emission is spread over a bandwidth of approximately 10 nm, with similar results observed over the range from 1.4x to 4x threshold. As is discussed in more detail in the following Section, because the Ti:Al$_2$O$_3$ transition is homogeneously broadened one would expect that mode competition would result in a narrow-linewidth output, if the laser was allowed to reach an equilibrium condition. However, under the conditions of short-pulse pumping, an equilibrium condition is most certainly not obtained. The buildup time at the 3-mJ output level is 180 nsec, and since the ring cavity path length was 96 cm, the output from the laser was developed after less than 56 passes around the cavity. The large spectral region over which emission is observed is due to a combination of such a small number of passes, the relatively broad spectral response of the intracavity prism tuning element, and the broad linewidth of the Ti:Al$_2$O$_3$ gain medium.
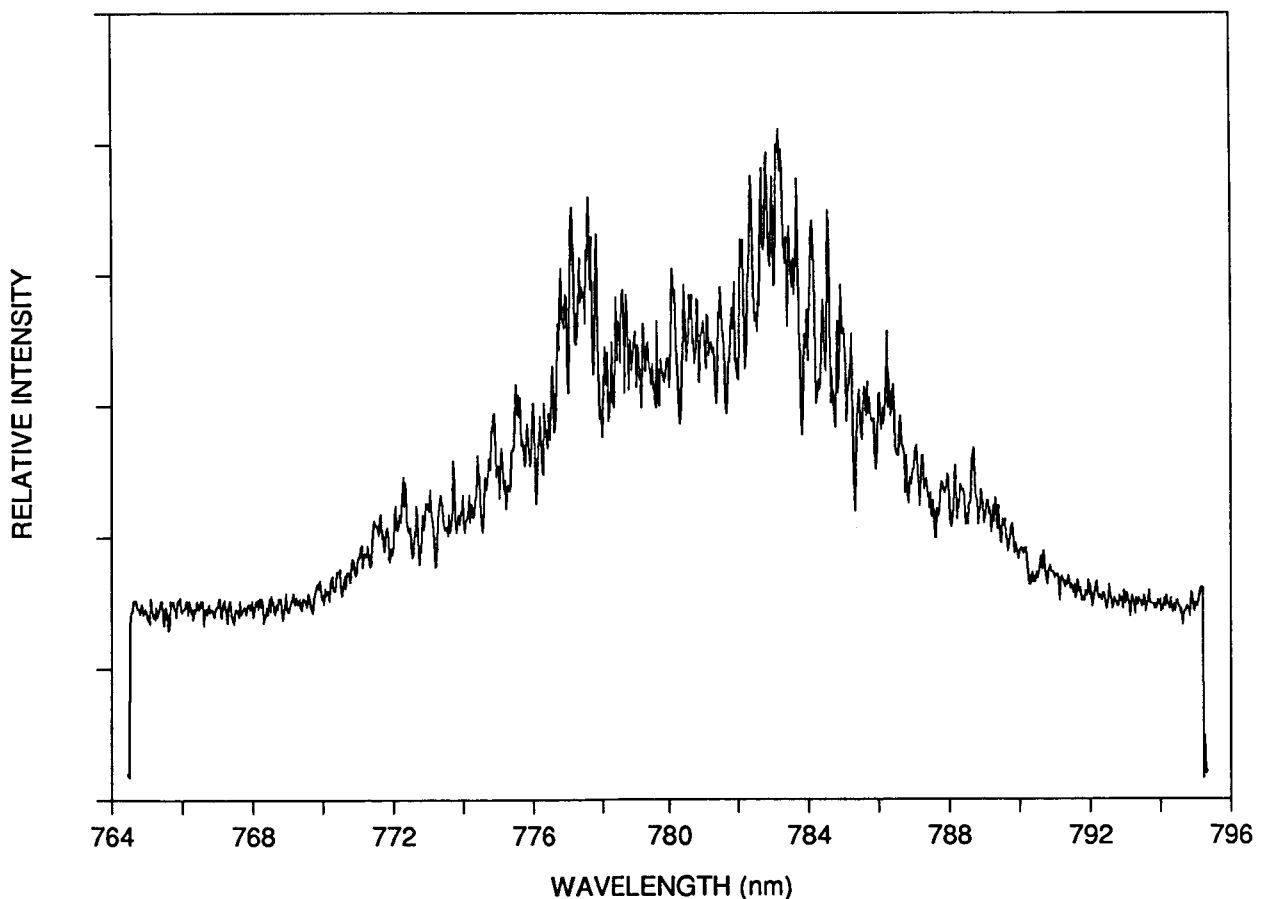
Figure 22. Emission spectrum from ring laser at the 3 mJ output level.

We attempted to narrow the ring-laser linewidth by placing tilted etalons, coated for 20% reflectivity, in the laser cavity. Figures 23, 24 and 25 show the spectral emission at output levels of 0.7, 2.8 and 4.2 mJ, respectively, with a 0.1-mm-thick intracavity etalon. The effect of the etalon was to greatly reduce the number of laser modes oscillating, to clusters around the etalon resonances, but not to limit the total spectral range over which emission was observed. Again, this is consistent with the condition in which mode competition has only partly developed. The output energy at a given pump level dropped approximately 10% with the insertion of the single etalon. In Fig. 24 one can observe the effects of damage to the coated surfaces of the etalon, which reduced the etalon finesse and thus increased the width of an individual etalon resonance. The number of oscillating modes was reduced even further by the use of two intracavity etalons, 0.1- and 0.2-mm thick. The spectra in Figs. 26-28 are at output energies of 0.6, 2.6 and 3.4 mJ, respectively. The output-energy loss was higher with the pair of etalons, with one particular set of data showing that the output at a 20-mJ pump level fell from 4.8 mJ with no etalons to 3.4 mJ with both etalons. We noted that there was a general problem with etalon damage, and operation at the highest energy levels was not reliable. Examination of the widths of the individual lines shown in Figs. 26-28 showed that they were three pixels in width, corresponding to a 90-pm linewidth. The grating-spectrometer resolution should have been better than 90 pm (the grating used was 1200 g/mm and the entrance slit was opened only about 10 microns) and thus we conclude that each of the lines appearing in the spectrum does not correspond to a single frequency.
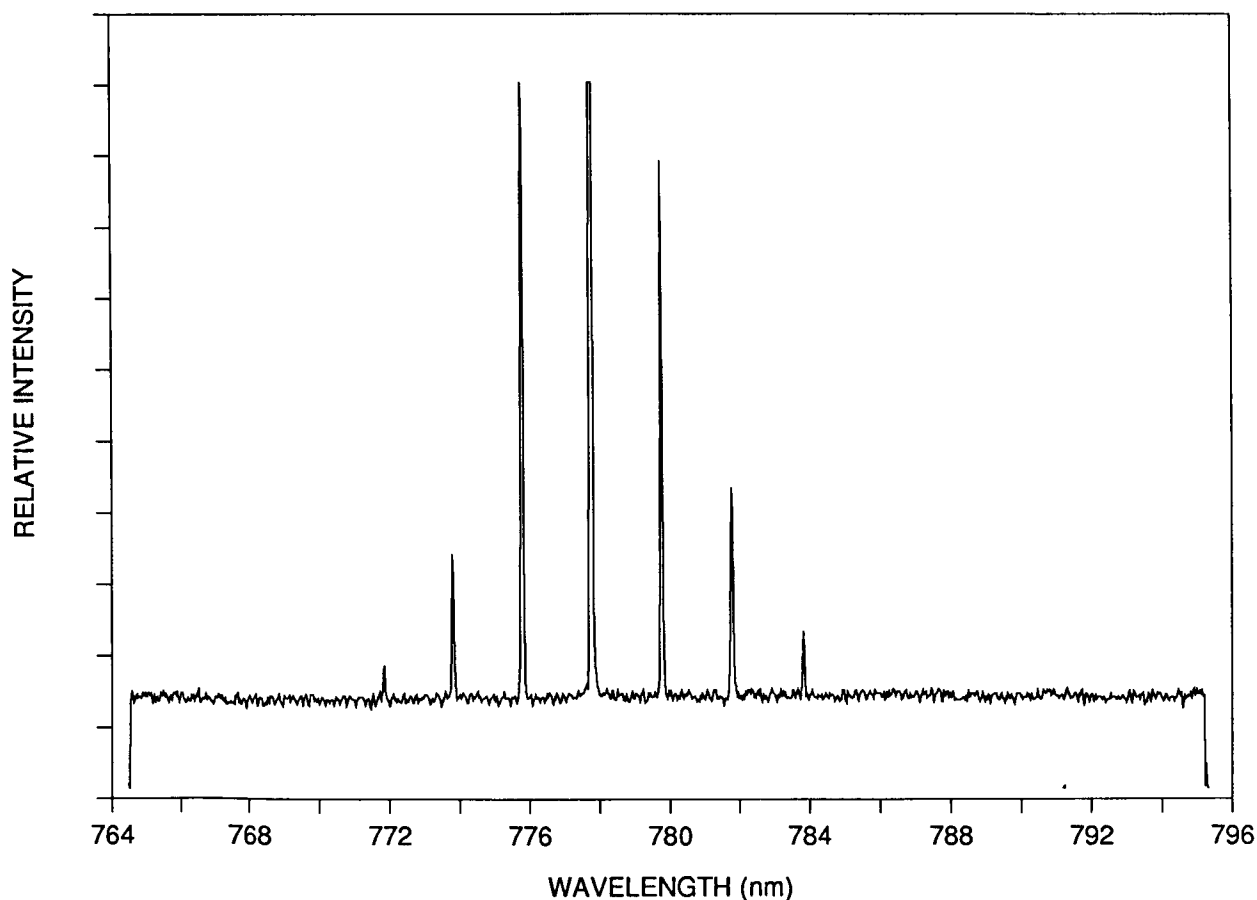
Figure 23. Emission spectrum from ring laser with 0.1-mm-thick etalon, at the 0.7-mJ output level.
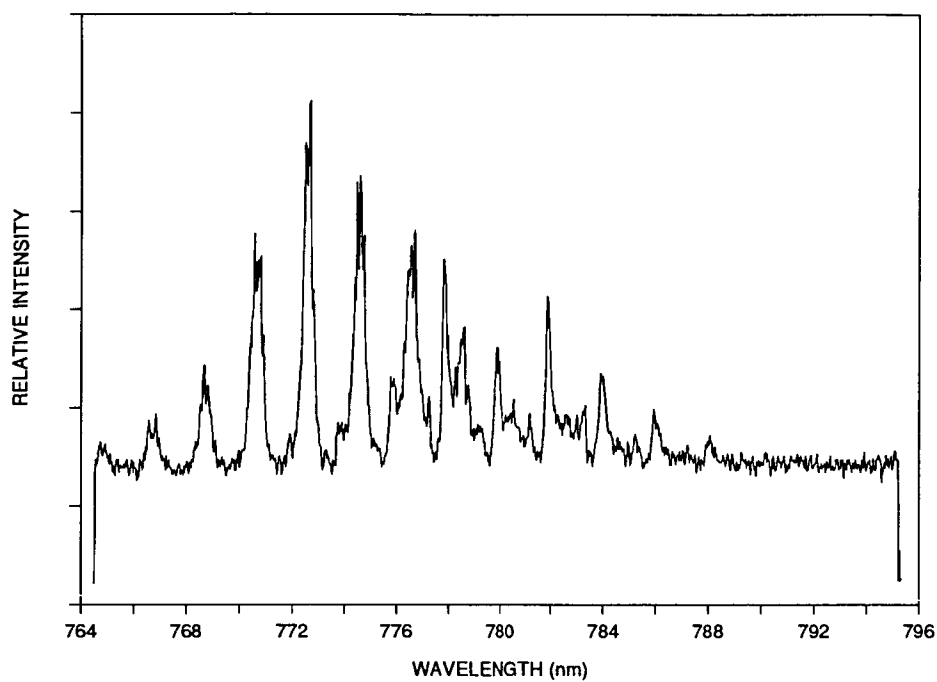
Figure 24. Emission spectrum from ring laser with 0.1-mm-thick etalon, at the 2.8-mJ output level.
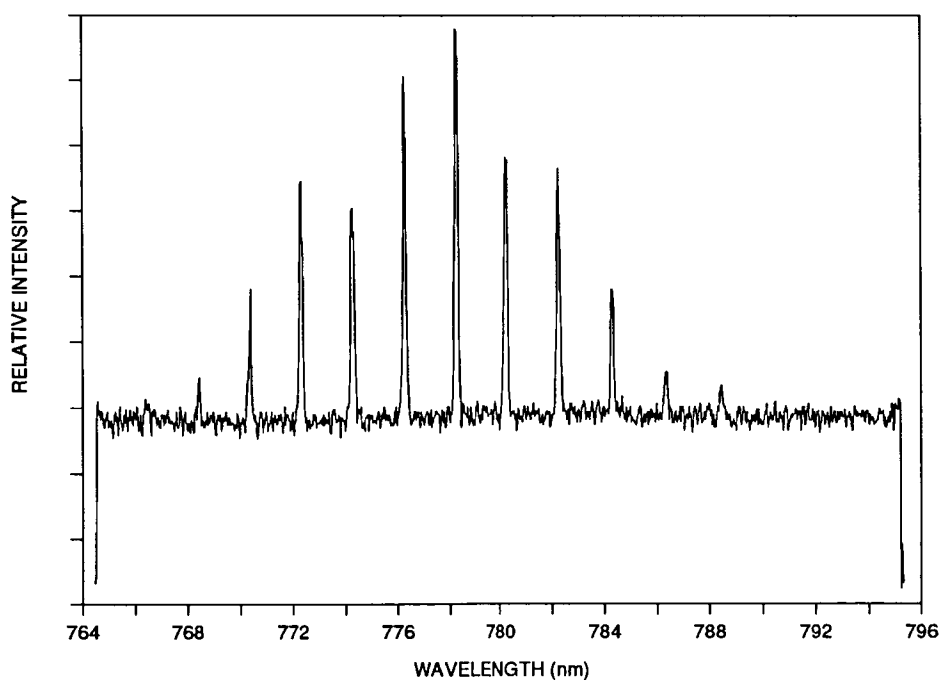
Figure 25. Emission spectrum from ring laser with 0.1-mm-thick etalon, at the 4.2-mJ output level.

27
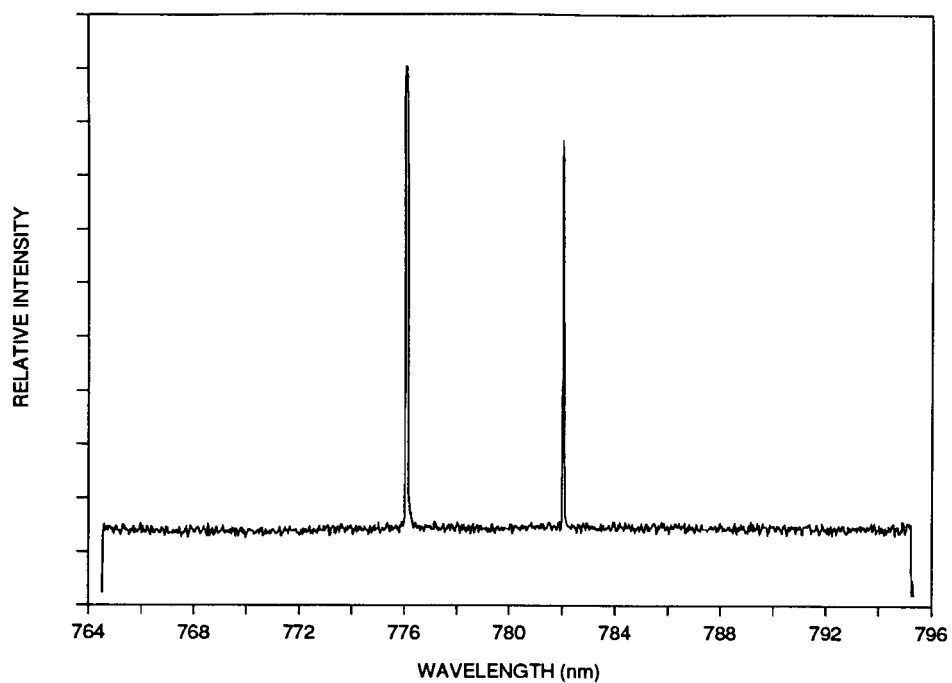
Figure 26. Emission spectrum from ring laser with 0.1-mm- and 0.2-mm-thick etalons, at the 0.6-mJ output level.
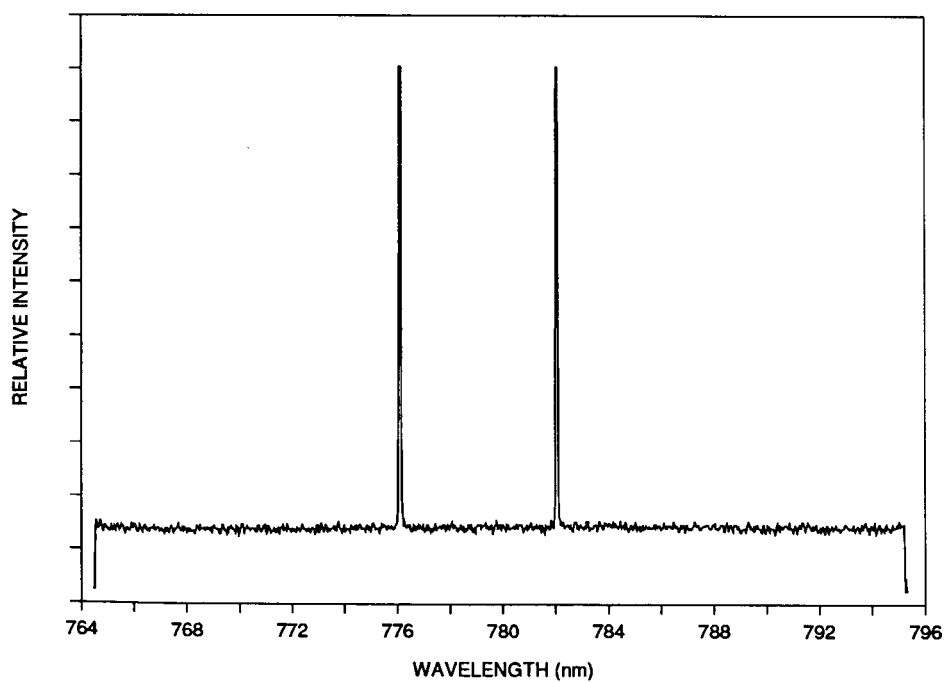
Figure 27. Emission spectrum from ring laser with 0.1-mm- and 0.2-mm-thick etalons, at the 2.6-mJ output level.

28
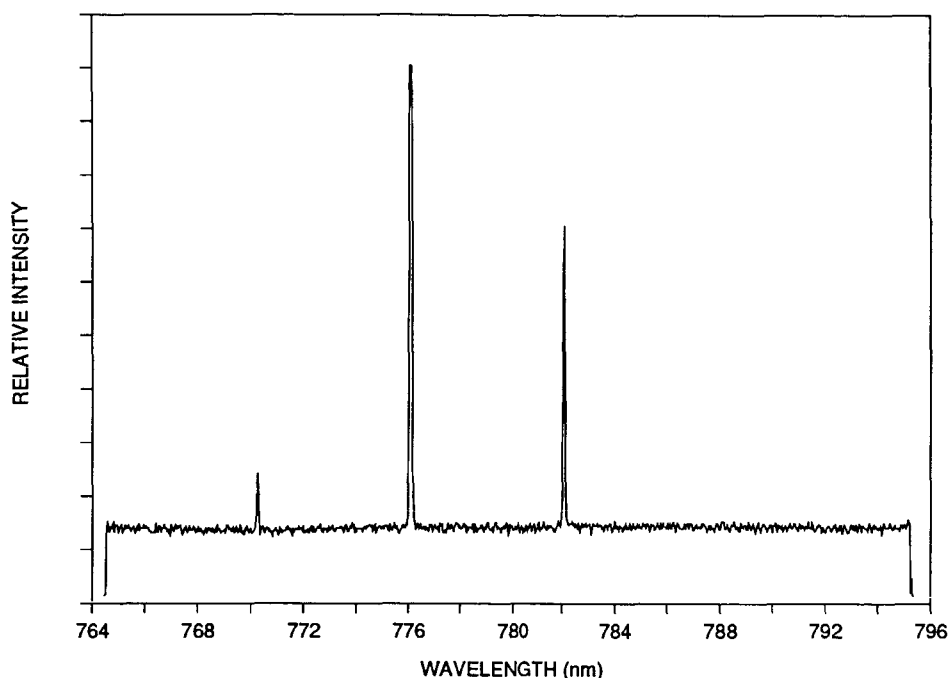
Figure 28. Emission spectrum from ring laser with 0.1-mm- and 0.2-mm-thick etalons, at the 3.4-mJ output level.

It might have been possible to observe single-frequency operation from the ring laser if we had employed higher-finesse etalons, but the higher circulating power inside the higher-finesse elements would have aggravated the damage problem even further. Our analysis of the ring laser results confirmed the conclusion that injection-locking of the Ti:Al$_2$O$_3$ laser was the best approach to obtaining truly narrow-linewidth operation. We attempted an experiment in which the output of a commercial, 20-mW, single-frequency diode laser (Sharp LT024) operating at 780 nm was injected in one direction into the ring laser. The diode output was focused into a pinhole and then collimated and mode-matched into the ring laser. The pinhole was used to provide a crude method of isolation between the diode and ring cavity. By adjusting the focal spot of the diode on the pinhole we could vary the level of coupling between diode and Ti:Al$_2$O$_3$ lasers. We directed the output of the ring laser (with the etalons removed) into the spectrometer-diode-array detection system and observed the real-time spectra as we coupled more energy from the diode into the ring laser. A single sharp line was clearly evident in the output and was of many orders-of magnitude greater intensity than the level produced by the diode alone. The line grew in intensity as the coupling increased but a certain point there was enough feedback from the ring laser to the diode to cause facet damage, and the diode ceased laser operation. In principle, if the diode was perfectly mode-matched both spatially and in frequency, the ring laser should not oscillate in the reverse direction and feed back energy to the diode. We concluded that a Faraday isolator between the diode and ring would be required for protection of the diode under actual experimental conditions, since perfect mode-matching could not always be guaranteed. Purchase of a Faraday isolator was not possible given the scope of the study, and we did not carry out further injection experiments.

4.4 Conceptual design of a narrow-linewidth oscillator

4.4.1 Background

The Ti:Al_2O_3 gain medium exhibits an unusually large gain bandwidth, due to the strong vibronic interaction between the electronic levels of the Ti^{3+} ion and the Al_2O_3 host crystal. The presence of narrow zero-phonon lines in low-temperature fluorescence spectra[1,5] confirms that essentially all of the Ti^{3+} ions are in the same crystalline environment and thus the laser transition is spatially homogeneous in nature. The very fast relaxation times (picosecond or shorter) associated with such a strong interaction and the large density of phonon levels assure that, except for perhaps intense subpicosecond pulses, the gain can be considered temporally homogeneous as well. Our experiments on the ring-laser system, described above, confirm the expected homogeneous nature of the laser transition, since the output energy dropped only slightly with insertion of an intracavity etalon, even though the number of modes was substantially reduced. Thus, essentially all of the output of a Ti:Al_2O_3 oscillator can be extracted in a narrow linewidth. How this is to be accomplished is the subject of the discussion to follow.

4.4.2 Technical approach

In principal, a homogeneously broadened, single-transverse-mode laser will, under steady-state conditions, oscillate on only a single longitudinal mode, even without mode-selecting elements in the cavity. The mode (modes from this point on in the discussion are assumed to be longitudinal) oscillating has the highest net gain per round trip in the laser cavity and, when equilibrium conditions are reached, the net gain is, by definition, unity. All other modes experience a net gain of less than unity, in some cases only infinitesimally lower. However, when the conditions for laser oscillation are first met, i.e. the net round trip gain becomes greater than unity, energy in the laser cavity is thermal in nature (modified to some extent by spontaneous emission from the laser medium) and thus all longitudinal modes have some level of excitation, even if it is equivalent to only one photon. In the early stages of laser action each mode builds up at a rate dependent on the net gain, governed by the laser gain bandwidth and any mode-selecting elements in the laser cavity. The process of elimination of all but one mode begins as the gain in the active medium begins to saturate and some modes experience a net loss, rather than gain. If there are only very small differences between the net gains among modes a large number of passes through the laser cavity may be required before equilibrium is reached.

Consider the simple case of two modes which have built up in energy. Figure 29 shows the attenuation experienced by the lower-net-gain mode with respect to the other mode, as a function of the number of passes around the laser cavity. Three curves show the function for different ratios of net gain. An attenuation of 10^{-20} would bring an energetic mode back down to below the noise level. Differences in net gain of on the order of 0.1% can be significant only when the number of passes is greater than 10^4, which for typical cavities, with round-trip times of 1-2 nsec, requires 10 μsec of oscillation.

The gain-switched behavior of a Ti:Al_2O_3 laser pumped by a typical 20-nsec-duration pulse from a frequency-doubled Nd laser results in the generation of an output pulse with tens-of-nanoseconds duration. The delay time from the start of the pump pulse to the Ti:Al_2O_3 laser pulse depends on a number of factors but is, as is evident from Figs. 20-21, typically on the order of 100 nanoseconds. Given the large gain bandwidth of the Ti:Al_2O_3 gain medium and resultant small differences in gain among a large number of modes, it is not surprising that in gain-switched operation without mode-selecting elements large output linewidths are observed, since the number of passes through the cavity is less than 100. The ring laser described above, with only a single prism in the cavity, exhibited a linewidth of 10 nm when pumped at twice threshold, which implies that as many as 2×10^4 modes could be oscillating.
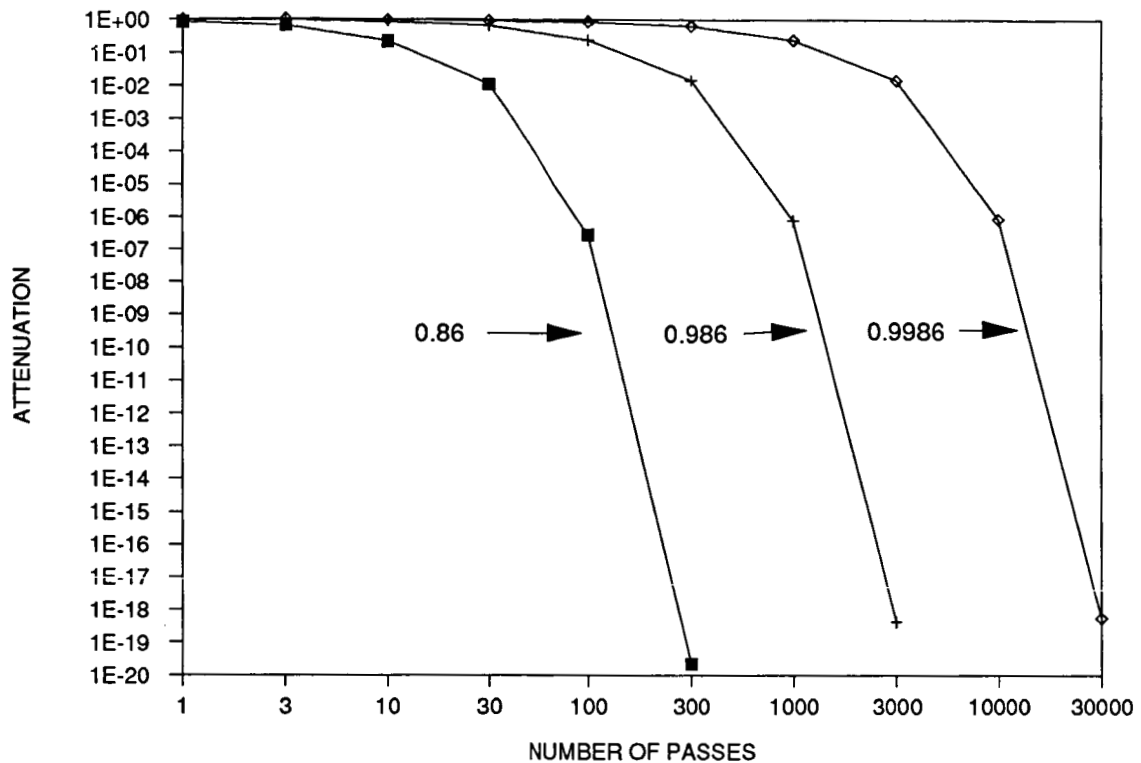
Figure 29. Attenuation of lower-gain mode as a function of the number
of passes, for different ratios of net gain.

NASA has stated that requirement for lidar system linewidths be 0.3 pm at 760 nm and 1.0 pm at 726 and 939 nm. These can be translated to frequency linewidths of 560, 150 and 340 MHz at 726, 760 and 939 nm, respectively. For compact cavities such linewidths allow only one (or perhaps two, for the H_2O bands) modes to be oscillating. For the most accurate determination of the actual laser frequency by a device such as a wavemeter it is desirable that the system be restricted to only one mode. We have therefore chosen, as the design requirement, the attainment of single-frequency operation for the narrow-linewidth oscillator.

We have considered three approaches to obtaining single-frequency output from a Ti:Al_2O_3 oscillator pumped by a frequency-doubled, q-switched Nd laser. The first and most simple involves placing selective elements in the laser cavity with sufficient rejection to prevent energy buildup in all but one mode, even with the relatively small number of cavity passes possible in gain-switched operation. The technology developed for nitrogen- or Nd-laser-pumped, narrow linewidth dye lasers could be considered appropriate for this approach. In designs attributed to Hansch[7], Littman[8] and Meyer[9] some combinations of gratings (either in Littrow or in grazing incidence), beam-expanding telescopes or prisms and Fizeau wedges are used as selective elements. The high insertion losses associated with these elements are easily overcome by the very high gains achievable by dye lasers. Our analysis of dye laser technology applied to the Ti:Al_2O_3 system points out two significant problems. First, the achievable gain in the Ti:Al_2O_3 medium, although higher than in other solid state systems, does not approach that of dye systems, and the high losses associated with some of the tuning elements, especially grazing-incidence gratings, would make the Ti:Al_2O_3-oscillator threshold unreasonably high. Second, the limitations in oscillator output set by optical damage to some of the components would likely limit the output energy to well below a mJ, requiring a more involved amplifier chain in any final system transmitter design. In particular, high-finesse etalons or Fizeau wedges are particularly susceptible to damage, given the high circulating powers inside the elements. The problems mentioned lead us to consider other approaches.

31

One other approach increases the number of effective passes through the laser cavity by adding a q-switch to the laser. If after the pump pulse is applied to the medium the q-switch loss is adjusted to allow the laser to operate slightly above threshold and, after some delay, the q-switch loss is reduced to zero, the pulse generated will have a spectral characteristic determined by the modes selected during the delay period. This 'slowly-opening q-switch' technique has been applied to Nd lasers for line narrowing[10]. Given the 3.2-μsec upper-state lifetime of the Ti:Al_2O_3 medium, one can extend the delay period out to only 1 or 2 μsec without losing a substantial fraction of the inversion to fluorescence decay. Thus the number of cavity passes could be increased to approximately 1000, a definite improvement over the normal gain-switched oscillator. However, the adjustment of q-switch loss to maintain operation during the buildup period just above threshold is extremely critical and becomes more so the longer the period. One must typically employ some type of feedback loop, sensing the laser output with a detector, to obtain stable performance from one pulse to the next.

The other possible approach is to employ a conventional gain-switched Ti:Al_2O_3 oscillator and inject into the cavity of that laser a single frequency resonant (or nearly so) with one of the cavity longitudinal modes. The injection technique, injection locking if the frequency is resonant and injection seeding if the frequency is somewhat off resonance, changes the nature of the gain-switched laser from that of an oscillator building up from background noise to more nearly that of a regenerative amplifier of the injected signal. The injected signal builds up much more rapidly than any noise background and therefore reduces the net gain in the cavity to below the point at which any other frequency can obtain appreciable energy. Injection techniques have been applied to dye, excimer, CO_2, alexandrite and Nd lasers, and, recently, at NASA/Langely, to the Ti:Al_2O_3 system[11]. The requirements for frequency selectivity in the injected oscillator are greatly reduced for reasonable levels of injected power. The injection scheme avoids the need for intracavity etalons in the oscillator and thus should allow higher damage-free levels of output energy. One requires a narrow-linewidth injection source, presumably a Ti:Al_2O_3 laser, which leads to a chicken-and-egg problem if the injecting source is another laser pumped by a frequency-doubled, q-switched Nd laser.

We have chosen to design a narrow-linewidth Ti:Al_2O_3 laser using injection techniques because a) we are concerned that reliable, energetic operation from an oscillator with a slowly opening q-switch may be difficult to achieve and b) we have developed a straightforward scheme for generating the required single-frequency injecting signal. The scheme involves the use of a normal-mode Nd laser which operates with an intracavity doubling crystal to generate a 530-nm pulse of 200-μsec duration. By operating the Nd laser far over threshold one nearly eliminates the relaxation oscillations typically associated with normal-mode Nd lasers, and can obtain a temporally smooth output pulse. A Ti:Al_2O_3 laser pumped with such a pulse operates in the quasi-cw mode with a considerable number of cavity passes (100,000) and can readily be limited to a single longitudinal mode with modest requirements on the intracavity selection elements. Observation of Fig. 29 shows the clear advantage obtained by operation with such a large number of passes in the quasi-cw laser. The consideration of technical effects on laser stabilty, such as pump-induced heating in the laser crystal and microphonics in the laser cavity, discussed in 4.4.3 below, indicates that effects are significant only around the point at which the oscillator has reached single-mode operation.

The complete Ti:Al_2O_3 narrow-linewidth oscillator conceptual design consists of a quasi-cw, single-frequency Ti:Al_2O_3 master oscillator with an associated long-pulse pump laser, a gain-switched slave oscillator pumped by a conventional frequency-doubled, q-switched Nd laser and a Faraday isolation stage used after the output of the slave oscillator. An electronic control system, which could be implemented by a microcomputer, is used to drive the tuning elements. Figure 30 is a block diagram of the entire system and the individual components are described in the following subsections.
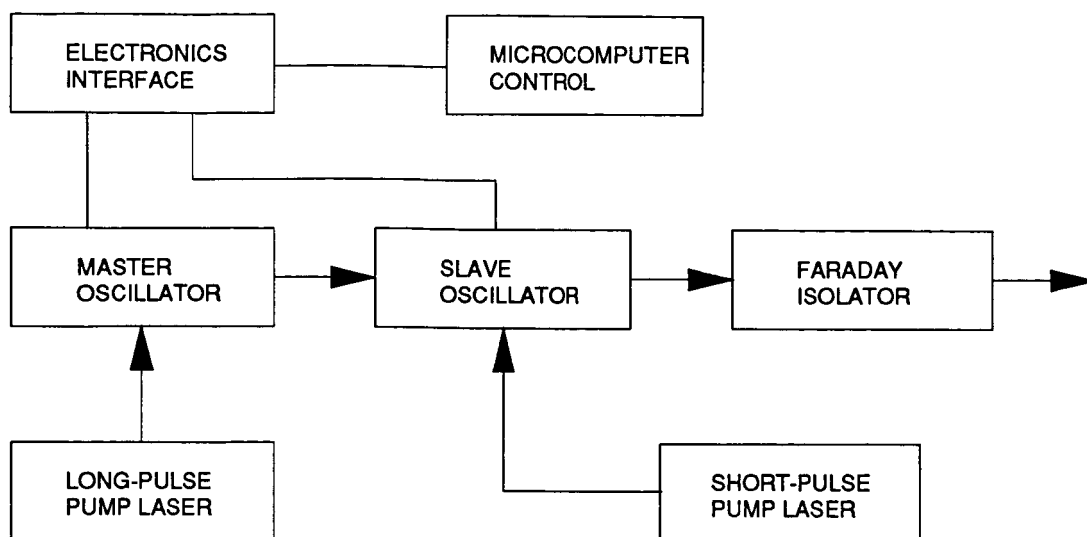
```
┌─────────────────┐          ┌─────────────────┐
│  ELECTRONICS    │──────────│  MICROCOMPUTER  │
│  INTERFACE      │          │  CONTROL        │
└─────────────────┘          └─────────────────┘

┌─────────────────┐   ┌─────────────────┐   ┌─────────────────┐
│  MASTER         │──▶│  SLAVE          │──▶│  FARADAY        │──▶
│  OSCILLATOR     │   │  OSCILLATOR     │   │  ISOLATOR       │
└─────────────────┘   └─────────────────┘   └─────────────────┘
         ▲                     ▲
┌─────────────────┐          ┌─────────────────┐
│  LONG-PULSE     │          │  SHORT-PULSE    │
│  PUMP LASER     │          │  PUMP LASER     │
└─────────────────┘          └─────────────────┘
```

Figure 30. Block diagram of narrow-linewidth oscillator.

4.4.3 Master oscillator

The Ti:Al$_2$O$_3$ master-oscillator design calls for the use of an approximately 200-μsec-long pump pulse, which results in quasi-cw oscillation from the system. Cw operation from the Ti:Al$_2$O$_3$ laser, pumped by an argon-ion laser, was obtained in early experiments with the laser crystal cooled to cryogenic temperatures and quasi-cw operation was observed for a room-temperature crystal by mechanically chopping the pump (Appendix A). Recently, efficient, true-cw, room-temperature operation, with thresholds as low as 1.1 W of incident power, has been observed by workers at Lincoln Laboratory[12]. Since the upper state lifetime of the Ti:Al$_2$O$_3$ medium is 3.2 μsec, pump pulses much longer than this result in quasi-cw operation from the laser, free of sustained relaxation oscillations in the absence of external perturbations. Figure 31 shows the calculated output, based on our standard rate-equation computer model for laser dynamics, of a Ti:Al$_2$O$_3$ laser pumped at twice threshold by a 200-μsec-long rectangular pump pulse. The initial relaxation oscillations damp out in the first 10 μsec of oscillation, leaving a long period of essentially steady-state operation. The initial spike results from the fast turn-on of the model pump pulse, and would not be as pronounced under real pumping conditions.

In order to eliminate the effects of spatial hole-burning, thereby maximizing single-frequency output, the master oscillator design is that of a unidirectional ring laser, a scheme employed in commercial single-frequency dye lasers. Figure 32 shows a schematic layout of the master oscillator. As in other laser-pumped lasers, the system is limited to a single transverse mode by limiting the pumped region in the crystal to that capable of supporting only the TEM$_{00}$ mode. An optical diode, consisting of a length of Faraday rotator material in a magnetic field and a quartz crystal compensation plate, assures that the ring laser operates in only one direction, with only a travelling wave in the cavity. The laser is tuned by three elements, a birefringent filter, an air-spaced etalon with spacing set by a piezoelectric element (a tunable etalon), and a cavity mirror mounted on a piezoelectric element. The design philosophy for tuning takes advantage of the long oscillation time of the laser, and requires only modest rejection of unwanted modes to assure single-frequency operation. The criterion used for rejection is that the unwanted modes have a transmission in one pass through the cavity at most 0.995 times the transmission of the desired mode.
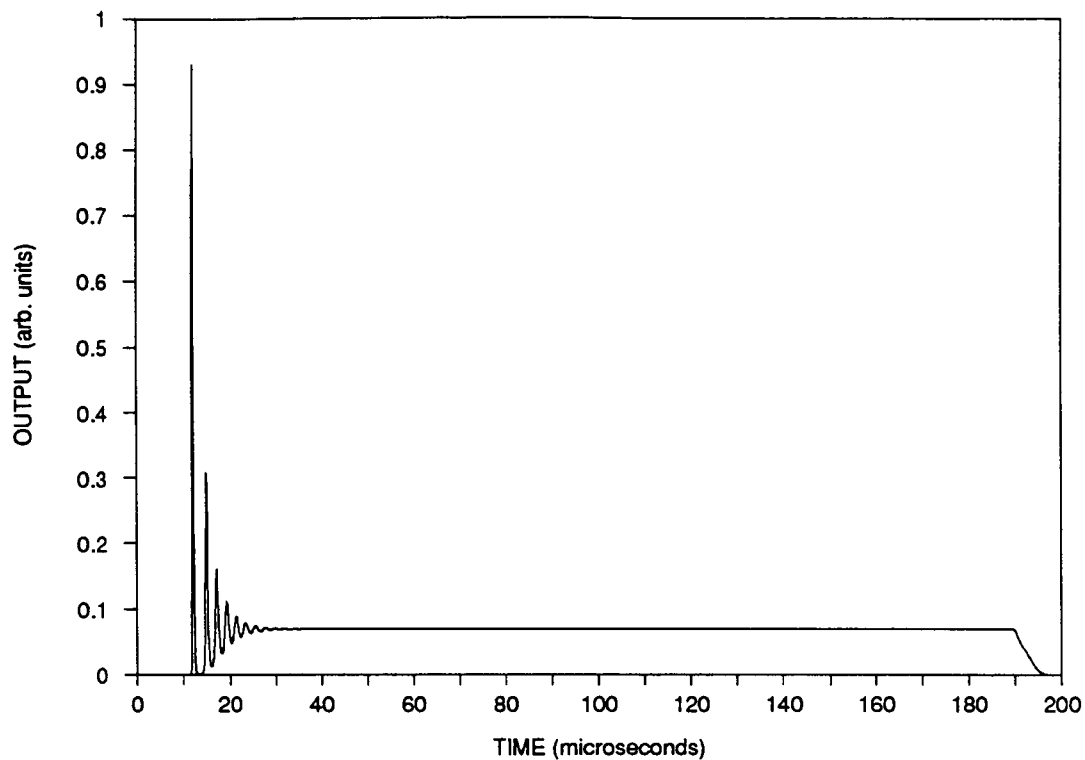
Figure 31. Calculated temporal output of Ti:Al$_2$O$_3$ oscillator pumped by 200-μsec-long pulse.
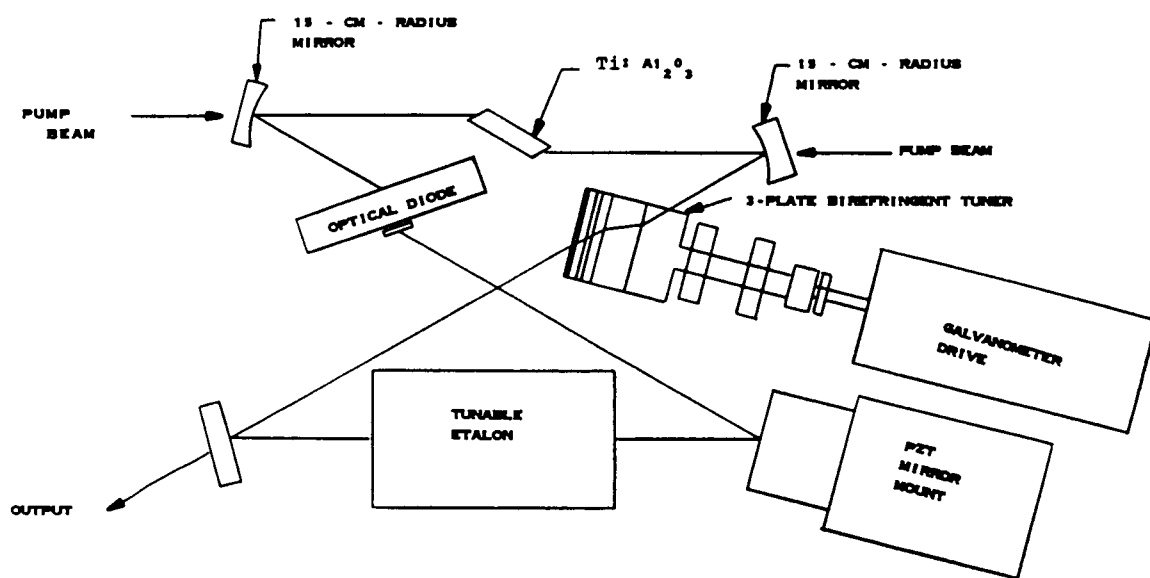

Figure 32. Optical design for master oscillator.

34

For the system shown in Figure 32, the current state of coating technology does not permit the use of one set of cavity mirrors over the 710-950-nm range. It is assumed that three different sets of coatings would be required, with one set allowing oscillation from 710-800 nm, another set covering 800-900 nm and a third set usable from 900-950 nm. In order to simplify the operation of the master oscillator the different coating sets would be applied as different segments on a given cavity mirror, allowing a change in the operating region by simple rotation of the mirror in the mirror mount.

The cavity spot size in the crystal is designed to be 100 μm in radius and we have chosen the use of a 75-μm-radius pump beam to minimize the threshold and yield a high slope efficiency, based on criteria previously developed for longitudinally pumped lasers[5]. The crystal to be used is 2-cm long and doped to absorb 80% of the pump energy. Assuming a single-pass loss in the cavity of 2.5%, an output-mirror transmission of 2.5% and an absorption of 75% of the pump energy, we calculate thresholds ranging from 3.6 mJ to 14.8 mJ of incident energy in a 200 μsec-long pulse, over a gain cross section range of 1-4 x 10^{-19} cm^2. The cross section range covers the desired tuning span, as well as uncertainties in the absolute cross section. The operating point for the master oscillator is set at twice threshold, which results in estimated peak output powers of 4-11 W over the 710-950-nm region. We assume the single-pass loss from the various cavity elements to be about 1.5%, which requires the use of a Ti:Al$_2$O$_3$ crystal with a loss coefficient of 0.005 cm^{-1}, a reasonable value given the current state of growth technology.

The birefringent tuning filter is a crucial element in the laser design. We have developed a computer code, based on the use of the matrix formulation for transmission through birefringent media, to carry out an accurate design of the filter. The code is based on an extension of previous work[13] and calculates the equivalent matrix for an arbitrary number of birefringent plates (with arbitrary optic-axis orientation) and any number of Brewster's angle surfaces associated with other intracavity elements, such as the laser crystal. Unlike the previous effort, we solve the eigenvalue equation for the equivalent matrix in order to determine the exact transmission for the two eigenpolarizations as a function of wavelength, a technique employed by Bloom[14] for filters with the optic axis restricted to lie in the plane of the plate. The material chosen for the filter is crystalline quartz, and the design code takes into account the variation in birefringence of quartz with wavelength.

There are many parameters to be specified in birefringent filter design, including number of plates, plate thicknesses, and orientation of the optic axis, and there are only general guidelines available for determining a correct design[15]. We required that the filter tune over the desired range for a rotation angle of less than 25 degrees, into order to use a scanning galvanometer drive, described below. In addition, a narrow linewidth in the immediate vicinity of the transmission peak was desired in order to use only one tunable etalon in the laser cavity. The design arrived at is a three-plate filter with thickness ratios of 1:2:15, a thin-plate thickness of 0.61 mm and plate normals oriented at 35 degrees to the optic axis. The resonances of the filter falling within the Ti:Al$_2$O$_3$ tuning region are shown in Fig. 33, as a function of rotation angle, and show that two sets of orders are present. We determined that a filter design with only one order set covering the desired range would not be practical, as the thinnest plate would be too fragile. The rejection offered by the use of different mirror sets prevents one set of orders from interfering with the other, however. As an example, at a tuning angle of 122 degrees, the filter has resonances at both 790 and 940 nm, but the mirror coatings for the 900-950-nm region would prevent oscillation at the shorter wavelength. The transmission for the two eigenpolarizations at a filter angle of 116.2 degrees appears in Fig. 34. It is interesting to note that the polarizations are purely linear only at the peak transmission points. We have calculated, given the master oscillator operating point over threshold, that the transmission at the various sidelobes shown in Fig. 34 is sufficiently low to prevent oscillation at all but the main transmission peaks, over the entire tuning range of the system.
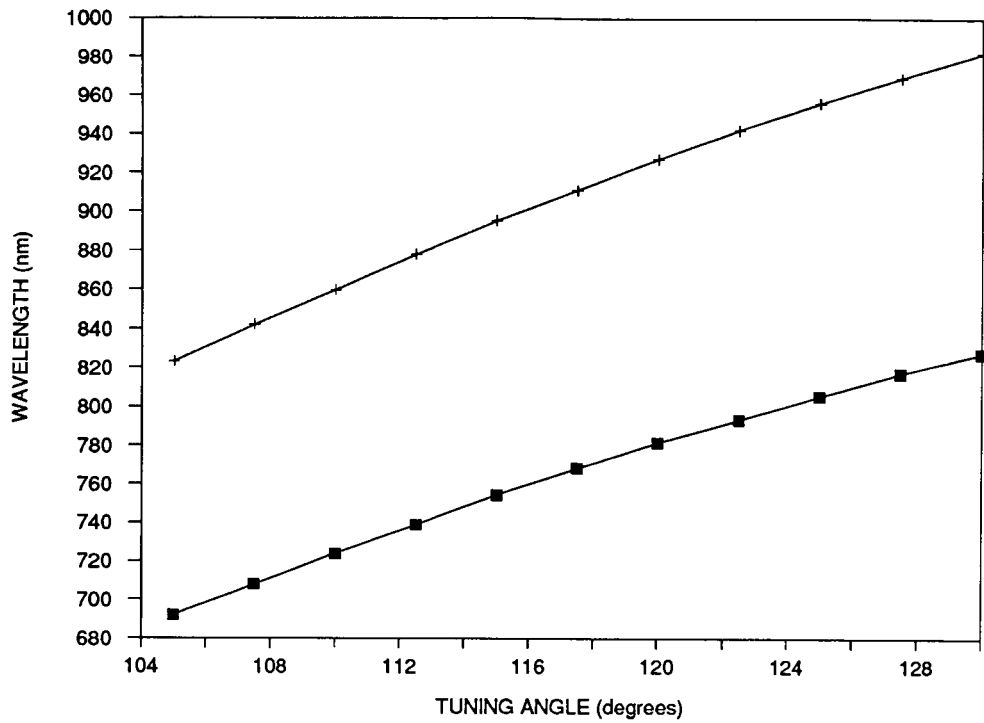
Figure 33. Resonant frequencies of birefringent tuning element, as a function of angle.
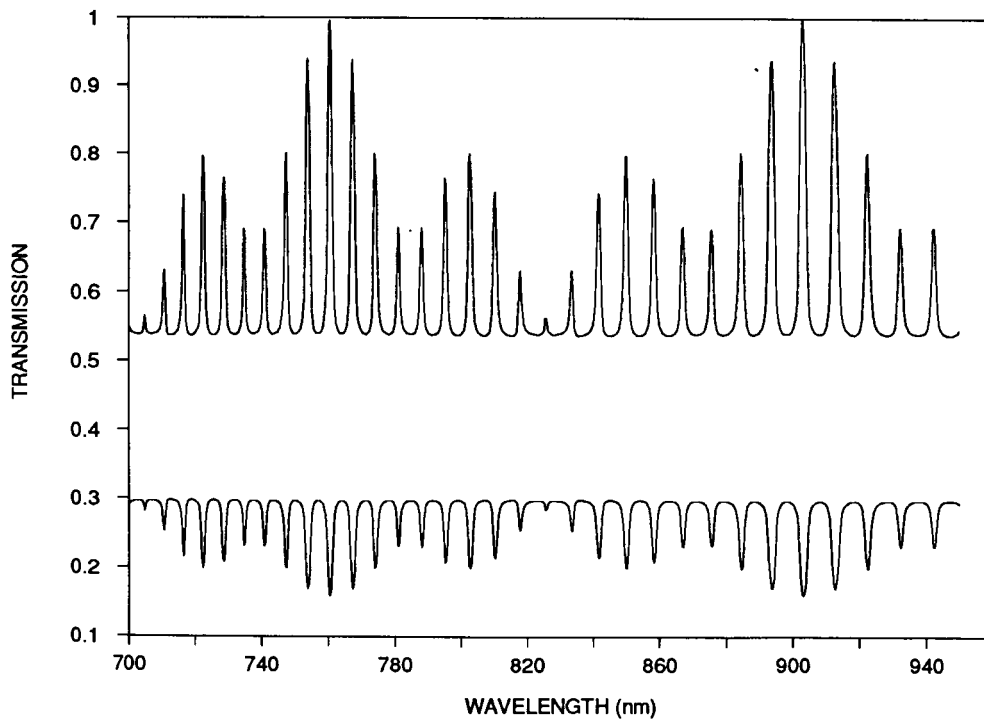
Figure 34. Transmission vs wavelength for two eigenpolarizations of birefringent filter.
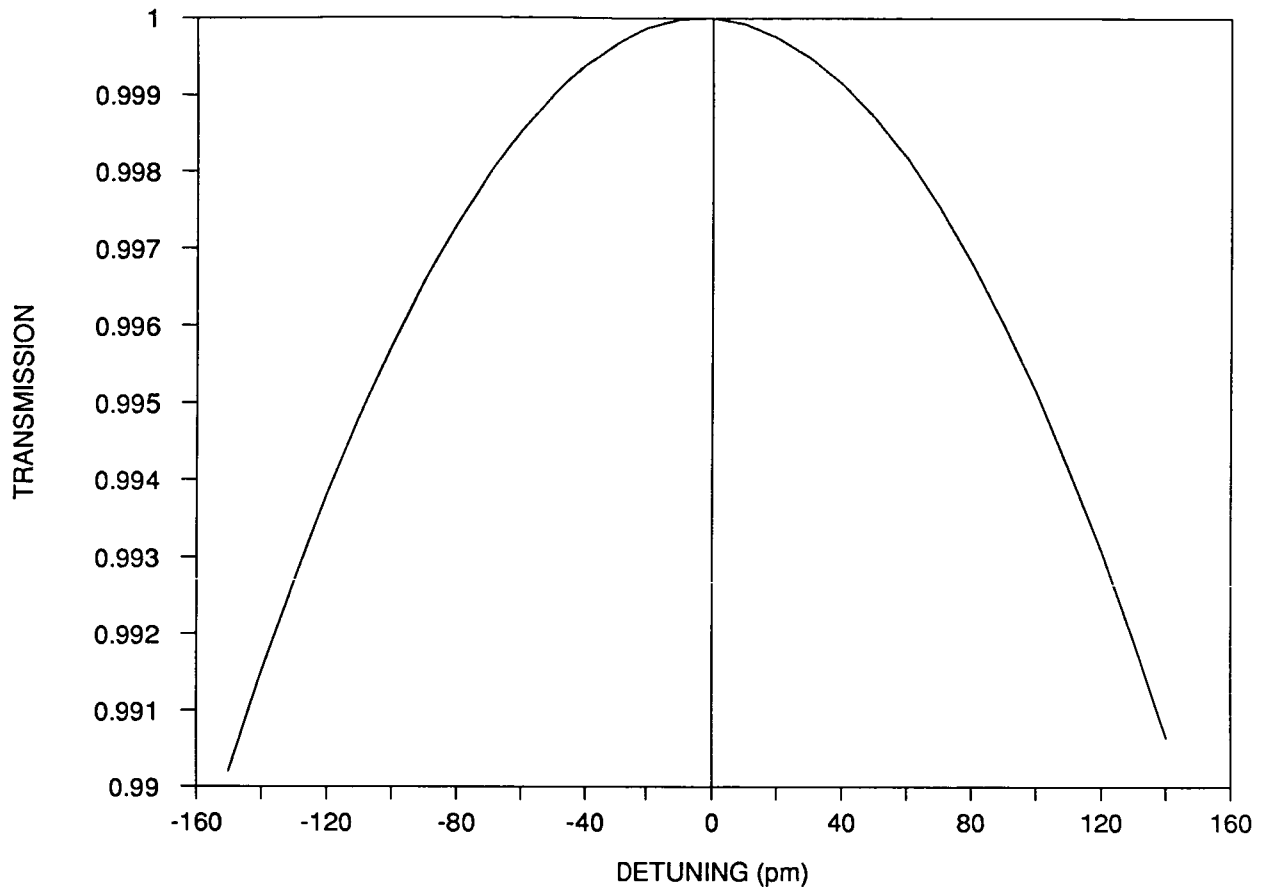
Figure 35. Expanded display around 760-nm peak in Fig. 34.

An expansion about the 760-nm peak in the curve of Fig. 34 appears in Fig. 35 and shows that the full width of the transmission curve to the 0.995-transmission points is 195 pm. The birefringent tuning element exhibits a tuning rate ranging from 4 to 7.6 nm/degree over the span shown in Fig. 34. The element could be rotated by galvanometer scanner (General Scanning, Inc., Watertown, MA, Model G325DT) which is capable of setting an angular position to better than 50 μrad. Given the tuning rates above, the scanner can set the peak wavelength to better than 22 pm, a small fraction of the birefringent-tuner linewidth even in the wavelength region with the highest tuning rate, 840 nm.

In terms of frequency the 0.995-transmission linewidth in Fig. 35 is about 100 GHz. An examination of the transmission curves around wavelengths from 724 to 938 nm shows that frequency linewidths are constant at the 100-GHz level. While the linewidth of the master oscillator operating with only the birefringent tuning element would be considerably narrower than 100 GHz, it is unlikely that the laser emission would collapse into a single frequency, even given the large number of passes in the cavity. Even if it did, the actual frequency would be extremely sensitive to small perturbations in the system, and would rapidly switch from one mode to the other. For stable operation one other tuning element is required to reliably force single-frequency operation.

We have chosen as the element a tilted, air-spaced Fabry-Perot etalon, with the spacing adjustable over at least one wavelength, or free spectral range (FSR) by use of a piezoelectric transducer. The FSR is selected to be 50 GHz, so that if one etalon resonance is set to the peak of the birefringent filter response, adjacent resonances fall at the 0.995-transmission points on either side of the birefringent-filter curve. The finesse of the etalon is required to be high enough to reject all but one longitudinal mode. We have based our analysis of the tilted etalon on a classic paper by Danielmeyer[16], which derived the losses associated with tilting intracavity etalons as well as losses due to scattering and imperfect parallelism. The spacing-tuned etalon offers the advantages of a fixed and sufficiently small tilt loss as well as the simple tuning mechanism made possible by the piezoelectric transducer. The major disadvantage of the air-spaced unit is the need for anti-reflection coatings on the rear surfaces of the mirrors, which limits the spectral range over which the insertion loss of the etalon is low. In order to cover the desired tuning range one could coat the mirrors in a segmented fashion with different coatings, so that different wavelength regions could be accessed by rotation of the device about the tilt axis.

The transmission around resonance of the 50 GHz-FSR etalon is plotted in Fig. 36 for two different mirror reflectivities. As currently configured, the cavity design for the master oscillator (Fig. 32) has a single-pass optical path length of about 65 cm, which results in a longitudinal mode spacing of 0.46 GHz. If we apply the same criteria as before we require a reflectivity between 40 and 50% in order to have a transmission of 0.995 at the frequencies of adjacent modes. It is important to use the minimum etalon-mirror reflectivity needed to obtain reliable single-frequency operation, because the etalon tilt loss increases rapidly with reflectivity. Figure 37 shows the tilt loss as a function of tilt angle for 40 and 50% reflectivities, calculated on the basis of the expected spot size of 0.042 cm at the etalon surface. We have determined that a tilt angle of approximately 2 mrad is needed to prevent feedback from the etalon into the main cavity, and from Fig. 37 it is evident that, at that angle, the loss changes significantly in going from 40% to 50% reflection. It would be useful to conduct experiments to determine if reliable single-frequency operation can be obtained with adjacent mode transmissions greater than 0.995, but the design point used in this discussion assumes that the transmission would be set at that level.

The optical diode shown in Fig. 32 consists of a 1-cm length of Hoya FR-5 (or equivalent) Faraday-rotator glass in a magnetic field parallel to the laser-cavity axis, followed by a 1-mm thick piece of c-axis crystal quartz acting as an optical rotator. For one direction of propagation through the optical diode the rotations induced by the Faraday glass and quartz cancel each other, while in the other direction the rotations add. Therefore, for the direction in which the rotations add, a mode initially polarized in the Brewster plane of the laser exhibits a loss at each of the surfaces in the cavity, while a mode in the direction with rotation cancellation suffers no loss. The largest difference in losses would occur if the rotations added to 90 degrees, but there is some loss differential even for small angles of rotation. For example, we calculate for the system shown in Fig. 32 that the 'wrong' direction would suffer a total loss per pass of approximately 2% for a net rotation of 8 degrees. Examination of Fig. 29 shows that such a loss results in a rapid reduction in amplitude for a mode in the wrong direction, on a time scale of the master-oscillator pulse length. The use of a small differential loss (as low as 0.01%) has been previously employed with cw Nd:YAG ring lasers to establish unidirectional oscillation[17]. In designing the diode we were initially concerned that the device would have to be readjusted at each wavelength for complete rotation cancellation, since both the Verdet constant and the rotary power of crystal quartz are a function of wavelength. We used tabulated data from Hoya and standard handbook data on quartz and discovered that in the Ti:Al$_2$O$_3$ laser wavelength region the wavelength dependence of rotation angle for both materials is the same (inversely proportional to the square of the wavelength), and thus cancellation is essentially wavelength-independent. Once the lengths of the Faraday glass and quartz are established one can always find a magnetic field at which almost exact wavelength cancellation occurs. Figure 38 shows the sum and difference of rotation angles over the 700-950-nm region for a magnetic field of 2350 Gauss, a field easily generated by a small permanent magnet.
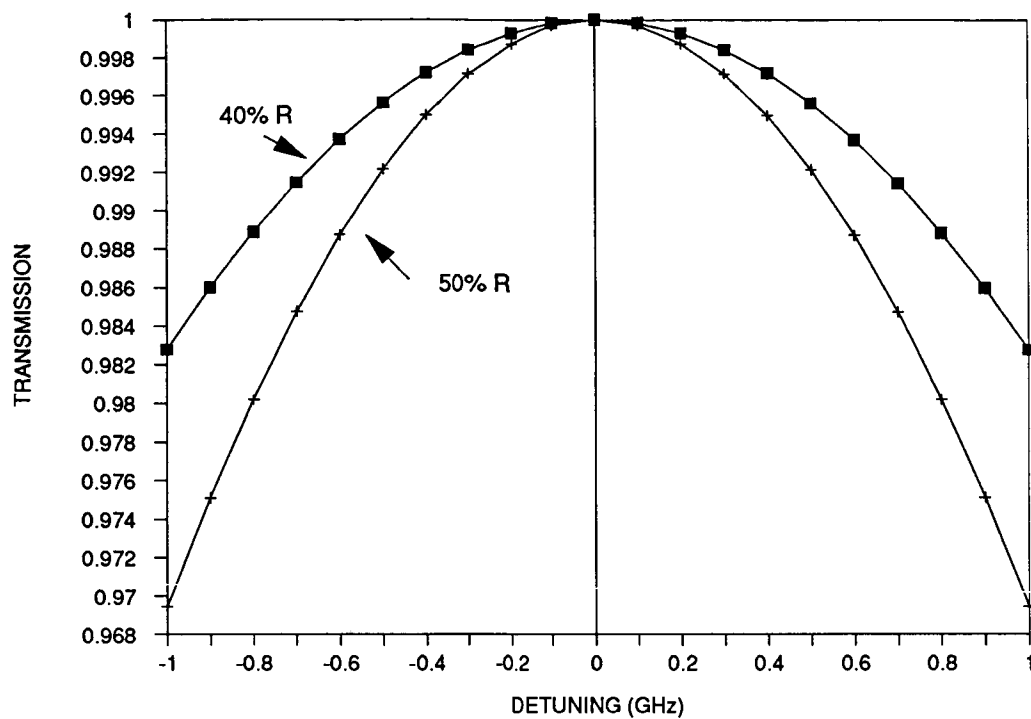
38

Figure 36. The transmission around resonance of a 50 GHz-FSR etalon,
for two different mirror reflectivities.
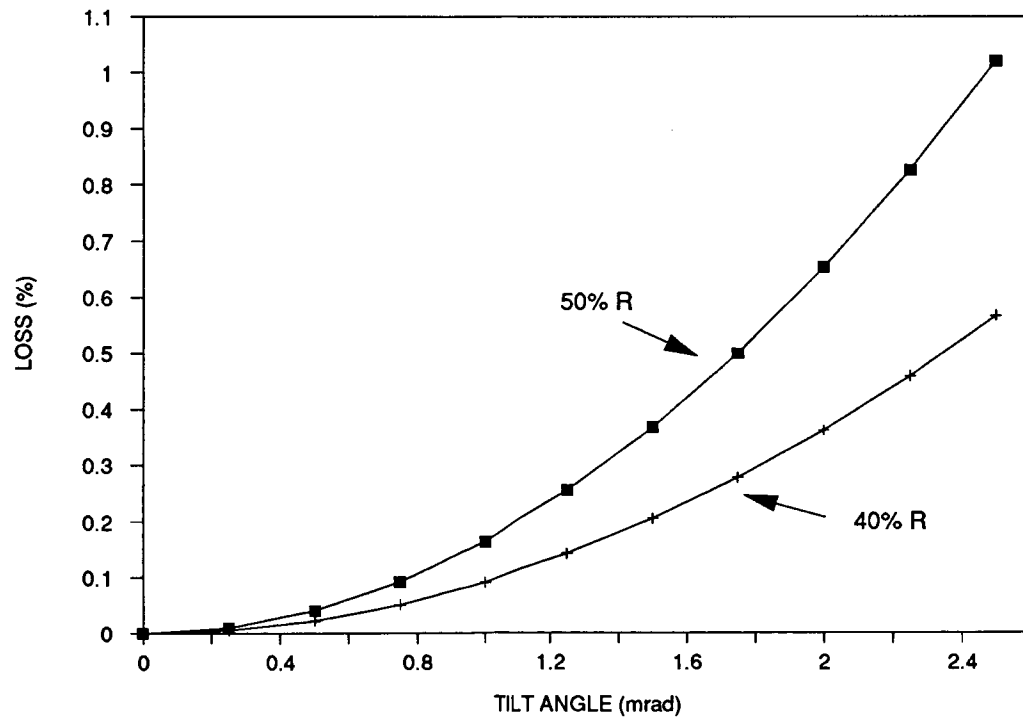
Figure 37. Etalon tilt loss as a function of tilt angle
for 40 and 50% reflectivities.

ROTATION (degrees)

16
15
14
13
12
11
10
9
8
7
6
5
4
3
2
1
0
-1

700   740   780   820   860   900   940

WAVELENGTH (nm)

BACKWARD

FORWARD
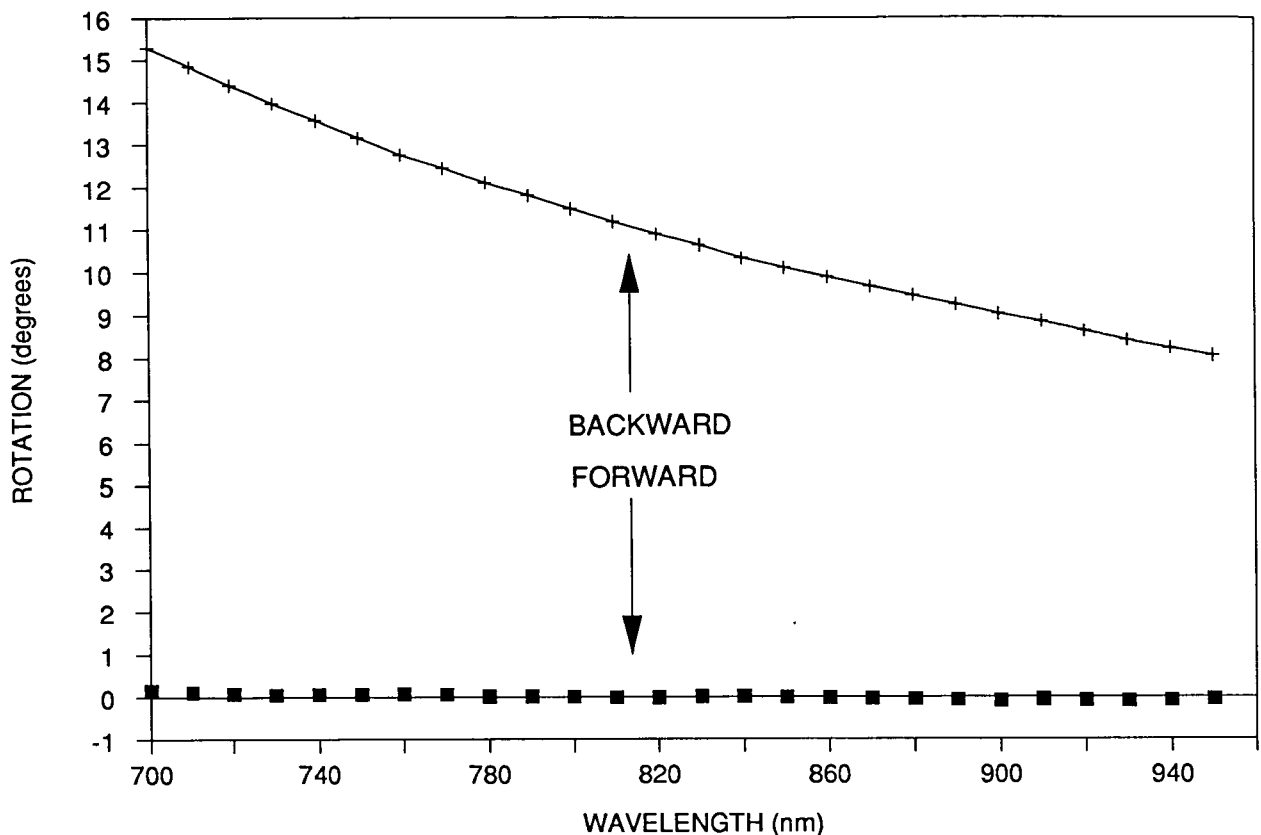
Figure 38. The sum and difference of rotation angles for a combined
Faraday rotator and crystal-quartz plate over the 700-950-nm region.

Proper operation of the Ti:Al$_2$O$_3$ master oscillator requires that a tunable-etalon resonance be centered in the transmission peak of the birefringent filter and that the longitudinal mode frequency of the ring cavity be centered in the peak of the etalon response. As shown in Fig. 32 the cavity mode frequency would be controlled by a piezoelectric transducer on one of the cavity mirrors. The galvanometer drive on the birefringent filter is voltage programmable and thus all the tuning elements could be adjusted by varying an applied voltage. The computer-based electronic control system we envision could, with appropriate software, account for the nonlinear nature of the birefringent element tuning with rotation angle as well as any nonlinearities in the piezoelectric elements. During startup of the system a detector observing the output power of the master oscillator could be used for input to the computer, via an analog-to-digital converter. Output power could be maximized by first tuning the etalon for maximum output and then tuning the main laser cavity.

Actual scanning of the laser wavelength could be done by simultaneous rotation of the birefringent tuner and translation of the piezoelectric elements. Both the etalon and cavity need only be tuned through half a FSR and then reset to operate on another order of the resonance. We have determined that 12-bit resolution is adequate for all the elements and could meet a step-resolution requirement of 0.05 pm, which is equivalent to a frequency resolution ranging from 30 MHz at 710 nm to 17 MHz at 950 nm. If an external system such as a wavemeter is used for wavelength stabilization then the software routine could be modified to accept correction inputs via any number of channels, including RS-232 or IEEE-488.

We have estimated the effects of temperature change on the resonant frequencies of the master-oscillator cavity, the etalon and the birefringent tuning element. For the case of the main ring cavity, we first determine the fractional change in optical path length with temperature of the various solid materials in the cavity and determine the effect on the main cavity resonance by multiplying the change by the ratio of the optical path of the component considered to the total optical path length of the cavity. The results from each solid element are multiplied by the operating frequency, summed together and added to the frequency shift caused by the cavity baseplate expansion. We assume use of Super-Invar for the base. The overall temperature sensitivity of the cavity is estimated (for an operating wavelength of 750 nm) to be 680 MHz per degree C, with the laser crystal and cavity base accounting for a 260 and 145 Mhz/C shift, respectively. Typical commercial tunable-etalon specifications are that the spacing stability is 50 nm/C, which corresponds to a peak shift of 3.3 GHz/C at 750 nm. We have analyzed the stability of the birefringent tuning element and find that the important parameter is the fractional change with temperature of the product of the birefringence and the length of the material. The temperature variation of the birefringence can be estimated from a table in the AIP Handbook[18] to be 1×10^{-6} per degree C, and the resultant fractional stability is 1.1×10^{-4}. At a wavelength of 750 nm, the temperature tuning rate of the birefringent filter is therefore 80 pm/C, increasing to 105 pm/C at 950 nm.

If we assume that an open-loop accuracy of 150 pm is required, it would be necessary to either hold the temperature of the birefringent tuning element stabilized to better than 2 degrees C or to measure the temperature accurately and correct the tuning angle by use of a table in a software control routine. The latter method would appear to be more desirable in that a power-consuming temperature-control system would not be required. The same can be said about maintaining stability of the tunable etalon, in that an oven could be used to hold the resonance frequency stable or software could correct for temperature changes by adjusting the voltage on the piezoelectric element. With no method for dealing with changes in the etalon temperature a requirement for a drift of less than, say, 1 pm/minute could be met only if the etalon temperature changed no faster than 0.1 C/minute. If a software routine was used to correct for changes in the etalon temperature a temperature sensor with a resolution of better than 0.1 C would be needed, a requirement easily met by combining a integrated circuit sensor such as the Analog Devices (Norwood, MA) AD590 with a 12-bit A/D converter. One could maintain the system within an accuracy of 1 pm or so, even without external stabilization. As for the longitudinal mode stability, it could be possible to correct for some of the frequency shift with temperature in a passive manner, as an adjunct to software correction. The cavity optical path length increases with temperature, but a compensating decrease of length with temperature can be accomplished by extending one of the cavity mirrors inward from the pivot point of the mirror mount and taking advantage of the thermal expansion of the material supporting the mirror. The piezoelectric driver for one of the cavity mirrors would be well suited for use in the passive-stabilization scheme. In order to work well the scheme requires that all the elements in the cavity change temperature at roughly the same rate. It would be best to enclose the master (and slave) oscillators in a thermally insulated enclosure, to damp out rapid and unequal changes in temperature in the system induced by the outside environment.

One important issue for the master oscillator is the question of frequency chirp induced by temperature changes in the Ti:Al_2O_3 crystal during the pump pulse. At a 10-Hz repetition rate the amount of average heat dissipation in the laser crystal ranges from 22 mW (2.2 mJ/pulse) at short wavelengths, where thresholds and the energy dissipated per pump photon are low, to a high of 133 mW (13.3 mJ/pulse) at the long-wavelength limit. The peak heat dissipation in a 200-μsec pulse ranges from 11 W to 65 W. As is the case for most heat-flow problems there are no closed-form solutions allowing calculation of both the temperature rise in the crystal and the transient behavior of the temperature during a single pump pulse. If we model the laser medium as a uniformly heated cylinder cooled by heat flowing out the cylinder outer surface then under steady-state conditions the temperature rise from the center of the cylinder to the wall is given by $P/4\pi k$, where P is the power dissipated per unit length and k is the thermal conductivity, which for sapphire is 0.35 W/cm-C. For the highest anticipated average heating of 67 mW/cm, we find

a temperature rise of 0.015 degrees C in the 2-cm-long crystal. If steady-state conditions were reached during the pulse the peak temperature rise would range from about 1.3 to 7.6 degrees C. However, it takes some time to establish a thermal equilibrium, which creates the possibility for a frequency chirp during the laser pulse. We can estimate the time required to reach steady state from a curve in Carslaw and Jaeger[19]. We calculate that the thermal diffusivity of Al_2O_3 is 0.12 cm^2/sec, and given the pumped-volume radius of 75 μm, we observe that 80% of the steady-state heat rise would occur in 140 μsec. At the highest heating rate we find that the last 60 μsec of the output would shift about 320 MHz given the 210 MHz/C tuning shift associated with the laser crystal at an operating wavelength of 950 nm. Although the injection process requires that the master oscillator output be resonant with the slave oscillator only for the buildup time of the slave-laser output, about 100 nsec, the chirp at the long-wavelength limit of the tuning range could present some problems in maintaining frequency control of the master oscillator, and the issue will require further examination.

An additional concern with the operation of the master oscillator could be the frequency jitter induced by mechanical vibrations in the cavity base or mirror mounts. Our experience with other laser-pumped lasers, such as diode-pumped Nd:YAG, indicates that well-designed cavities in a laboratory environment exhibit mechanically induced frequency instabilities on the order of 10 MHz or less. Thus, the major source of frequency instability is the chirp induced by transient heating in the active medium, provided the environment surrounding the laser is relatively quiet.

4.4.4 Long-pulse pump laser

The pump laser for the master oscillator is an internally doubled normal-mode Nd:YAG system, employing the doubling crystal KTP. A schematic of the laser appears in Fig. 39. A similar system with a $LiIO_3$ doubler was operated by a French group[20] and was capable of generating 12.5 mJ of energy in one of the output beams, in a 180-μsec-long pulse free of spiking over all but the first 30 μsec of operation. The spike-free nature of the output is primarily due to operation of the Nd:YAG laser well over threshold, which results in very rapid damping out of any relaxation oscillations.
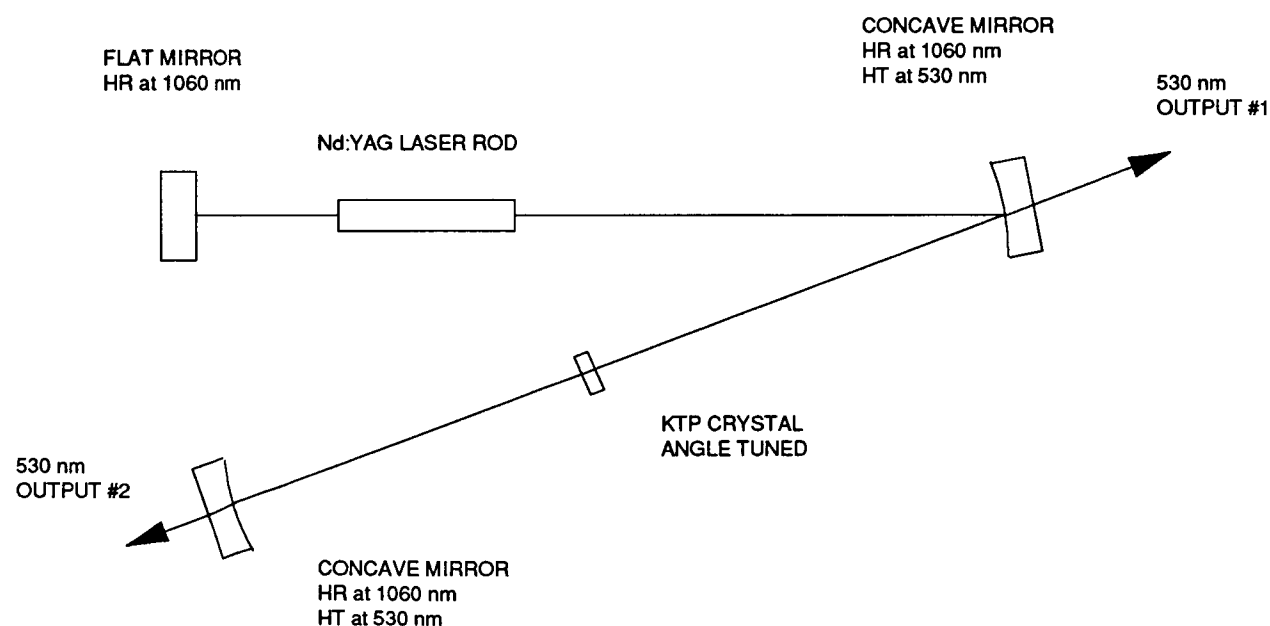

Figure 39. Pump laser for master oscillator.

4.4.5 Slave oscillator

The slave oscillator design is a simple ring-cavity system which uses the $Ti:Al_2O_3$ gain medium configured as a Brewster-angle prism. The schematic diagram of Fig. 40 shows the advantage of the ring system, in that the injection beam from the master oscillator does not undergo any back-reflections from the optics of the slave oscillator, even when perfect mode-matching is attained. The dispersion of $Ti:Al_2O_3$ is used to effect coarse tuning of the cavity by adjustment of the position and angle of a flat mirror mounted on the piezoelectric element. The alignment criterion used is to always maintain a constant boresight of the beam path starting at the flat mirror, reflecting off the concave output mirror and ending at the $Ti:Al_2O_3$ crystal, thereby maintaining a proper and constant alignment of both the injection and output beams. To do this requires that over the entire tuning range the flat mirror be linearly translated a distance less than 1 mm, and rotated in one plane over an angle of 6 mrad. In a spaceborne system appropriate actuators, under computer control, could be used for tuning. As is the case for the master oscillator, we do not anticipate that one set of cavity mirror coatings could span the entire tuning range, and coatings in different quadrants of the mirrors would have to be used to allow full wavelength coverage. The use of different coatings would aid in the suppression of unlocked short-wavelength oscillation when the system is operated out in the 900-nm region.

The laser crystal assumed in the design is 3-cm long and is doped to absorb 80% of the pump energy. We have chosen as the design goal operation of the slave oscillator at an output of 5 mJ with a pulsewidth in the range 15-25 nsec. The pump-energy requirements depend on operating wavelength, and range from approximately 20 mJ at the short wavelengths to 60 mJ at the longest wavelength. Our only major question in the design is what value to use for the gain cross section out at 950 nm, and what would be safe operating points for both pump fluence and intracavity fluence. If we employ a 60%-R output coupler at 950 nm and the gain cross section is reduced to 1/3 of the peak value, the pump fluence at threshold for a pump-beam diameter of 1 mm would be 4.6 J/cm^2. It would be possible to operate the oscillator at $1.5x$ threshold, desirable for the generation of a 20-25-nsec-long pulse, if the laser crystal could operate reliably at a pump fluence of 7 J/cm^2. If not the laser cavity would have to be shortened and the pump ratio over threshold reduced to still maintain a short output pulse.

As far as the effectiveness of injection locking, we note that locking of similar oscillators with the output of 20-mW diode lasers has been observed[21], and thus we do not anticipate any problems in obtaining complete locking with the 4-11 W output of the master oscillator. We have calculated the temperature rise in the laser crystal due to pumping, and the worst-case pumping condition, at 950 nm, results in a transient rise in temperature of 0.2 degrees C, which would have only a small effect on the cavity resonance frequency. We have considered two techniques for maintaining a stable locked condition. Both control the piezoelectric transducer on the slave-oscillator cavity in order to maximize the resonance between the frequencies of the master- and slave-oscillator cavities. The first senses the power from the master oscillator transmitted through the slave cavity before the slave laser is pumped and adjusts the slave mirror for resonance. The other senses the delay time between the pump pulse and the slave-oscillator output. If the delay is minimized then the injected power must therefore be maximum. One could experimentally determine which of the two approaches is most effective, and then implement one of them into the overall computer control program for the system.

Ti:sapphire CRYSTAL

PZT MIRROR MOUNT

CONCAVE OUTPUT MIRROR

OUTPUT

PUMP AND
INJECTION BEAMS
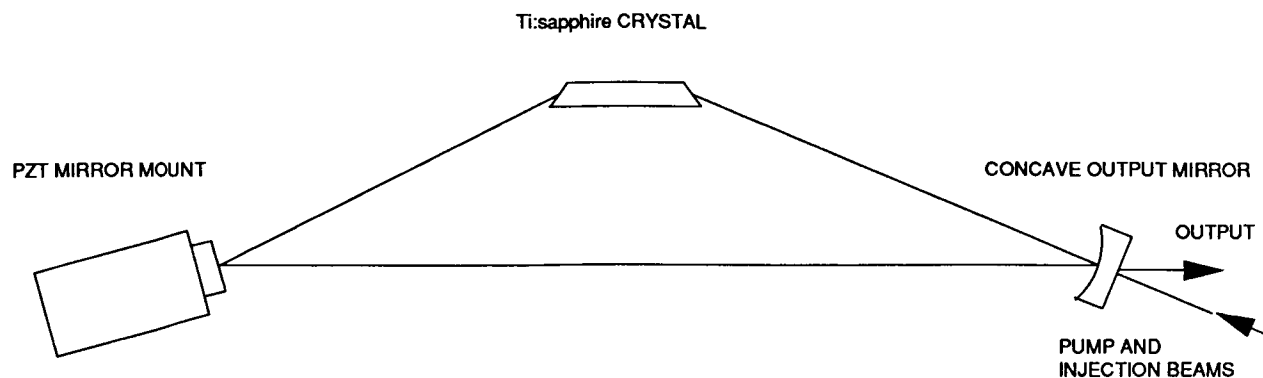
Figure 40. Ti:Al$_2$O$_3$ slave laser.

4.4.6 Faraday isolator

It is important for the overall system stability that no interaction exists between the narrow-linewidth oscillator and any following power-amplifier system. In order to minimize the interaction, we would place a Faraday isolator between the output of the slave oscillator and any amplification stages. Such a device has become available commercially from Optics for Research, Inc. (Caldwell, NJ) and utilizes the Hoya glass mentioned above as well as a permanent magnet system and two calcite polarizers. The reverse isolation is on the order of 30 dB, which should be adequate for the system. Since the Verdet constant changes with wavelength it is necessary as the wavelength changes to adjust the magnetic field integrated over the path length in the glass to obtain maximum isolation. In the suggested device the adjustment could be accomplished by a relative translation of the glass in the magnets.

5 References

1. C.E. Byvik and A.M. Buoncristiani, IEEE J. Quantum Electron. **QE-21**, 1619, (1985).

2. P. Albers, E. Stark and G. Huber, J. Opt. Soc. Am. **B3**, 134 (1986).

3. C.W. Struck and W.H. Fonger, J. Lumin. **10**, 1 (1975).

4. D. Andreou, Rev. Sci. Instrum. **49**, 596 (1978).

5. P.F. Moulton, IEEE J. Quantum Electron. **QE-21**, 1582 (1985).

6. B.F. Gachter and J.A.Konigstein, J. Chem Phys. **60**, 2003 (1974).

7. T.W. Hansch, Appl.Opt. **11**, 895 (1972).

8. M.G. Littman, Opt. Lett. **3**, 138 (1978).

9. Y.H. Meyer and M.N. Nenchev, Opt. Lett. **6**, 119 (1981).

10. D.C. Hanna, B. Luther-Davies and D.C. Smith, Electron. Lett. **8**, 369 (1972).

11. P. Brockman, C.H. Bair, J.C. Barnes, R.V. Hess and E.V. Browell, Opt. Lett. **11**, 712 (1986).

12. A. Sanchez, R.E. Fahey, A.J. Strauss and R.L Aggarwal, Opt. Lett. **11**, 363 (1986).

13. S. Lovold, P.F. Moulton, D.K. Killinger and N. Menyuk, IEEE J. Quantum Electron. **QE-21**, 202 (1985).

14. A.L. Bloom, J. Opt. Soc. Am. **64**, 447 (1974).

15. G. Holtom and O. Teschke, IEEE J. Quantum Electron. **QE-10**, 577 (1974).

16. H.G. Danielmeyer, IEEE J. Quantum Electron. **QE-6**, 101 (1970).

17. A.R. Clobes and M.J. Brienza, Appl. Phys. Lett. **21**, 265 (1972).

18. American Institute of Physics Handbook, 2nd Edition (McGraw-Hill, New York 1963) p. 6-24.

19. H.S. Carslaw and J.C. Jaeger, Conduction of Heat in Solids, 2nd Edition (Clarendon Press, Oxford, 1986) p. 205.

20. A. Koenke and A. Hirth, Opt. Commun. **34**, 245 (1980).

Spectroscopic and laser characteristics of Ti:Al$_2$O$_3$

P. F. Moulton

Schwartz Electro-Optics, Inc., 45 Winthrop Street, Concord, Massachusetts 01742

Spectroscopic measurements and laser performance of Ti:Al$_2$O$_3$ are discussed in detail. Data on absorption and fluorescence spectra and fluorescence lifetime as a function of temperature are presented. Laser characteristics observed with pulsed-dye-laser, frequency-doubled Nd:YAG-laser, and argon-ion-laser pumping are covered and show that nearly quantum-limited conversion of pump radiation can be achieved, along with tuning over the wavelength range 660–986 nm.

INTRODUCTION

The Ti:Al$_2$O$_3$ solid-state laser is one of the more recently demonstrated[1] tunable systems and the first to use Ti^{3+} as the active ion. As will be discussed below, the Ti:Al$_2$O$_3$ laser is characterized by a simple energy-level structure, a broad tuning range, and a relatively large gain cross section. This paper will cover basic spectroscopy of Ti:Al$_2$O$_3$ and properties of laser operation under both pulsed and quasi-cw excitation.

SPECTROSCOPY

The electronic structure of the Ti^{3+} ion is a closed shell plus a single 3d electron. The free-space, fivefold-degenerate (neglecting spin) d-electron levels are split by the crystal field of the host. In the host Al$_2$O$_3$ the site for the Ti^{3+} ion has trigonal symmetry; the crystal field can be viewed as the sum of cubic- and trigonal-symmetry components. The cubic field dominates and splits the Ti^{3+} energy levels into a triply degenerate $^2T_2$ ground state and a doubly degenerate ^2E excited state. The trigonal field splits the ground $^2T_2$ state into two levels, and the lower of the two levels is split further into two levels by the spin–orbit interaction.[2] The energy differences between the lowest-energy $^2T_2$ level and the other $^2T_2$ levels have been determined by infrared absorption measurements[2,3] to be 38 and 107 cm^{-1}; the dynamic Jahn–Teller effect has been shown to play a major role in determining those energies.[4]

The separation between the $^2T_2$ and ^2E states was first determined by McClure[5] through optical absorption measurements to be around 19 000 cm^{-1}, as evidenced by an absorption band in the visible wavelength region. Later measurements[6,7] confirmed that the band observed was, in fact, due to the Ti^{3+} ion. Figure 1 shows our measurement, for two polarizations at room temperature, of the $^2T_2 \rightarrow {}^2E$ absorption band. The double-peaked nature of the band is due to the Jahn–Teller splitting of the ^2E state. McClure[5] measured the peak splitting to be 1850 cm^{-1} at a crystal temperature of 77 K, and Eigenmann[8] later showed that two Gaussian bands with centers of 20 476 and 17 987 cm^{-1} and linewidths of 1295 and 921 cm^{-1}, respectively, were good approximations to the 77-K band shape. The cross-section scale shown in Fig. 1 was derived from measurements on a sample with a Ti concentration of 3.3 × 10^{19} cm^{-3} (or ~0.1

wt. % Ti$_2$O$_3$ in Al$_2$O$_3$) as determined by x-ray fluorescence techniques. All concentrations discussed in this paper refer to those in the crystal, based on the cross-section data. Since the x-ray measurement does not discriminate between different valence states of the Ti ion, it may be that not all the ions were Ti^{3+}, and thus the cross section represents a lower bound.

Data on fluorescence from the $^2E \rightarrow {}^2T_2$ transition of Ti:Al$_2$O$_3$ was first reported by Gachter and Koningstein,[9] who associated a number of low-temperature details in the spectra with zero-, one- and two-phonon transitions. In particular, they established that the highest-energy zero-phonon line was at 16 216 cm^{-1}. Our measurements of the polarized fluorescence spectra at 300 K (Fig. 2) show emission peaking at and extending to longer wavelengths than that in Ref. 9; our results[10] agree with the behavior of the Ti:Al$_2$O$_3$ laser systems discussed below.

We observed the fluorescence decay at room temperature to be exponential, with a lifetime of 3.15 ± 0.05 μsec. The lifetime measurement was accomplished by recording (on a transient digitizer) the detected broadband fluorescence decay from samples excited at 490 nm by a pulsed dye laser. Six different samples grown by three different techniques and having concentrations ranging from <0.01 to 0.1 wt. % Ti$_2$O$_3$ were examined and showed the same decay time within the error limits given. Figure 3 plots the variation in lifetime with temperature for one sample doped at the 0.1% level. Some of the reduction in lifetime with increasing temperature could be associated with an increased phonon-induced radiative transition rate, but the rapid reduction in lifetime at high temperatures is characteristic of fluorescence quenching due to multiphonon nonradiative decay.[11]

The only other short-wavelength absorption associated with the Ti^{3+} ion in Al$_2$O$_3$ is a charge-transfer band, produced by the transition in which an electron on one of the oxygen ions moves to the Ti-ion site, changing the ion state to Ti^{2+}. Tippins[12] measured charge-transfer bands for a number of transition-metal ions in Al$_2$O$_3$ and reported the existence of the Ti^{3+} charge-transfer band peaking around 180 nm. Our measurements, done on a 0.1-mm-thick sample containing ~0.05 wt. % Ti$_2$O$_3$, show almost exactly the same spectral shape observed by Tippins up to the short-wavelength limit (190 nm) of the spectrophotometer used and include evidence of the small peak at 260 nm attributed by Tippins to Fe^{3+} impurities. However, the extinction
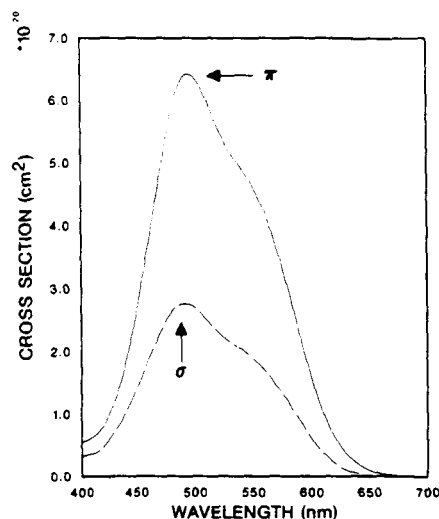
Fig. 1.   Polarized absorption cross sections for the $^2T_2 \rightarrow {}^2E$ transition in Ti:Al$_2$O$_3$. Baseline was arbitrarily set to zero for both polarizations at 700 nm.
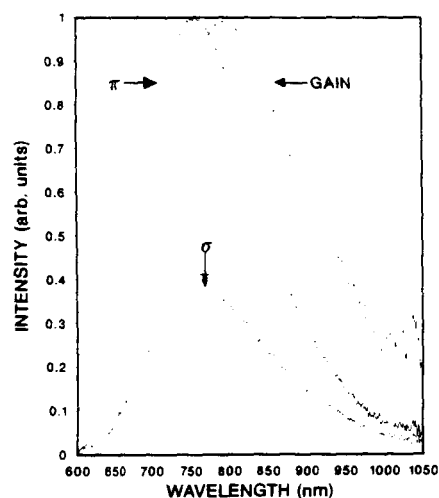

Fig. 2.   Polarized fluorescence spectra and calculated gain line shape for Ti:Al$_2$O$_3$.

coefficient of our measured absorption, 27 cm^{-1} at 190 nm, is considerably less than the value of ~180 cm^{-1} deduced from Tippins data, which is surprising, since the crystal examined by Tippins had an estimated doping level smaller than our sample by more than an order of magnitude. Tippins noted that an *a priori* calculation of the charge-transfer band positions in Al$_2$O$_3$ for four ions other than Ti^{3+} gave good agreement with data, while the band observed in the Ti^{3+}-doped sample was 1 eV lower in energy than predicted. It was also noted that the Ti^{3+} band, because of the closeness of ionization potentials between Ti^{2+} and Al^{2+}, might be close to the intrinsic absorption edge of Al$_2$O$_3$ and therefore difficult to observe. We conclude from our measurements that the measured high-energy absorption in the Ti:Al$_2$O$_3$ samples may not be associated with Ti^{3+} ions substituting in the Al^{3+} sites and may, in fact, be associated with some other defect.

Nath and Walda[13] reported that the addition of trace amounts of TiO$_2$ (<100 parts in 10^6) had a substantial effect on the UV absorption edge of Al$_2$O$_3$, suggesting that the Ti^{4+} ion could be responsible for the observed UV absorption. Later experiments by Bessonova *et al.*[14] showed that Ti-doped samples having both the $^2T_2 \rightarrow {}^2E$ and the 190-nm absorption bands would exhibit both an appreciable increase in the intensity of the UV band and a disappearance of the $^2T_2 \rightarrow {}^2E$ band after annealing in oxygen at high temperatures. The authors concluded that Ti^{4+} ions were therefore responsible for the 190-nm band.

All the Ti:Al$_2$O$_3$ crystals used for laser experiments exhibited an unexpectedly high loss at the laser wavelength. An investigation of the loss showed the existence of a broad, weak absorption band extending into the near infrared. Figure 4 plots the band for two polarizations at room temperature, observed from a Czochralski-grown crystal[15] doped (as determined by optical absorption measurements)
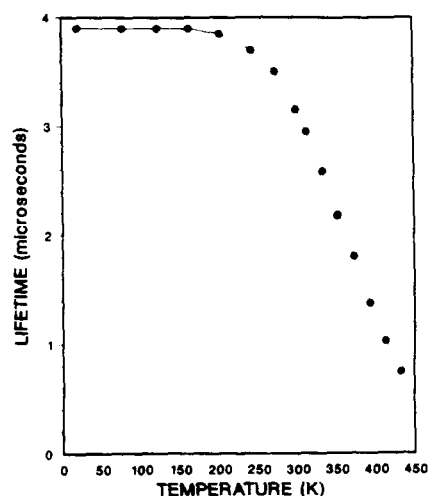

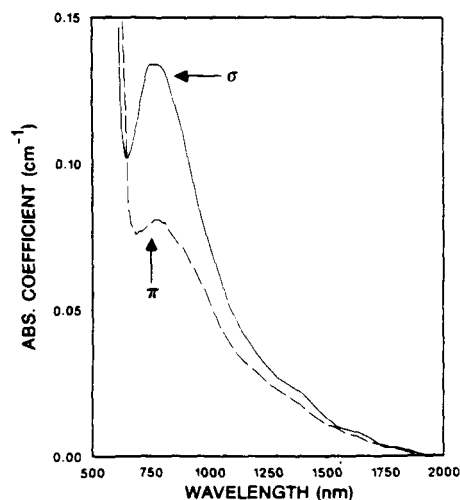Fig. 3.   Fluorescence lifetime versus temperature for the $^2E \rightarrow {}^2T_2$ transition in Ti:Al$_2$O$_3$.

Fig. 4.   Polarized measurement of the infrared absorption band in Ti:Al$_2$O$_3$.

with ~0.08 wt. % Ti_2O_3. Note that in contrast to the Ti^{3+} absorption band in Fig. 1, the σ polarization is more intense than the π polarization. The intensity of the near-infrared absorption band was found to vary among samples having roughly the same Ti^{3+} doping level and decreased as the Ti^{3+} concentration decreased. From the limited number of samples examined we observed that material grown by the heat-exchanger method[16] had a lower level of absorption than Czochralski-grown crystals. The identification and elimination of the defect or defects responsible for the absorption band is currently an active research area. Two theories of the origin of the infrared absorption band have been proposed. One[17] associates the absorption with Ti^{3+} ions in interstitial or defect sites or at sites close to native defects. There is some evidence that postgrowth annealing can reduce the infrared band intensity.[17] The other[18] proposes that pairs of Ti^{3+}–Ti^{4+} ions are responsible, based on observations of pair-related absorption in solutions.[19]

GAIN MEASUREMENTS

Optical gain in $Ti:Al_2O_3$ was measured by collinear propagation of focused, TEM_{00}-mode pump and probe beams through a 0.9-cm-long crystal doped with ~0.1 wt. % Ti_2O_3. The π-polarized probe beam was from a krypton-ion laser operating at 676.5 nm, while the pump beam was the 514.5-nm output of an argon-ion laser. The gain cross section at the probe-beam wavelength, σ_{pr}, was estimated by use of the following expression:

$$\sigma_{pr} = \frac{\pi(b^2 + 1)hcw_{pu}^2 G}{2\lambda_{pu} P_{pu} \tau} [1 - \exp(-\alpha_{pu}l)]^{-1}, \qquad (1)$$

where τ is the fluorescence lifetime, G is the measured fractional gain in the probe beam, α_{pu} is the absorption coefficient for the pump beam, l is the crystal length, λ_{pu} is the pump wavelength, and P_{pu} is the pump power in the crystal at the entrance surface. The quantity b is the ratio of the probe beam radius to that, w_{pu}, of the pump beam, while h and c are Planck's constant and the speed of light, respectively. For the experiment considered b was approximately 0.5, w_{pu} was 6×10^{-3} cm, and α_{pu} was 2.7 cm^{-1}. A gain of 1×10^{-2} per watt of pump power was observed, leading to a calculated σ_{pr} of $\sim 6.8 \times 10^{-20}$ cm^2. Given the uncertainties in some of the measured quantities, especially the values for G and w_{pu}, the accuracy of σ_{pr} as determined by Eq. (1) is estimated to be ±30%.

Figure 2 includes a curve for the gain cross-section line shape calculated using the relation between fluorescence and cross-section line shapes discussed in Appendix A. The broadening and extension to longer wavelengths of the gain line shape compared with the fluorescence line shape is especially noticeable for the large-linewidth $Ti:Al_2O_3$ system. From the curve in Fig. 2 one predicts that the peak gain cross section is approximately four times the quantity σ_{pr}, and thus, based on the gain measurements, the peak gain cross section is $\sim 2.7 \times 10^{-19}$ cm^2.

The relation between spontaneous lifetime and gain cross section for uniaxial crystals, discussed in Appendix A, can be used to obtain an independent estimate of the peak gain cross section. The line shapes for π- and σ-polarized emission in Fig. 2 were numerically integrated, following Eq. (A9) in Appendix A, and used with Eq. (A8) to find a peak 300-K

gain cross section, at 795 nm, of $\sim 4.8 \times 10^{-19}$ cm^2, assuming a radiative lifetime of 3.15 μsec. If the radiative lifetime is really (from Fig. 3) the low-temperature value of 3.87 μsec, then the room-temperature fluorescence quantum efficiency is 0.81 and the peak gain cross section is 3.9×10^{-19} cm^2. The discrepancy in cross sections between the pump-probe measurement and the derivation from lifetime could be resolved by assuming a lower value for the room-temperature quantum efficiency.

A test of the data on emission cross sections can be performed by comparing the integrated cross section for emission with that for absorption. The validity of the test relies on the use of the Condon approximation in treating the coupled system composed of the Ti^{3+} electron and the host crystal phonons. In that approximation, the electric-dipole matrix element between two levels of the coupled system is expressed as the product of an electric-dipole matrix element between the purely electronic part of the system wave function and an overlap integral between the initial and final phonon states. The dipole matrix element is assumed independent of the particular phonon states involved. Thus the oscillator strengths for absorption and emission are equal, when degeneracies are properly accounted for. Using the oscillator-strength formula given in Appendix A we calculated for absorption an oscillator strength of 1.94×10^{-4}, based on the data in Fig. 1 and on degeneracies of 3 and 2 in the initial and final states, respectively. In the calculation of the emission oscillator strength we assume that the emission is effectively from only one of the ^2E states, and thus the initial- and final-state degeneracies are 1 and 3, respectively. In that case the emission oscillator strength will equal that for absorption if the peak cross section is 4.3×10^{-19} cm^2, in reasonable agreement with the values derived in the measurements above. If the Condon approximation holds we would conclude that the fluorescence quantum efficiency for $Ti:Al_2O_3$ is close to unity.

PULSED-LASER OPERATION

Dye-Laser Pumping

Laser operation from $Ti:Al_2O_3$ was first observed by longitudinally pumping the same crystal used in gain measurements with the 503-nm output of a coaxial flash-lamp-pumped Coumarin 504 dye laser. The 26-cm-long $Ti:Al_2O_3$-laser cavity consisted of an 8%-transmission flat mirror and a 15%-transmission, 75-cm-radius concave mirror. Figures 5(a), 5(b), and 5(c) show the pulse shapes of the pump laser and the $Ti:Al_2O_3$ laser at two pump levels over threshold; relaxation oscillations in the $Ti:Al_2O_3$ laser are evident. The uncoated crystal used was of poor optical quality, exhibiting considerable scattering and optical distortion, and an output energy of only 1 mJ could be observed at a pump energy of 36 mJ. The laser output wavelength was in the region 750–760 nm. As Fig. 2 indicates, one would have expected operation at a somewhat longer wavelength from the position of the peak in the gain cross section. The wavelength variation of absorption in the crystal around the laser operating region (an example for one crystal appears in Fig. 4) may have shifted the net gain to shorter wavelengths, however.

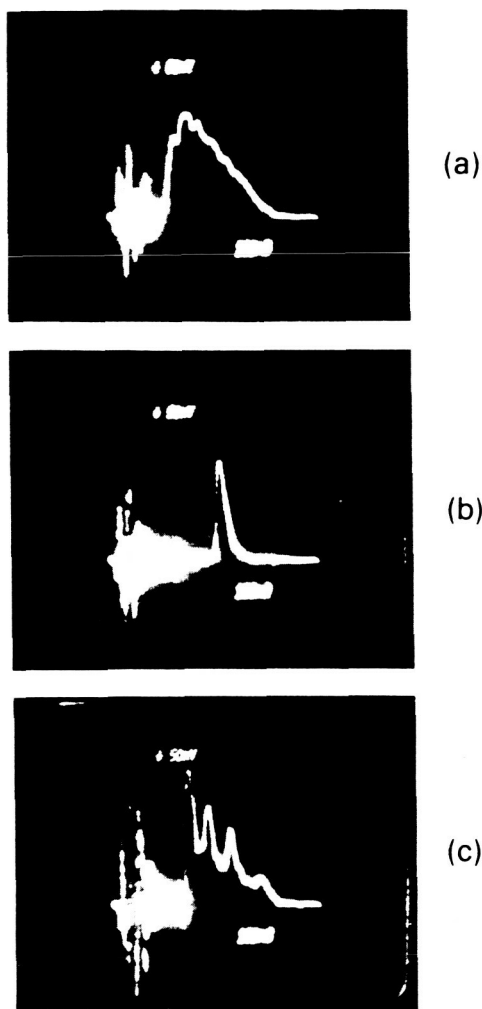Higher-quality crystals were obtained subsequent to the

Solid-State Laser Materials

Fig. 5.   Pump pulse shape (a) and Ti:Al₂O₃ laser pulses at (b) 1.6-times threshold and (c) 3.6-times threshold. Time scale is 100 nsec per large division. Signals at left of traces are electrical noise.

initial laser demonstration. Two laser rods were fabricated from the crystals; both were polished with flat, parallel end faces and antireflection coated for 750 nm. One crystal (referred to as heavily doped) was 2.1 cm long and had a Ti^{3+} doping level of 0.1%, while the other crystal (referred to as lightly doped) was 3.2 cm in length and had a doping level of 0.02%. The measured absorption coefficients at 750 nm for π-polarized light were ~0.04 and ~0.006 cm^{-1} for the heavily and lightly doped crystals, respectively.

Absorption from the $^2T_2 \rightarrow {}^2E$ transition in the heavily doped crystal was sufficiently intense to permit longitudinal pumping by the same coaxial flash-lamp-pumped dye laser used in the initial experiments, operating more efficiently with R6G dye at ~587 nm. Figure 6 shows the output energy at ~750 nm from the heavily doped crystal versus absorbed 587-nm pump energy for two different output-mirror transmissions. The optical cavity comprises a highly reflecting 25-cm-radius concave mirror and a flat output mirror, spaced 15 cm apart. Analysis of the data in Fig. 6

indicates that the slope quantum efficiency obtained with the 37%-transmission mirror was 67%. The internal loss in the laser can be calculated by two techniques, one based on the ratio of the thresholds for the two output mirrors (2.3) and the other based on the ratio of slope efficiencies (2.7). If L is the internal loss, T_1 and T_2 are two different output-mirror transmissions, R_{TH} is ratio of the threshold observed with T_2 to that with T_1, and R_Δ is the ratio of the slope efficiency observed with T_2 to that with T_1, then

$$L = (T_2 - R_1 T_{TH})/(R_{TH} - 1) \qquad (2)$$

and

$$L = (R_\Delta - 1)T_1 T_2/(T_2 - R_\Delta T_1). \qquad (3)$$

The assumptions for these equations are that the threshold and slope efficiency are proportional to $L + T_i$ and $T_i/(T_i + L)$, respectively, where $i = 1$ or 2. We found the same value for L (18%) using both techniques; the value was in good agreement with the measured absorption coefficient of the laser crystal.

Tuning experiments on the dye-laser-pumped system were carried out by insertion of two Brewster-angle, fused-silica prisms into the laser cavity. (Experiments with a Littrow-mounted grating as the tuning element proved to be unreliable because of optical damage to the grating surface.) The cavity length was extended to ~25 cm with the addition of the prisms, and the flat output mirror was replaced with another 25-cm-radius mirror. With a set of mirrors coated for operation at 750 nm, with 6% output coupling at that wavelength, laser operation over the wavelength range 687–821 nm was observed at an absorbed pump energy of ~8 mJ. When the mirror set was changed to one coated for 850 nm, with 5% coupling, tuning from 726 to 986 nm was possible at the same pumping level. The short-wavelength tuning limit was extended to 660 nm by the use of a set of 632.8-nm He–Ne laser mirrors in the cavity along with the lightly doped laser crystal pumped at 503 nm.

Although laser operation was readily obtained by use of the dye-laser pump, the low repetition rate (1 Hz) of the
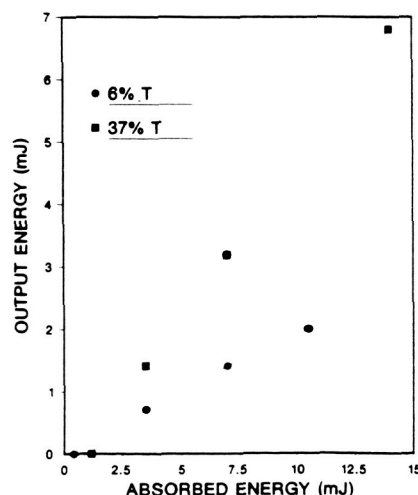

Fig. 6.   Output energy versus absorbed pump energy with two different output-mirror transmissions for dye-laser-pumped Ti:Al₂O₃ laser.
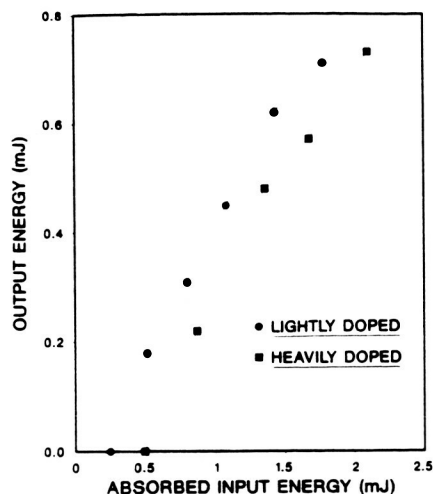
Fig. 7. Output energy versus absorbed input energy for two different laser crystals, pumped by a frequency-doubled Nd:YAG laser.

pump and the fluctuations in output energy and mode properties from one pulse to the next made characterization of some properties of the Ti:Al$_2$O$_3$ laser difficult. Additional data, described in the following subsection, were taken on 532-nm, frequency-doubled Nd:YAG-laser-pumped systems.

Doubled Nd:YAG-Laser Pump

As for the case of dye-laser pumping, longitudinal excitation of the crystal (through one of the Ti:Al$_2$O$_3$ laser-cavity mirrors) was used in the experiments. At 532 nm the lightly and heavily doped crystals absorbed ~70 and ~96% of the incident pump energy, respectively.

The initial pump system used was a conventional stable-resonator, multimode, flash-lamp-pumped and Q-switched Nd:YAG laser, the output of which was externally doubled by a KD*P crystal. The system produced 532-nm energies of up to 5.5 mJ at a 10-Hz repetition rate. Figure 7 shows output versus absorbed pump energy for the two crystals in a 17-cm-long optical cavity composed of a 25-cm-radius highly reflecting mirror and a flat output mirror. The output mirror transmissions at 750 nm were 25 and 49% for the lightly and heavily doped crystals, respectively. The slope quantum efficiency was 68% over most of the operating range of the lightly doped crystal and 78% over the initial portion of the range for the heavily doped crystal, and operating wavelengths were in the 750–760-nm region. Heating effects were evident in the latter material at the highest input energies, manifested in a change in the mode structure of the Ti:Al$_2$O$_3$ laser output, from TEm$_{00}$-mode operation at low input energies to highly multimode operation at the highest energies. Near-diffraction-limited output could be obtained at high energies, however, by a defocusing of the pump beam.

We took data on laser threshold and slope efficiency for both crystals using other output-mirror transmissions. As for the case with the dye-laser pump, the loss associated with the heavily doped crystal was found to be in reasonable agreement with the measured value of 0.04 cm^{-1}. A consistent loss value was not determined for the lightly doped

crystal. In particular, the slope efficiency calculated from the data of Fig. 7 would be associated with a loss coefficient of 0.018 cm^{-1}. On the other hand, a threshold comparison between operation with 1 and 6% output couplings indicated a coefficient of 0.008 cm^{-1}, in close agreement with the measured absorption coefficient. The high loss derived from the slope efficiency could be related to an incomplete spatial overlap between the pump beam and the Ti:Al$_2$O$_3$ cavity modes in the crystal owing to the divergence of the focused pump away from the focal point. Such an incomplete overlap would reduce laser efficiency and make the crystal losses appear to be higher than they actually were. Overlap effects are less of an issue with the heavily doped crystal because of the short (~0.5 cm to the 1/e point) penetration depth of the pump radiation.

As part of the laser characterization, measurements of the pump-beam size at the crystal face were attempted by measuring pump transmission through a variety of calibrated apertures. Accurate results were difficult to obtain because the Q-switched pulse tended to ablate the aperture material, and if the beam intensity was attenuated to avoid ablation the transmitted power levels were difficult to measure. However, it was determined that 50- and 200-μm apertures passed ~40 and 90% of the pump energy, respectively. As was the case for dye-laser pumping, intracavity prisms were used to tune the output of the doubled-Nd:YAG-pumped laser. The same combinations of crystals and mirrors permitted tuning to be observed over the range 662–950 nm.

The temporal outputs of the Ti:Al$_2$O$_3$ lasers were observed to consist of single pulses, characteristic of gain-switched operation resulting from a pump pulse width that was short compared with the upper-state lifetime of the pumped laser. The pump pulse width was ~20 nsec full width at half-maximum (FWHM). The resulting Ti:Al$_2$O$_3$ laser pulse widths ranged, with the laser systems characterized by Fig. 7, from 11 nsec FWHM for the lightly doped crystal pumped at ~2.5 times threshold to the 5-nsec pulse shown in Fig. 8, observed from the heavily doped crystal pumped at ~5.5 times threshold. The delay between the peak of the pump pulse and the peak of the Ti:Al$_2$O$_3$ laser pulse varied, as
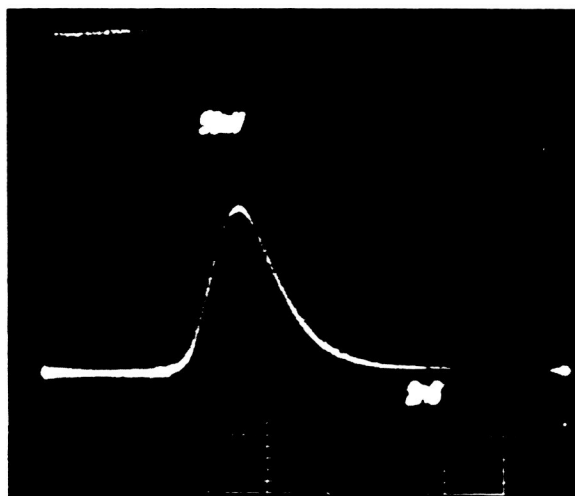

Fig. 8. Output pulse from a frequency-doubled Nd:YAG-pumped Ti:Al$_2$O$_3$ laser. Time scale is 4 nsec per large division.
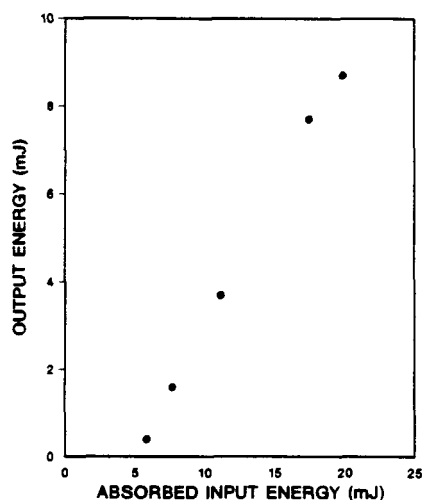
Fig. 9.   Output energy versus absorbed input energy for a Ti:Al₂O₃ laser pumped by an unstable-resonator, frequency-doubled Nd:YAG laser.

expected, with the pump ratio, from 45 nsec at 2.5 times threshold to 15 nsec at 6 times threshold.   Computer models based on the standard rate-equation approach to laser dynamics (e.g., Ref. 20) confirmed that only a single pulse should be generated given the pump and Ti:Al₂O₃ laser-cavity characteristics and that the buildup times and pulse widths observed experimentally were reasonable.   For the particular data of Fig. 8 the computer-generated pulse width was 1 nsec instead of the observed 5.   Some of this difference is due to the ~1 nsec rise time of the detector–oscilloscope combination (a vacuum photodiode driving a Tektronix 7834 oscilloscope).   The major cause of the discrepancy is likely the limitations of the rate-equation approach, the assumptions of which become invalid when the cavity round-trip time (1 nsec in this case) is an appreciable fraction of the predicted laser pulse width.

Considerably higher pump energies were obtained by employing an unstable-resonantor configuration with the Nd:YAG pump laser; pulse energies at 532 nm of up to 45 mJ at a 10-Hz repetition rate were generated.   Figure 9 presents output energy versus absorbed input energy for a Ti:Al₂O₃ laser assembled using the lightly doped crystal in a 60-cm-long resonator, which was composed of a flat, 750-nm highly reflecting mirror and a 2-m-radius, 30%-transmitting output mirror.   The laser crystal was located ~10 cm from the output mirror and pumped through the flat mirror.   This particular arrangement was employed to minimize optical damage to the coating on the flat.   The pump-beam diameter at the crystal was estimated to be ~1 mm.

The slope quantum efficiency in Fig. 9 is 86%.   The actual pump energy available from the doubling crystal was 1.9 times greater than the absorbed energy owing to the incomplete absorption of the pump in the crystal and reflection losses in the system optics; the overall conversion efficiency from available pump energy to Ti:Al₂O₃ output energy was 23%.   As for the stable-resonator pump, the Ti:Al₂O₃ output consisted of a single pulse, and at the maximum energy shown in Fig. 9 the output pulse width was 38 nsec.   Computer calculations predicted a pulse width of 20 nsec.   In

addition to shortcomings in the theory, discussed above, an additional reason for the longer observed pulse width may have been the multi-transverse-mode nature of the Ti:Al₂O₃ laser output.   Unlike the previous Ti:Al₂O₃ lasers, the unstable-resonator-pumped system had an excited volume in the Ti:Al₂O₃ crystal large enough to permit several transverse modes to oscillate.   The existence of slightly different buildup times for the different modes has the effect of spreading out in time the gain-switched output pulse.

The limit to the output energy for the unstable-resonator-laser-pumped system was set by pump-induced optical damage to the flat cavity mirror; damage occurred at energies slightly higher than shown in Fig. 9.   It is advisable in development of higher-energy Ti:Al₂O₃ lasers pumped by Q-switched, frequency-doubled Nd:YAG lasers to use pumping techniques that avoid passing the pump beam through one of the cavity mirrors.

Argon-Ion-Laser Pumping

Quasi-cw operation was obtained from the Ti:Al₂O₃ laser by use of an argon-ion laser as a pump source.   The argon-ion laser, operating on all lines in the blue-green wavelength region, was focused by a 17-cm-focal-length lens through a 25-cm-radius mirror (having 100% reflectivity at 750 nm) into the lightly doped Ti:Al₂O₃ crystal.   The laser cavity was completed by another 25-cm-radius mirror having ~1% transmission at 750 nm, spaced 30 cm from the highly reflecting mirror.   The laser crystal, in the center of the cavity, was attached to a copper heat sink and placed in a vacuum, along with the two cavity mirrors, to allow operation either with the crystal at room temperature or with the heat sink cooled to ~80 K by liquid nitrogen.   Under the latter conditions operation was obtained at a pump power (peak) of 4.8 W incident on the laser crystal.   Heating effects were evident in the sensitivity of optimum mirror alignment to pump power above threshold and were reduced by mechanically chopping the pump beam such that the pump was on only 16% of the time.   With the liquid-nitrogen cooling a peak output power from the Ti:Al₂O₃ laser of 150 mW was obtained at an incident pump power of 7.4 W.   Laser output was in the TEM₀₀ mode.   The slope quantum efficiency was ~11% based on a measured absorbed/incident pump-power ratio of 0.73.   Quasi-cw operation was also observed with the crystal at room temperature, with a threshold incident peak pump power of 5.6 W.   Heating effects were much more evident at room temperature because of the lower thermal conductivity of Al₂O₃ compared with that at liquid-nitrogen temperatures.   Fluctuations in the output power on a 200-μsec time scale were evident during a 1.6-msec-long pump pulse, and a peak power output of only ~45 mW could be obtained at a pump level of ~7 W.   Some effects on laser operation of the reduction in upper-state lifetime with temperature, evident in Fig. 3, were likely for the room-temperature Ti:Al₂O₃ laser.

A theory developed for longitudinally pumped lasers[20] operating in the TEM₀₀ mode and pumped by a TEM₀₀-mode laser is appropriate for the system discussed above. The threshold pump power, P_{TH}, is given by the expression

$$P_{TH} = \frac{\pi E_p w_L^2 (L + T) (a^2 + 1)}{4\sigma\tau [1 - \exp(-\alpha l)]},$$ (4)

where E_p is the energy of a pump photon, w_L is the beam

radius of the laser cavity mode in the crystal, L is the laser internal loss, T is the output-mirror transmission, a is the ratio w_p/w_L, where w_p is the beam radius of the pump, σ is the peak gain cross section, τ is the upper-state lifetime, and αl is the product of the absorption coefficient for the pump and the crystal length. The appropriate values for the cw-pumping experiment were $w_L = 1.7 \times 10^{-2}$ cm, $w_p = 4 \times 10^{-3}$ cm, $E_p \approx 4 \times 10^{-19}$ J, and $1 - \exp(-\alpha l) = 0.73$. The value used for $L + T$ was 0.05, and the lifetime was 3.87 μsec at 77 K and 3.15 μsec at room temperature. The observed thresholds for liquid nitrogen and room temperature were consistent with gain cross sections of 3.6×10^{-19} and 3.8×10^{-19} cm^2, respectively. Thus we find good agreement between the cross section calculated using the lifetime and fluorescence spectra and the cross section deduced from the cw-laser threshold. The slope efficiency was predicted to be 20% compared with the 11% observed, and there is, as yet, no good explanation for this discrepancy. In one experiment the transmission of pump power through the crystal at room temperature was measured as a function of incident power up to the 6-W level, in an effort to detect any unexpected saturation effects. The transmission was observed to be invariant, however.

CONCLUSIONS

The laser performance of Ti:Al$_2$O$_3$ is reasonably well understood based on the fundamental spectroscopic properties of the crystal. Laser operation spanning the entire expected gain linewidth and efficient, nearly quantum-limited conversion of pump energy have been observed. Such behavior is possible because the simple energy-level structure of the Ti^{3+} ion does not permit excited-state absorption of either the pump or Ti:Al$_2$O$_3$ laser radiation, provided that any charge-transfer transitions are sufficiently high in energy; this condition appears to be meet in Ti:Al$_2$O$_3$. The short upper-state lifetime is anomalous for paramagnetic-ion systems based on parity-forbidden transitions and is the result of the strong trigonal field in the Al$_2$O$_3$ host, which causes a significant deviation from an inversion-symmetry environment for the Ti^{3+} ion. Fortunately, the short lifetime is accompanied by a relatively large (especially for tunable systems) peak gain cross section. Three independent techniques for determining the cross section yield values in the range $(3-4) \times 10^{-19}$ cm^2. The most significant improvement in the quality of existing Ti:Al$_2$O$_3$ crystals would be a reduction in the as-yet-unidentified absorption in the laser wavelength region, an absorption not associated with isolated Ti^{3+} ions. It is likely that laser operation from Ti^{3+} in other host crystals can be obtained, and the search for new hosts should be an interesting challenge for both materials scientists and laser physicists.

APPENDIX A

McCumber[21] defines a spontaneous emission function $f_\varsigma(\mathbf{k}, \nu)$ such that $f_\varsigma(\mathbf{k}, \nu)d\Omega_{\mathbf{k}\varsigma}$ is the average intensity in photons/second for one of the two possible independent polarizations, per unit frequency interval of frequency ν radiation emitted in the direction of the unit vector $\mathbf{k}$ into the solid angle $d\Omega_{\mathbf{k}\varsigma}$, from each excited fluorescent center. We have changed his notation to use ς as an index for one of the

polarizations and also use frequency ν instead of angular frequency ω. The gain cross section $\sigma_\varsigma(\mathbf{k}, \nu)$ is related to the spontaneous emission function by[21]

$$\sigma_\varsigma(\mathbf{k}, \nu) = f_\varsigma(\mathbf{k}, \nu)c^2/n^2\nu^2, \tag{A1}$$

where n is the refractive index of the host crystal, approximated in this discussion as isotropic. We can define another spontaneous emission function, $G_\varsigma(\mathbf{k}, \lambda)$, which is similar to $f_\varsigma(\mathbf{k}, \nu)$ but gives emission intensity in terms of more experimentally useful units, watts per unit wavelength interval, as a function of free-space wavelength $\lambda = c/\nu$. A straightforward calculation, accounting for the change in variables, allows the gain cross section as a function of wavelength to be expressed by

$$\sigma_\varsigma(\mathbf{k}, \lambda) = \frac{\lambda^5 G_\varsigma(\mathbf{k}, \lambda)}{hc^2 n^2}. \tag{A2}$$

This relation was used to calculate the gain cross-section line shape shown in Fig. 2.

For a uniaxial crystal such as Ti:Al$_2$O$_3$ it is possible to derive the directional and polarization variation in spontaneous-emission intensity. We establish a spherical coordinate system for the direction of emission based on the angle θ between $\mathbf{k}$ and the c axis and the angle ϕ between the projection of $\mathbf{k}$ on a plane perpendicular to the c axis and some arbitrary axis in that plane. The orientation of the polarization (transverse to $\mathbf{k}$) is measured by the angle ψ. For $\psi = 0$ the polarization lies in the plane perpendicular to the c axis, the σ polarization. After some geometrical calculations one finds that the spontaneous-emission function can be expressed as

$$G(\lambda, \theta, \phi, \psi) = G_\sigma(\lambda)(\cos^2 \psi + \sin^2 \psi \cos^2 \theta)$$
$$+ G_\pi(\lambda)\sin^2 \psi \sin^2 \theta, \tag{A3}$$

where $G_\sigma(\lambda)$ and $G_{\pi(\lambda)}$ are emission functions for purely σ- and π-polarized radiation, respectively. As expected, there is no variation in the function with ϕ.

McCumber relates the spontaneous emission lifetime, τ, to the emission function $f_\varsigma(\mathbf{k}, \nu)$ by the following:

$$1/\tau = \sum_\varsigma \int_{4\pi} d\Omega_{\mathbf{k}\varsigma} \int_0^\infty f_\varsigma(\mathbf{k}, \nu)d\nu, \tag{A4}$$

where the summation is to be made over two independent (i.e., orthogonal) polarizations. The lifetime can be related to the $G(\lambda, \theta, \phi, \psi)$ function by

$$1/\tau = \frac{1}{hc} \int_\infty^0 d\lambda \int_0^{2\pi} d\phi \int_0^\pi d\theta\lambda \sin\theta[G_\sigma(\lambda)(1 + \cos^2\theta)$$
$$+ G_\pi(\lambda)\sin^2\theta], \tag{A5}$$

where the sum has been taken over two linear polarizations, one with $\psi = 0$ and the other with $\psi = \pi/2$. After carrying out the integrations over angle we are left with

$$1/\tau = \frac{8\pi}{hc} \int_\infty^0 [\tfrac{2}{3}G_\sigma(\lambda) + \tfrac{1}{3}G_\pi(\lambda)]d\lambda. \tag{A6}$$

It is possible given knowledge of the emission functions $G_\sigma(\lambda)$ and $G_\pi(\lambda)$ and the lifetime to determine the gain cross section. Experimental measurements of the functions typi-

cally determine them to within some multiplicative constant.

We define the experimentally measured functions

$$g_\pi(\lambda) = \alpha G_\pi(\lambda),$$
$$g_\pi(\lambda) = \alpha G_\pi(\lambda), \tag{A7}$$

where α is a constant. By use of Eqs. (A2) and (A6) one can find the cross section in terms of the angular variables discussed above. such that

$$\sigma(\theta, \psi, \lambda)$$
$$= \frac{\lambda^5 \left[g_\pi(\lambda)\sin^2\psi \sin^2\theta + g_\sigma(\lambda)(\cos^2\psi + \sin^2\psi \cos^2\theta) \right]}{8\pi c n^2 \tau I}, \tag{A8}$$

where

$$I = \int_\infty^0 [{}^2\!/_3\, g_\sigma(\lambda) + 1/3\, g_\pi(\lambda)]\lambda d\lambda. \tag{A9}$$

If the measured spontaneous-emission lifetime results from a combination of radiative and nonradiative decay, then one can define a fluorescence quantum efficiency. η, as the ratio of the radiative rate to the total rate, where the total rate is the inverse of the measured lifetime. The cross section calculated in Eq. (A8) must be multiplied by η to derive the actual gain cross section.

Another important spectroscopic quantity is the oscillator strength of a transition. If F_{if} is the oscillator strength for a transition from initial level i to final level f, then, for a uniaxial crystal (in CGS units)

$$F_{if} = \frac{g_i}{g_f} \frac{mc^2}{\pi e^2} \frac{9n}{(n^2+2)^2} \int_\infty^0 [{}^2\!/_3\, \sigma_\sigma(\lambda) + {}^1\!/_3\sigma_\pi(\lambda)] \frac{d\lambda}{\lambda^2}, \tag{A10}$$

where m and e are the mass and charge of the electron, respectively, and g_i and g_f are the degeneracies of the initial and final levels, respectively. $\sigma_\sigma(\lambda)$ and $\sigma_\pi(\lambda)$ are the cross sections for σ- and π-polarized emission, respectively. The derivation of the equation is based on the averaging techniques for uniaxial crystals discussed above and on the use of the Lorentz–Lorenz correction for the local field in the crystal, as discussed by Curie.[22]

ACKNOWLEDGMENTS

REFERENCES

1. Operation of the Ti:Al2O3 laser was first reported by the author at the Twelfth International Quantum Electronics Conference in Munich in June 1982. Brief articles appeared in *Physics News in 1982*," P. F. Schewe, ed. (American Institute of Physics, New York, 1983) and in *Solid State Research Report* (Lincoln Laboratory, MIT, 1982:3), pp. 15–21. A more complete description of the author's efforts was in the chapter "Recent advances in transition-metal-doped lasers," in *Tunable Solid State Lasers*, Springer Series in Optical Sciences, P. Hammerling, A. Budgor, and A. Pinto, eds. (Springer-Verlag, Berlin, 1985). pp. 4–10. Work by others includes P. Lacovara, L. Esterowitz, and R. Allen, "Flash-lamp pumped Ti:Al2O3 laser using fluorescent conversion," Opt. Lett. **10**, 273–275 (1985); G. F. Albrecht, J. M. Eggleston, and J. J. Ewing, "Measurements of Ti³⁺:Al2O3 as a lasing material," Opt. Commun. **52**, 401–404 (1985); B. K. Sevast'yanov et al., "Tunable laser based on Al2O3:Ti³⁺ crystal," Sov. Phys. Crystallog. **29**, 566–567 (1984).
2. E. D. Nelson, J. Y. Wong, and A. L. Schawlow, "Far infrared spectra of Al2O3:Cr³⁺ and Al2O3:Ti³⁺," Phys. Rev. **156**, 298–308 (1967).
3. R. R. Joyce and P. L. Richards, "Far infrared spectra of Al2O3 Doped with Ti, V and Cr," Phys. Rev. **179**, 375–380 (1969).
4. R. M. MacFarlane, J. Y. Wong, and M. D. Sturge, "Dynamic Jahn–Teller effect in octahedrally coordinated d^1 impurity systems," Phys. Rev. **166**, 250–258 (1968).
5. D. S. McClure, "Optical spectra of transition-metal ions in corundum," J. Chem. Phys. **36**, 2757–2779 (1962).
6. T. P. Jones, R.L. Coble, and C. J. Mogab, "Defect diffusion in single crystal alumum oxide," J. Am. Ceram. Soc. **52**, 331–334 (1969).
7. G. A. Keig, "Influence of the valence state of added impurity ions on the observed color in doped aluminum oxide single crystals," J. Cryst. Growth **2**, 356–360 (1968).
8. H. K. Eigenmann, Ph.D. dissertation (Swiss Federal Institute of Technology, Zurich, Switzerland, 1970).
9. B. F. Gachter and J. A.Koningstein, "Zero phonon transitions and interacting Jahn–Teller phonon energies from the fluorescence spectrum of α-Al2O3:Ti³⁺," J. Chem. Phys. **60**, 2003–2006 (1974).
10. Similar results have been observed by K. L. Schepler, AFAL, Wright-Patterson Air Force Base, Ohio 45433 (personal communication, 1983).
11. Similar fluorescence lifetime data have been observed by G. Huber, University of Hamburg, Hamburg, Federal Republic of Germany (personal communication, 1984).
12. H. H. Tippins, "Charge-transfer spectra of transition-metal ions in corundum," Phys. Rev. B **1**, 126–135 (1970).
13. G. Nath and G. Walda, "Strong reduction of laser produced damage in sapphire and ruby by doping with TiO2," Z. Naturforsch. **A23**, 624–625 (1968).
14. T. S. Bessonova, M. P. Stanislavskii, and V. Ya. Khaimov-Malkov, "Effect of heat treatment and irradiation on absorption spectra of Ti and Si corundum," Opt. Spectrosc. (USSR) **41**, 87–88 (1976).
15. Electronics Division, Union Carbide, San Diego, Calif.
16. Crystal Systems, Inc., Salem, Mass.
17. P. Lacovara, L. Esterowitz, and M. Kokta, "Growth, spectroscopy and lasing of titanium-doped sapphire," IEEE J. Quantum Electron. **QE-21**, 1614–1618 (1985).
18. C. K. Jorgenson, University of Geneva, Geneva, Switzerland (personal communication, 1985).
19. C. K. Jorgenson, "Comparative ligand field studies IV," Acta Chem. Scand. **11**, 73–85 (1957).
20. P. F. Moulton, "An investigation of the Co:MgF2 laser system," IEEE J. Quantum Electron. **QE-21**, 1582–1595 (1985).
21. D. E. McCumber, "Theory of phonon-terminated optical masers," Phys. Rev. **134**, A299–A306 (1964).
22. D. Curie, *Luminescence in Crystals* (Methuen, London, 1963), p. 69.

Solid-State Laser Materials

Solid-State Laser Materials

P. F. Moulton

P. F. Moulton was born in Springfield, Massachusetts, on May 27, 1946. He received the A.B. degree in physics from Harvard University, Cambridge, Massachusetts, in 1968 and the M.S. and Ph.D. degrees from the Department of Electrical Engineering and Computer Science, Massachusetts Institute of Technology, Cambridge, in 1971 and 1975, respectively. He spent a postdoctorate year in 1975 at MIT Lincoln Laboratory, Lexington, Massachusetts, and became a staff member there in 1976. His work at Lincoln Laboratory included high-resolution infrared spectroscopic measurements of molecules, development of lasers for remote sensing, and research and development of tunable and high-efficiency solid-state lasers. Since 1985 he has been Vice-President and General Manager of the Boston Division of Schwartz Electro-Optics, Concord, Massachusetts, where he is engaged in the research and development of a variety of solid-state laser systems. Dr. Moulton is a senior member of the Institute of Electrical and Electronics Engineers and a member of the Optical Society of America.

Report Documentation Page

1. Report No.	2. Government Accession No.	3. Recipient's Catalog No.
NASA CR-4093		

4. Title and Subtitle		5. Report Date
Titanium-Doped Sapphire Laser Research and Design Study		September 1987
		6. Performing Organization Code

7. Author(s)	8. Performing Organization Report No.
Peter F. Moulton	
	10. Work Unit No.

9. Performing Organization Name and Address	11. Contract or Grant No.
Schwartz Electro-Optics, Inc. Boston Division 45 Winthrop Street Concord, MA 01742	NAS1-17961
	13. Type of Report and Period Covered

12. Sponsoring Agency Name and Address	Contractor Report Final Report
National Aeronautics and Space Administration Langley Research Center Hampton, VA 23665-5225	14. Sponsoring Agency Code

15. Supplementary Notes

Langley Technical Monitor: Arthur L. Newcomb, Jr.

16. Abstract

Three main topics were considered in this study: the fundamental laser parameters of titanium-doped sapphire, characterization of commercially grown material and design of a tunable, narrow-linewidth laser. Fundamental parameters investigated included the gain cross section, upper-state lifetime as a function of temperature and the surface-damage threshold. Commercial material was found to vary widely in the level of absorption of the laser wavelength with the highest absorption in Czochralski-grown crystals. Several Ti:sapphire lasers were constructed, including a multimode laser with greater than 50mJ of output energy and a single-transverse-mode ring laser, whose spectral and temporal characteristics were completely characterized. A design for a narrow-linewidth (single-frequency) Ti:sapphire laser was developed, based on the results of the experimental work. The design involves the use of a single-frequency, quasi-cw master oscillator, employed as an injection source for a pulsed ring laser.

17. Key Words (Suggested by Author(s))	18. Distribution Statement
Ti:sapphire LIDAR Tunable solid state laser	Unclassified—Unlimited Subject Category 36

19. Security Classif. (of this report)	20. Security Classif. (of this page)	21. No. of pages	22. Price
Unclassified	Unclassified	60	A04